

Simultaneous Measurement of Oscillation Parameters in Beam and Atmospheric Neutrino Data from Tokai-to-Kamioka and Super-Kamiokande Experiments

Daniel Robert Clement Barrow

Magdalen College, Oxford University

¹⁰ A Dissertation Submitted to Oxford University

¹¹ for the Degree of Doctor of Philosophy

¹²

13 **Simultaneous Measurement of**

14 **Oscillation Parameters in Beam and**

15 **Atmospheric Neutrino Data from**

16 **Tokai-to-Kamioka and**

17 **Super-Kamiokande Experiments**

18 *Abstract*

19 Lorem ipsum dolor sit amet, consectetur adipiscing elit, sed do eiusmod tempor incididunt ut labore et dolore magna aliqua. Nulla aliquet porttitor lacus luctus accumsan tortor posuere. Pulvinar neque laoreet suspendisse interdum. Sem viverra aliquet eget sit. Nunc sed velit dignissim sodales ut eu sem integer vitae. At erat pellentesque adipiscing commodo elit at imperdiet dui accumsan. Fames ac turpis egestas integer eget aliquet nibh. Scelerisque eu ultrices vitae auctor eu augue. Purus non enim praesent elementum facilisis leo vel. Sollicitudin nibh sit amet commodo. Vitae auctor eu augue ut. Vel quam elementum pulvinar etiam. A condimentum vitae sapien pellentesque habitant morbi tristique senectus. Viverra accumsan in nisl nisi scelerisque eu ultrices. Sed viverra ipsum nunc aliquet bibendum enim. Sit amet purus gravida quis. In vitae turpis massa

³² sed elementum tempus egestas sed sed. Vivamus arcu felis bibendum
³³ ut tristique et egestas. Senectus et netus et malesuada fames ac turpis.
³⁴ Ac auctor augue mauris augue.

35 Declaration

36 This dissertation is the result of my own work, except where ex-
37 plicit reference is made to the work of others, and has not been sub-
38 mitted for another qualification to this or any other university. This
39 dissertation does not exceed the word limit for the respective Degree
40 Committee.

41 Daniel Robert Clement Barrow

42 ©The copyright of this thesis rests with the author and is made available under a Creative
43 Commons Attribution Non-Commercial No Derivatives licence. Researchers are free to copy,
44 distribute or transmit the thesis on the condition that they attribute it, that they do not use
45 it for commercial purposes and that they do not alter, transform or build upon it. For any
46 reuse or redistribution, researchers must make clear to others the licence terms of this work.

47

Acknowledgements

48 at pretium nibh ipsum. Eget nunc scelerisque viverra mauris in aliquam. Arcu vitae
49 elementum curabitur vitae nunc sed velit dignissim. Sed arcu non odio euismod lacinia
50 at quis risus sed. Vitae tempus quam pellentesque nec nam aliquam sem et tortor.
51 Viverra aliquet eget sit amet tellus cras adipiscing. Purus sit amet luctus venenatis
52 lectus magna. In aliquam sem fringilla ut morbi tincidunt augue. Fermentum dui
53 faucibus in ornare. Aliquam malesuada bibendum arcu vitae elementum curabitur
54 vitae nunc sed.

55 Ultricies leo integer malesuada nunc vel risus commodo. Tellus cras adipiscing
56 enim eu turpis egestas pretium. Dictumst quisque sagittis purus sit amet volutpat
57 consequat mauris nunc. Vitae congue mauris rhoncus aenean vel elit scelerisque
58 mauris pellentesque. Vel facilisis volutpat est velit egestas dui id ornare. Suscipit
59 adipiscing bibendum est ultricies. At in tellus integer feugiat scelerisque varius
60 morbi enim. Cras semper auctor neque vitae tempus. Commodo sed egestas egestas
61 fringilla phasellus faucibus. Cras pulvinar mattis nunc sed blandit. Pretium viverra
62 suspendisse potenti nullam ac tortor vitae. Purus sit amet volutpat consequat. Orci
63 sagittis eu volutpat odio facilisis mauris. Sit amet massa vitae tortor condimentum
64 lacinia quis. Commodo sed egestas egestas fringilla phasellus. Sed libero enim sed
65 faucibus turpis. Vitae tempus quam pellentesque nec.

66 Blandit massa enim nec dui. Viverra tellus in hac habitasse platea dictumst vestibulu-
67 lum. Bibendum enim facilisis gravida neque convallis. Sagittis nisl rhoncus mattis
68 rhoncus urna neque. Nisl rhoncus mattis rhoncus urna neque. Ac tortor vitae purus
69 faucibus ornare. Aenean sed adipiscing diam donec adipiscing tristique risus. Sapien
70 nec sagittis aliquam malesuada bibendum. Et leo duis ut diam quam nulla. Tellus
71 rutrum tellus pellentesque eu tincidunt tortor aliquam nulla facilisi. Fermentum leo

⁷² vel orci porta non pulvinar neque. Eget sit amet tellus cras adipiscing enim eu. Sed
⁷³ viverra tellus in hac habitasse platea dictumst vestibulum.

⁷⁴ Sit amet consectetur adipiscing elit. At varius vel pharetra vel turpis nunc eget
⁷⁵ lorem. Elit scelerisque mauris pellentesque pulvinar pellentesque habitant morbi
⁷⁶ tristique senectus. Odio euismod lacinia at quis risus sed vulputate odio. Vitae suscipit
⁷⁷ tellus mauris a diam maecenas sed enim ut. Dignissim convallis aenean et tortor at
⁷⁸ risus viverra. Diam sollicitudin tempor id eu. Erat velit scelerisque in dictum. Blandit
⁷⁹ cursus risus at ultrices. Ac tortor vitae purus faucibus ornare suspendisse sed.

Contents

81	1 Neutrino Oscillation Physics	1
82	1.1 Discovery of Neutrinos	1
83	1.2 Theory of Neutrino Oscillation	3
84	1.2.1 Three Flavour Oscillations	3
85	1.2.2 The MSW Effect	7
86	1.3 Neutrino Oscillation Measurements	9
87	1.3.1 Solar Neutrinos	9
88	1.3.2 Atmospheric Neutrinos	12
89	1.3.3 Accelerator Neutrinos	15
90	1.3.4 Reactor Neutrinos	18
91	2 T2K and SK Experiment Overview	21
92	2.1 The Super-Kamiokande Experiment	21
93	2.1.1 The SK Detector	22
94	2.1.2 Calibration	26
95	2.1.3 Data Acquisition and Triggering	29
96	2.1.4 Cherenkov Radiation	31
97	2.2 The Tokai to Kamioka Experiment	33
98	2.2.1 The Neutrino Beam	35
99	2.2.2 The Near Detector at 280m	38
100	2.2.2.1 Fine Grained Detectors	41
101	2.2.2.2 Time Projection Chambers	42
102	2.2.2.3 π^0 Detector	44
103	2.2.2.4 Electromagnetic Calorimeter	44
104	2.2.2.5 Side Muon Range Detector	46

105	2.2.3 The Interactive Neutrino GRID	46
106	3 Bayesian Statistics and Markov Chain Monte Carlo Techniques	48
107	3.1 Bayesian Statistics	49
108	3.2 Monte Carlo Simulation	50
109	3.2.1 Markov Chain Monte Carlo	52
110	3.2.2 Metropolis-Hastings Algorithm	55
111	3.2.3 MCMC Optimisation	56
112	3.3 Understanding the MCMC Results	60
113	3.3.1 Marginalisation	60
114	3.3.2 Parameter Estimation and Credible Intervals	61
115	3.3.3 Application of Bayes' Theorem	63
116	3.3.4 Comparison of MCMC Output to Expectation	64
117	4 Oscillation Probability Calculation	66
118	4.1 Overview	66
119	4.2 Treatment of Fast Oscillations	72
120	Bibliography	77
121	List of Figures	85
122	List of Tables	90

¹²⁴ **Chapter 1**

¹²⁵ **Neutrino Oscillation Physics**

¹²⁶ When first proposed, neutrinos were expected to be massless fermions that only in-
¹²⁷ teract through weak and gravitational forces. This meant they were very difficult to
¹²⁸ detect as they can pass through significant amounts of matter without interacting. De-
¹²⁹ spite this, experimental neutrino physics has developed with many different detection
¹³⁰ techniques and neutrino sources being used today. In direct tension with the standard
¹³¹ model physics, neutrinos have been determined to oscillate between different lepton
¹³² flavours requiring them to have mass.

¹³³ section 1.1 describes the observation techniques and discovery of neutrinos. The
¹³⁴ theory underpinning neutrino oscillation is described in section 1.2. This section
¹³⁵ includes the approximations which can be made to simplify the understanding of
¹³⁶ neutrino oscillation in a two-flavour approximation as well as how the medium
¹³⁷ in which neutrinos propagate can manipulate the oscillation probability. The past,
¹³⁸ current, and future neutrino experiments are detailed in section 1.3 including the
¹³⁹ reactor, atmospheric, and long-baseline accelerator neutrino sources that have been
¹⁴⁰ used to successfully constrain oscillation parameter determination.

¹⁴¹ **1.1 Discovery of Neutrinos**

¹⁴² At the start of the 20th century, the electrons emitted from the β -decay of the nucleus
¹⁴³ were found to have a continuous energy spectrum [1,2]. This observation seemingly
¹⁴⁴ broke the energy conservation invoked within that period's nuclear models. Postulated

in 1930 by Pauli as the solution to this problem, the neutrino (originally termed “neutron”) was theorized to be an electrically neutral spin-1/2 fermion with a mass of the same order of magnitude as the electron [3]. This neutrino was to be emitted with the electron in β -decay to alleviate the apparent breaking of energy conservation. As a predecessor of the weak interaction model, Fermi’s theory of β -decay developed the understanding by coupling the four constituent particles; electron, proton, neutron, and neutrino, into a consistent model [4].

Whilst Pauli was not convinced of the ability to detect neutrinos. The first observations of the particle were made in the mid-1950s when neutrinos from a reactor were observed via the inverse β -decay (IBD) process, $\bar{\nu}_e + p \rightarrow n + e^+$ [5, 6]. The detector consisted of two parts; a neutrino interaction medium and a liquid scintillator. The interaction medium was built from two water tanks. These were loaded with cadmium chloride to allow increased efficiency of neutron capture. The positron emitted from IBD annihilates, $e^+ + e^- \rightarrow 2\gamma$, generating a prompt signal and the neutron is captured on the cadmium via $n + {}^{108}Cd \rightarrow {}^{109}Cd \rightarrow {}^{109}Cd + \gamma$, producing a delayed signal. The experiment observed an increase in the neutrino event rate when the reactor was operating compared to when it was switched off, in much the same way as modern reactor neutrino experiments operate.

After the discovery of the ν_e , the natural question of how many flavours of neutrino exist was asked. In 1962, a measurement of the ν_μ was conducted at the Brookhaven National Laboratory [7]. A proton beam was directed at a beryllium target, generating a π -dominated beam which then decayed via $\pi^\pm \rightarrow \mu^\pm + (\nu_\mu, \bar{\nu}_\mu)$, and the subsequent interactions of the ν_μ were observed. The final observation to be made was that of the ν_τ from the DONUT experiment [8]. Three neutrinos seem the obvious solution as it mirrors the known number of charged lepton (as they form weak isospin doublets) but there could be evidence of more. Several neutrino experiments have found anomalous

₁₇₁ results [9, 10] which could be attributed to sterile neutrinos however cosmological
₁₇₂ observations indicate the number of neutrino species $N_{eff} = 3.15 \pm 0.23$ [11].

₁₇₃ 1.2 Theory of Neutrino Oscillation

₁₇₄ As direct evidence of beyond Standard Model physics, a neutrino generated with
₁₇₅ lepton flavour α can change into a different lepton flavour β after propagating some
₁₇₆ distance. This phenomenon is called neutrino oscillation and requires that neutrinos
₁₇₇ must have a non-zero mass (as seen in subsection 1.2.1). This is direct evidence
₁₇₈ of beyond standard model physics. This behaviour has been characterised by the
₁₇₉ Pontecorvo-Maki-Nakagawa-Sakata (PMNS) [12–14] mixing matrix which describes
₁₈₀ how the flavour and mass of neutrinos are associated. This is analogous to the Cabibbo-
₁₈₁ Kobayashi-Maskawa (CKM) [15] matrix measured in quark physics.

₁₈₂ 1.2.1 Three Flavour Oscillations

₁₈₃ The PMNS parameterisation defines three flavour eigenstates, ν_e , ν_μ and ν_τ (indexed
₁₈₄ ν_α), which are assigned based upon the weak interaction flavour states and three mass
₁₈₅ eigenstates, ν_1 , ν_2 and ν_3 (indexed ν_i). Each mass eigenstate is the superposition of all
₁₈₆ three flavour states,

$$|\nu_i\rangle = \sum_\alpha U_{\alpha i} |\nu_\alpha\rangle. \quad (1.1)$$

₁₈₇ U is the PMNS matrix which correlates the mass and flavour eigenstates. Neutrinos
₁₈₈ interact with leptons of the same weak flavour eigenstate rather than mass eigenstate.

¹⁸⁹ The propagation of a neutrino flavour eigenstate, in a vacuum, can be re-written as a
¹⁹⁰ plane-wave solution to the time-dependent Schrödinger equation,

$$|\nu_\alpha(t)\rangle = \sum_i U_{\alpha i}^* |\nu_i\rangle e^{-i\phi_i}. \quad (1.2)$$

¹⁹¹ The probability of observing a neutrino of flavour eigenstate β from one which
¹⁹² originated as flavour α can be calculated as,

$$P(\nu_\alpha \rightarrow \nu_\beta) = |\langle \nu_\beta | \nu_\alpha(t) \rangle|^2 = \sum_{i,j} U_{\alpha i}^* U_{\beta i} U_{\alpha j} U_{\beta j}^* e^{-i(\phi_j - \phi_i)} \quad (1.3)$$

¹⁹³ The ϕ_i term can be expressed in terms of the energy, E_i , and magnitude of the
¹⁹⁴ three momenta, p_i , of the neutrino, $\phi_i = E_i t - p_i x$ (t and x being time and position
¹⁹⁵ coordinates). Therefore,

$$\phi_j - \phi_i = E_j t - E_i t - p_j x + p_i x. \quad (1.4)$$

¹⁹⁶ For a relativistic particle, $E_i \gg m_i$,

$$p_i = \sqrt{E_i^2 - m_i^2} \approx E_i - \frac{m_i^2}{2E_i}. \quad (1.5)$$

¹⁹⁷ Making the approximations that neutrinos are relativistic, the mass eigenstates

¹⁹⁸ were created with the same energy and that $x = L$, where L is the distance traveled by

¹⁹⁹ the neutrino, Equation 1.4 then becomes

$$\phi_j - \phi_i = \frac{\Delta m_{ij}^2 L}{2E}, \quad (1.6)$$

²⁰⁰ where $\Delta m_{ij}^2 = m_j^2 - m_i^2$. This, teamed with further use of unitarity relations results

²⁰¹ in Equation 1.3 becoming

$$P(\nu_\alpha \rightarrow \nu_\beta) = \delta_{\alpha\beta} - 4 \sum_{i>j} \Re \left(U_{\alpha i}^* U_{\beta i} U_{\alpha j} U_{\beta j}^* \right) \sin^2 \left(\frac{\Delta m_{ij}^2 L}{4E} \right) + (-) 2 \sum_{i>j} \Im \left(U_{\alpha i}^* U_{\beta i} U_{\alpha j} U_{\beta j}^* \right) \sin \left(\frac{\Delta m_{ij}^2 L}{2E} \right). \quad (1.7)$$

²⁰² Where $\delta_{\alpha\beta}$ is the Kronecker delta function and the negative sign is included for the

²⁰³ oscillation probability of antineutrinos.

²⁰⁴ Typically, the PMNS matrix is parameterised into three mixing angles, a charge

²⁰⁵ parity (CP) violating phase δ_{CP} , and two Majorana phases $\alpha_{1,2}$,

$$U = \underbrace{\begin{pmatrix} 1 & 0 & 0 \\ 0 & c_{23} & s_{23} \\ 0 & -s_{23} & c_{23} \end{pmatrix}}_{\text{Atmospheric, Accelerator}} \underbrace{\begin{pmatrix} c_{13} & 0 & s_{13}e^{-i\delta_{CP}} \\ 0 & 1 & 0 \\ -s_{13}e^{-i\delta_{CP}} & 0 & c_{13} \end{pmatrix}}_{\text{Reactor, Accelerator}} \underbrace{\begin{pmatrix} c_{12} & s_{12} & 0 \\ -s_{12} & c_{12} & 0 \\ 0 & 0 & 1 \end{pmatrix}}_{\text{Reactor, Solar}} \underbrace{\begin{pmatrix} e^{i\alpha_1/2} & 0 & 0 \\ 0 & e^{i\alpha_2/2} & 0 \\ 0 & 0 & 1 \end{pmatrix}}_{\text{Majorana}}. \quad (1.8)$$

206 Where $s_{ij} = \sin(\theta_{ij})$ and $c_{ij} = \cos(\theta_{ij})$. The oscillation parameters are often
 207 grouped; (1, 2) as “solar”, (2, 3) as “atmospheric” and (1, 3) as “reactor”. Many
 208 neutrino experiments aim to measure the PMNS parameters from a wide array of
 209 origins, as is the purpose of this thesis.

210 The Majorana phase, $\alpha_{1,2}$, containing matrix included within Equation 1.8 is only
 211 included for completeness. For an oscillation analysis experiment, any term in this
 212 oscillation probability calculation containing this phase disappears due to taking the
 213 expectation value of the PMNS matrix.

214 A two flavour approximation can be attained when one assumes the third mass
 215 eigenstate is degenerate with another. As discussed in section 1.3, it is found that
 216 $\Delta m_{21}^2 \ll |\Delta m_{31}^2|$. This results in the two flavour approximation being reasonable for
 217 understanding the features of the oscillation. In this two flavour case, the mixing
 218 matrix becomes,

$$U_{2\text{ Flav.}} = \begin{pmatrix} \cos(\theta) & \sin(\theta) \\ -\sin(\theta) & \cos(\theta) \end{pmatrix}. \quad (1.9)$$

219 This culminates in the oscillation probability,

$$\begin{aligned} P(\nu_\alpha \rightarrow \nu_\alpha) &= 1 - \sin^2(2\theta) \sin^2\left(\frac{\Delta m^2 L}{4E}\right), \\ P(\nu_\alpha \rightarrow \nu_\beta) &= \sin^2(2\theta) \sin^2\left(\frac{\Delta m^2 L}{4E}\right). \end{aligned} \quad (1.10)$$

220 For $\alpha \neq \beta$. For a fixed neutrino energy, the oscillation probability is a sinusoidal
 221 function depending upon the distance over which the neutrino propagates. The

222 frequency and amplitude of oscillation are dependent upon the ratio of the $\Delta m^2 / 4E$
223 and $\sin^2 2\theta$, respectively. For more human-readable units, the maximum oscillation
224 probability for a fixed value of θ is given at $L[km] / E[GeV] \sim 1.27 / \Delta m^2$. It is this
225 calculation that determines the best L/E value for a given experiment to be designed
226 around for measurements of a specific value of Δm^2 .

227 1.2.2 The MSW Effect

228 The theory of neutrino oscillation in a vacuum is described in subsection 1.2.1. How-
229 ever, the beam neutrinos and atmospheric neutrinos originating from below the
230 horizon propagate through matter in the Earth. The coherent scattering of neutrinos
231 from a material target modifies the hamiltonian of the system. This results in a change
232 in the oscillation probability. Notably, charged current scattering ($\nu_e + e^- \rightarrow \nu_e + e^-$,
233 propagated by a W boson) only affects electron neutrinos compared to the neutral
234 current scattering ($\nu_l + l^- \rightarrow \nu_l + l^-$, propagated by a Z^0 boson), interacts through
235 all neutrino flavours equally. In the two-flavour limit, the effective mixing parameter
236 becomes

$$\sin^2(2\theta) \rightarrow \sin^2(2\theta_m) = \frac{\sin^2(2\theta)}{(A/\Delta m^2 - \cos(2\theta))^2 + \sin^2(2\theta)}, \quad (1.11)$$

237 where $A = 2\sqrt{2}G_F N_e E$ with N_e is the electron density of the medium and G_F is
238 Fermi's constant. It is clear to see that there exists a value of $A = \Delta m^2 \cos(2\theta)$ for
239 $\Delta m^2 > 0$ which results in a divergent mixing parameter. This resonance is due to
240 the Mikheyev-Smirnov-Wolfenstein (MSW) effect (or more colloquially, the matter
241 resonance) which regenerates the electron neutrino component of the neutrino flux
242 [16–18]. The density at which the resonance occurs is given by

$$N_e = \frac{\Delta m^2 \cos(2\theta)}{2\sqrt{2}G_F E}. \quad (1.12)$$

243 At densities lower than this critical value, the oscillation probability will be much
244 closer to that of vacuum oscillation. The resonance occurring from the MSW effect
245 depends on the sign of Δm^2 . Therefore, any neutrino oscillation experiment which
246 observes neutrinos and antineutrinos which have propagated through matter can have
247 some sensitivity to the ordering of the neutrino mass eigenstates.

248 For an experiment observing atmospheric neutrinos propagating through the Earth,
249 such as the studies presented in this thesis, a model of the Earth's density and layering
250 is required. The model used within this analysis is the Preliminary Reference Earth
251 Model (PREM) [19]. This model provides piecewise cubic polynomials. To follow the
252 methodology set in [20], this analysis simply approximates the model as four layers of
253 constant density with values taken from the PREM model, as described in Table 1.1.
254 As seen in [DB: Link to Oscillation chapter](#), the approximation in this methodology has
255 been removed and the density is instead integrated along the track using the piecewise
256 polynomials.

257 The density measurements provided in the PREM model are provided in terms
258 of mass density, whereas neutrino oscillations are sensitive to the electron number
259 density. This value can be computed as the product of the chemical composition and
260 mass density of each layer.

261 The beam oscillation probability in this thesis uses a baseline of 295km, density
262 2.6g/cm^3 , and chemical composition 0.5.

Layer	Outer Radius [km]	Density [g/cm ³]	Chemical composition (Z/A)
Inner Core	1220	13	0.468 ± 0.029
Outer Core	3480	11.3	0.468 ± 0.029
Lower Mantle	5701	5.0	0.497
Transition Zone	6371	3.3	0.497

Table 1.1: Description of the four layers of the Earth invoked within the PREM model [19].

263 1.3 Neutrino Oscillation Measurements

264 As evidence of beyond standard model physics, the 2015 Nobel Prize in Physics was
 265 awarded to the Super-Kamiokande (SK) [21] and Sudbury Neutrino Observatory
 266 (SNO) [22] collaborations for the first definitive observation of solar and atmospheric
 267 neutrino oscillation [23]. Since then, the field has seen a wide array of oscillation
 268 measurements from a variety of neutrino sources. As seen in subsection 1.2.1, the
 269 neutrino oscillation probability is dependent on the ratio of the propagation baseline, L ,
 270 to the neutrino energy, E . It is this ratio that determines the type of neutrino oscillation
 271 a particular experiment is sensitive to.

272 As illustrated in Figure 1.1, there are many neutrino sources that span a wide
 273 range of energies. The least energetic neutrinos are from diffuse supernovae and
 274 terrestrial neutrinos at $O(1)$ MeV whereas the most energetic neutrinos originate from
 275 atmospheric and galactic neutrinos of $> O(1)$ TeV.

276 1.3.1 Solar Neutrinos

277 Solar neutrinos are emitted from fusion reaction chains at the center of the Sun. The
 278 solar neutrino flux, given as a function of neutrino energy for different fusion and
 279 decay chains is illustrated in Figure 1.2. Whilst proton-proton fusion generates the
 280 largest flux of neutrinos, the neutrinos are of low energy and are difficult to reconstruct

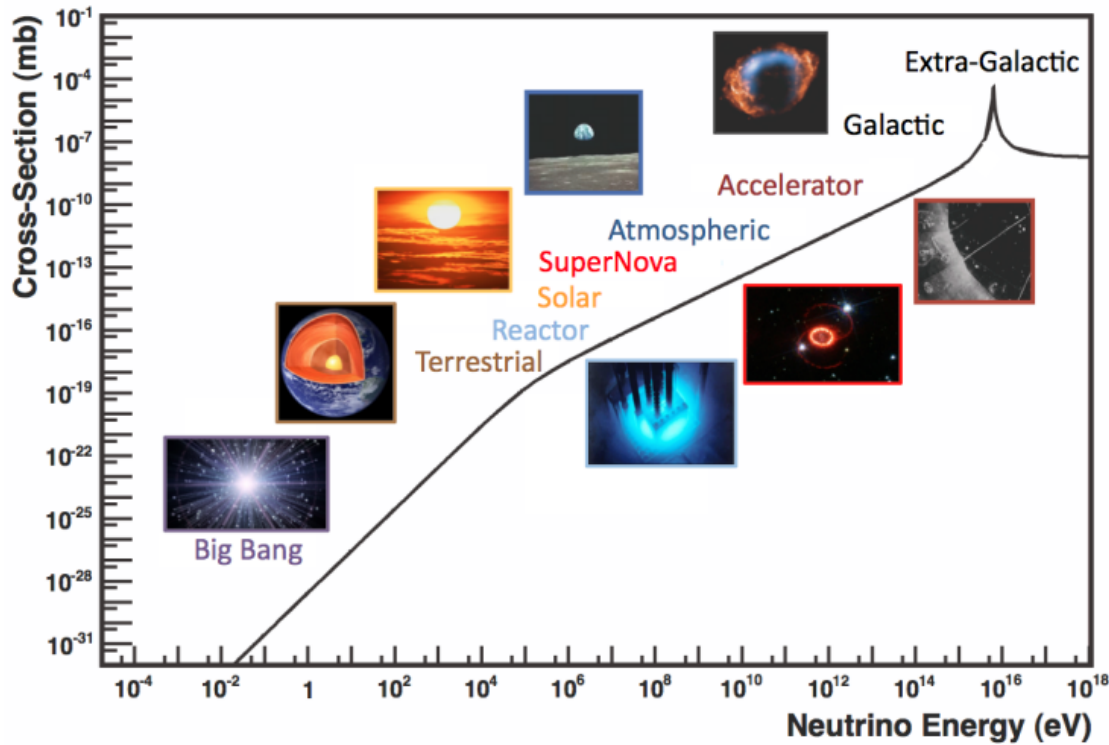


Figure 1.1: The cross-section of neutrinos from various natural and man-made sources as a function of neutrino energy. Taken from [24]

due to the IBD interaction threshold of 1.8MeV. Consequently, most experiments focus on the neutrinos from the decay of 8B (via ${}^8B \rightarrow {}^8Be^* + e^+ + \nu_e$), which are higher energy.

The first measurements of solar neutrinos observed a significant reduction in the event rate compared to predictions from the Standard Solar Model [26, 27]. The proposed solution to this “solar neutrino problem” was $\nu_e \leftrightarrow \nu_\mu$ oscillations in a precursory version of the PMNS model [28]. The Kamiokande [29], Gallex [30] and Sage [31] experiments confirmed the ~ 0.5 factor deficit of solar neutrinos.

The conclusive solution to this problem was determined by the SNO collaboration [32]. Using a deuterium water target to observe 8B neutrinos, the event rate of charged current (CC), neutral current (NC), and elastic scattering (ES) interactions (Given in Equation 1.13) was simultaneously measured. CC events can only occur for electron neutrinos, whereas the other interaction channels are agnostic to neutrino

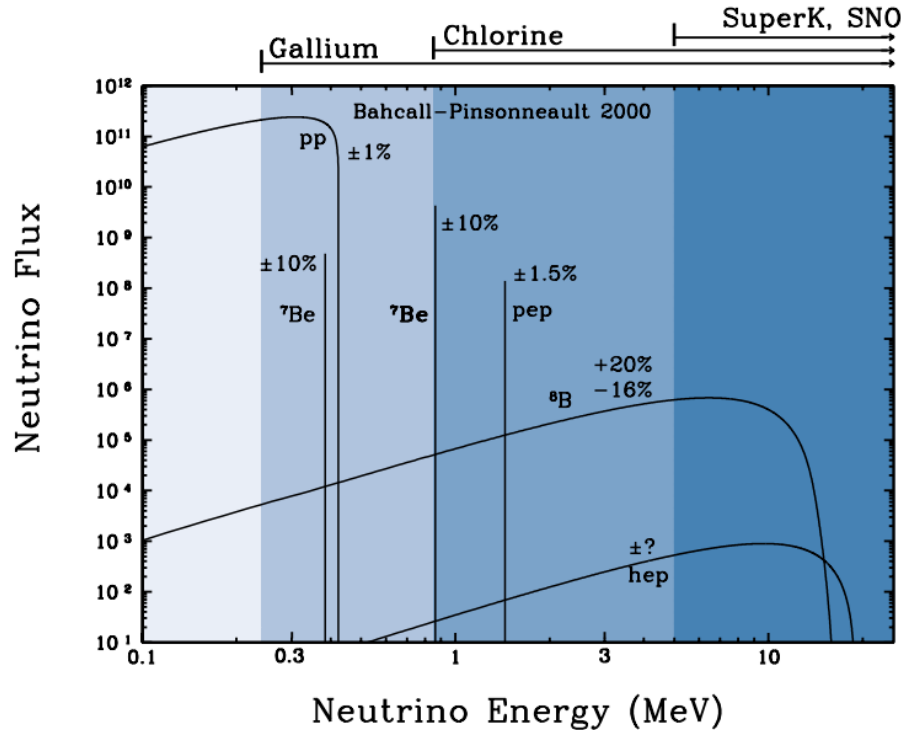


Figure 1.2: The solar neutrino flux as a function of neutrino energy for various fusion reactions and decay chains as predicted by the Standard Solar Model. Taken from [25].

flavour (Although the ES reaction is more sensitive to electron neutrino interactions).
 This meant that there were direct measurements of the ν_e and ν_x neutrino flux. It was concluded that the CC and ES interaction rates were consistent with the deficit previously observed. Most importantly, the NC reaction rate was only consistent with the others under the hypothesis of flavour transformation.

$$\begin{aligned} \nu_e + d &\rightarrow p + p + e^- & (\text{CC}) \\ \nu_x + d &\rightarrow p + n + \nu_x & (\text{NC}) \\ \nu_x + e^- &\rightarrow \nu_x + e^- & (\text{ES}) \end{aligned} \quad (1.13)$$

Many experiments have since measured the neutrino flux of different interaction chains within the sun [33–35]. The most recent measurement was that of CNO neutr-

³⁰¹ nos which were recently observed with 5σ significance by the Borexino collaboration.
³⁰² Future neutrino experiments aim to further these spectroscopic measurements of
³⁰³ different fusion chains within the Sun [36–38]. Solar neutrinos act as an irreducible
³⁰⁴ background for dark matter experiments like DARWIN but oscillation parameter
³⁰⁵ measurements can be made [39].

³⁰⁶ 1.3.2 Atmospheric Neutrinos

³⁰⁷ The interactions of primary cosmic ray protons in Earth's upper atmosphere generate
³⁰⁸ showers of energetic hadrons. These are mostly pions and kaons which when they
³⁰⁹ decay produce a natural source of neutrinos spanning energies of MeV to TeV [40].
³¹⁰ This decay is via

$$\begin{aligned} \pi^\pm &\rightarrow \mu^\pm + (\nu_\mu, \bar{\nu}_\mu) \\ \mu^\pm &\rightarrow e^\pm + (\nu_e, \bar{\nu}_e) + (\nu_\mu, \bar{\nu}_\mu) \end{aligned} \tag{1.14}$$

³¹¹ such that for a single pion decay, three neutrinos are produced. The atmospheric
³¹² neutrino flux energy spectra as predicted by the Bartol [41], Honda [42, 43], and
³¹³ FLUKA [44] models are illustrated in Figure 1.3. The flux distribution peaks at an
³¹⁴ energy of $O(10)\text{GeV}$. The uncertainties associated with these models are dominated
³¹⁵ by the hadronic production of kaon and pions as well as the primary cosmic flux.

³¹⁶ Unlike long-baseline experiments which have a fixed baseline, the distance at-
³¹⁷ mospheric neutrinos propagate is dependent upon the zenith angle at which they
³¹⁸ interact. This is illustrated in Figure 1.4. Neutrinos that are generated directly above
³¹⁹ the detector ($\cos(\theta) = 1.0$) have a baseline equivalent to the height of the atmosphere
³²⁰ whereas neutrinos that interact directly below the detector ($\cos(\theta) = -1.0$) have to

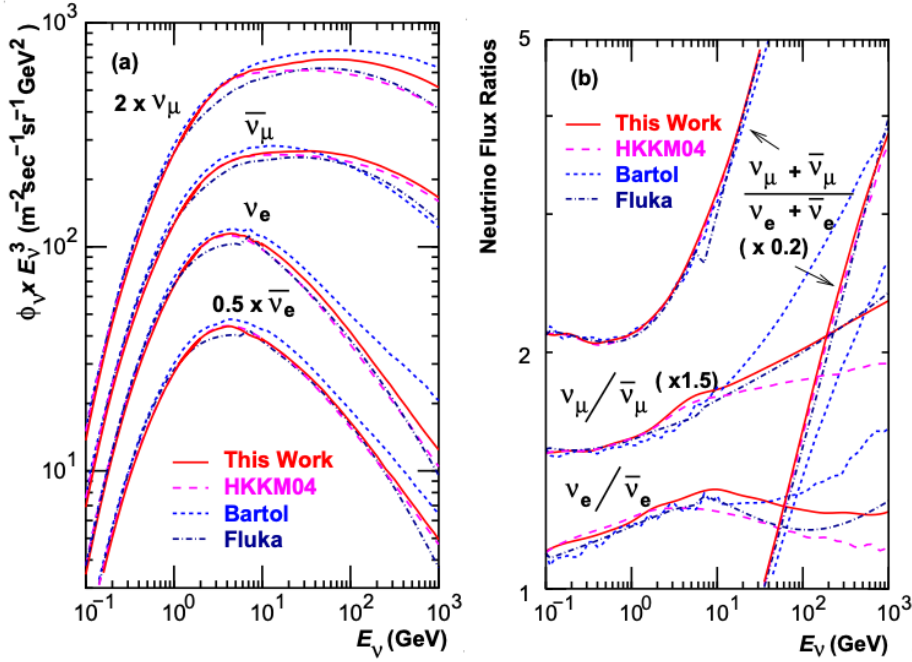


Figure 1.3: Left panel: The atmospheric neutrino flux for different neutrino flavours as a function of neutrino energy as predicted by the 2007 Honda model (“This work”) [42], the 2004 Honda model (“HKKM04”) [43], the Bartol model [41] and the FLUKA model [44]. Right panel: The ratio of the muon to electron neutrino flux as predicted by all the quoted models. Both figures taken from [42].

321 travel a length equal to the diameter of the Earth. This means atmospheric neutrinos
 322 have a baseline that varies from $O(20)\text{km}$ to $O(6 \times 10^3)\text{km}$. Any neutrino generated
 323 at or below the horizon will be subject to matter effects as they propagate through the
 324 Earth.

325 Figure 1.5 highlights the neutrino flux as a function of the zenith angle for different
 326 slices of neutrino energy. For medium to high-energy neutrinos (and to a lesser degree
 327 for low-energy neutrinos), the flux is approximately symmetric around $\cos(\theta) = 0$.
 328 To the accuracy of this approximation, the systematic uncertainties associated with
 329 atmospheric flux for comparing upward-going and down-going neutrino cancels. This
 330 allows the down-going events, which are mostly insensitive to oscillation probabilities,
 331 to act as an unoscillated prediction (similar to a near detector in an accelerator neutrino
 332 experiment).

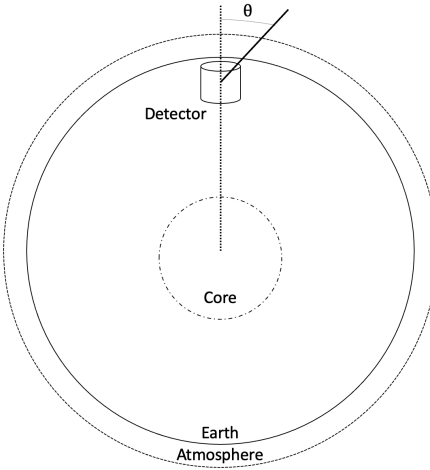


Figure 1.4: A diagram illustrating the definition of zenith angle as used in the Super Kamiokande experiment [45].

³³³ Precursory hints of atmospheric neutrinos were observed in the mid-1960s search-
³³⁴ ing for $\nu_\mu^{(-)} + X \rightarrow X^* + \mu^\pm$ [46]. This was succeeded with the IMB-3 [47] and
³³⁵ Kamiokande [48] experiments which measured the ratio of muon neutrinos com-
³³⁶ pared to electron neutrinos $R(\nu_\mu/\nu_e)$. Both experiments were found to have a con-
³³⁷ sistent deficit of muon neutrinos, with $R(\nu_\mu/\nu_e) = 0.67 \pm 0.17$ and $R(\nu_\mu/\nu_e) =$
³³⁸ $0.60^{+0.07}_{-0.06} \pm 0.05$. Super-Kamiokande (SK) [45] extended this analysis by fitting os-
³³⁹ cillation parameters in $P(\nu_\mu \rightarrow \nu_\tau)$ which found best fit parameters $\sin^2(2\theta) > 0.92$
³⁴⁰ and $1.5 \times 10^{-3} < \Delta m^2 < 3.4 \times 10^{-3} \text{ eV}^2$.

³⁴¹ Since then, atmospheric neutrino experiments have been making precision mea-
³⁴² surements of the $\sin^2(\theta_{23})$ and Δm^2_{32} oscillation parameters. Atmospheric neutrino
³⁴³ oscillation is dominated by $P(\nu_\mu \rightarrow \nu_\tau)$, where SK observed a 4.6σ discovery of ν_τ
³⁴⁴ appearance [49]. Figure 1.6 illustrates the current estimates on the atmospheric mixing
³⁴⁵ parameters from a wide range of atmospheric and accelerator neutrino observatories.

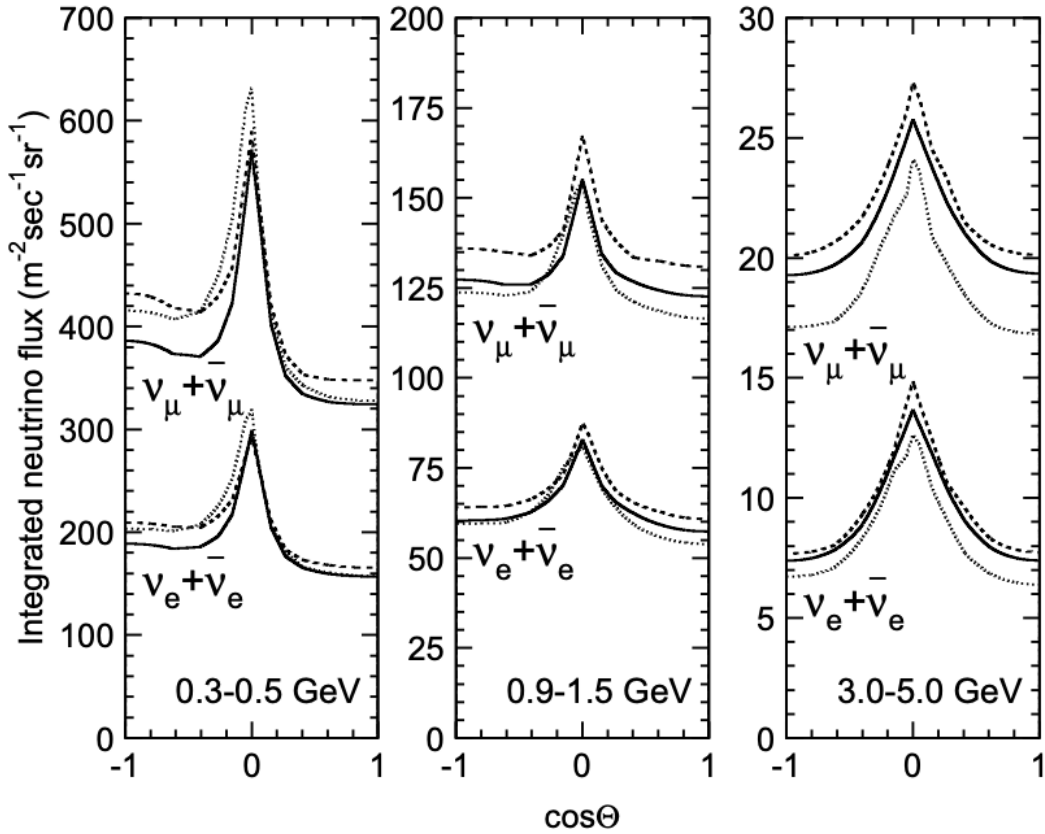


Figure 1.5: Predictions of the summed neutrino and antineutrino flux for electron and muon neutrinos from the Bartol [41], Honda [42] and FLUKA [44] models as a function of zenith angle with respect to the detector. Left panel: $0.3 < E_\nu < 0.5$. Middle panel: $0.9 < E_\nu < 1.5$. Right panel: $3.0 < E_\nu < 5.0$. Figures taken from [45].

346 1.3.3 Accelerator Neutrinos

347 The concept of using a man-made “neutrino beam” was first realised in 1962 [56].
 348 Since then, many experiments have followed which all use the same fundamental
 349 concepts. Typically, a proton beam is aimed at a target producing charged mesons that
 350 decay to neutrinos. The mesons can be sign-selected by the use of magnetic focusing
 351 horns to generate a neutrino or antineutrino beam. Pions are the primary meson that
 352 decay and depending on the orientation of the magnetic field, a muon (anti-)neutrino
 353 beam is generated via $\pi^+ \rightarrow \mu^+ + \nu_\mu$ or $\pi^- \rightarrow \mu^- + \bar{\nu}_\mu$. The decay of muons and
 354 kaons does result in an irreducible intrinsic electron neutrino background. In T2K,

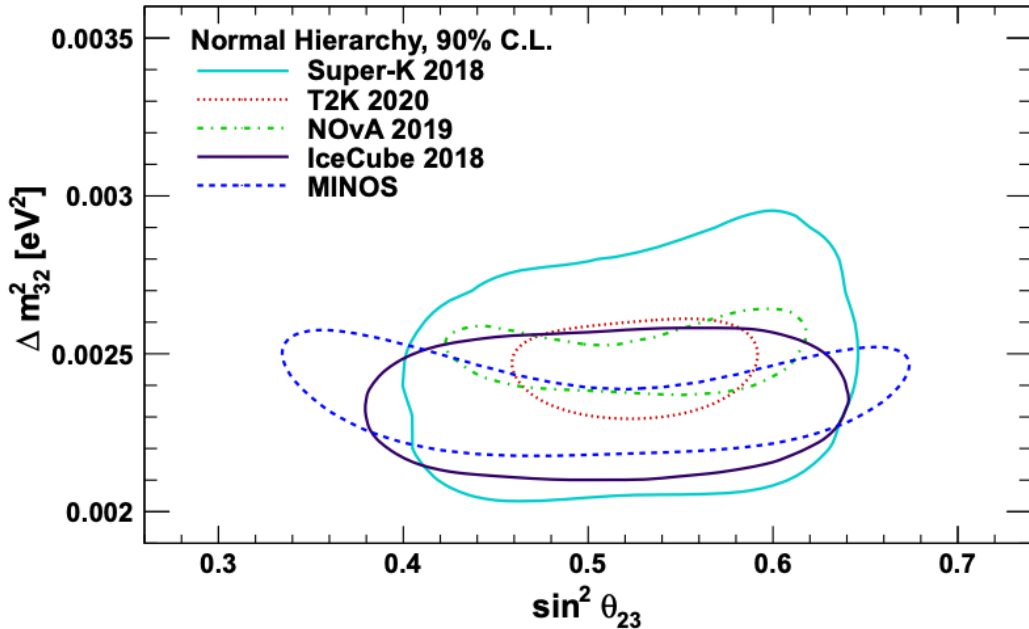


Figure 1.6: Constraints on the atmospheric oscillation parameters, $\sin^2(\theta_{23})$ and Δm_{32}^2 , from atmospheric and long baseline experiments: SK [50], T2K [51], NO ν A [52], IceCube [53] and MINOS [54]. Figure taken from [55].

355 this background contamination is $O(< 1\%)$ [57]. There is also an approximately $\sim 5\%$
 356 “wrong-sign” neutrino background of $\bar{\nu}_\mu$ generated via the same decays.

357 The energy of each neutrino in the beam is dependent on the energy of the initial
 358 proton beam. Therefore, tuning the proton energy allows the neutrino energy to be set
 359 to a value that maximises the disappearance oscillation probability in the L/E term in
 360 Equation 1.10. This means that accelerator experiments are typically more sensitive
 361 to the mixing parameters as compared to a natural neutrino source. However, the
 362 disadvantage compared to atmospheric neutrino experiments is that the baseline has
 363 to be shorter due to the lower flux. Consequently, there is typically less sensitivity to
 364 matter effects and the ordering of the neutrino mass eigenstates.

365 A neutrino experiment measures

$$R(\vec{x}) = \Phi(E_\nu) \times \sigma(E_\nu) \times \epsilon(\vec{x}) \times P(\nu_\alpha \rightarrow \nu_\beta), \quad (1.15)$$

where $R(\vec{x})$ is the event rate of neutrinos at position \vec{x} , $\Phi(E_\nu)$ is the flux of neutrinos with energy E_ν , $\sigma(E_\nu)$ is the cross-section of the neutrino interaction and $\epsilon(\vec{x})$ is the efficiency of the detector. In order to leverage the most out of an accelerator neutrino experiment, the flux and cross-section systematics need to be constrained. This is typically done via the use of a “near detector”, situated at a baseline of $O(1)$ km. This detector observes the unoscillated neutrino flux and constrains the parameters used within the flux and cross-section model.

The first accelerator experiments to precisely measure oscillation parameters were MINOS [58] and K2K [59]. These experiments confirmed the $\nu_\mu \rightarrow \nu_\mu$ oscillations seen in atmospheric neutrino experiments by finding consistent mixing parameter values for $\sin^2(\theta_{23})$ and Δm_{23}^2 . The current generation of accelerator neutrino experiments, T2K and NOvAextended this field by observing $\bar{\nu}_\mu \rightarrow \bar{\nu}_e$ and lead the sensitivity to atmospheric mixing parameters as seen in Figure 1.6 [60]. The two experiments differ in their peak neutrino energy, baseline, and detection technique. The NOvAexperiment is situated at a baseline of 810km from the NuMI beamline which delivers 2GeV neutrinos. The T2K neutrino beam is peaked around 0.6GeV and propagates 295km. The NOvAexperiment also uses functionally identical detectors (near and far) which allow the approximate cancellation of detector systematics whereas T2K uses a plastic scintillator technique at the near detector and a water Cherenkov far detector. The future generation experiments DUNE [61] and Hyper-Kamiokande [62] will succeed these experiments as the high-precision era of neutrino oscillation parameter measurements develops.

³⁸⁸ Several anomalous results have been observed in the LSND [9] and MiniBooNE [10]
³⁸⁹ detectors which were designed with purposefully short baselines. Parts of the neu-
³⁹⁰ trino community attributed these results to oscillations induced by a fourth “sterile”
³⁹¹ neutrino [63] but several searches in other experiments, MicroBooNE [64] and KAR-
³⁹² MEN [65], found no hints of additional neutrino species. The solution to the anomalous
³⁹³ results are still being determined.

³⁹⁴ 1.3.4 Reactor Neutrinos

³⁹⁵ As illustrated in the first discovery of neutrinos (section 1.1), nuclear reactors are a very
³⁹⁶ useful man-made source of electron antineutrinos. For reactors that use low-enriched
³⁹⁷ uranium ^{235}U as fuel, the antineutrino flux is dominated by the β -decay fission of ^{235}U ,
³⁹⁸ ^{238}U , ^{239}Pu and ^{241}Pu [66] as illustrated in Figure 1.7.

³⁹⁹ Due to their low energy, reactor electron antineutrinos predominantly interact
⁴⁰⁰ via the inverse β -decay (IBD) interaction. The typical signature contains two signals
⁴⁰¹ delayed by $O(200)\mu\text{s}$; firstly the prompt photons from positron annihilation, and
⁴⁰² secondly the photons emitted ($E_{tot}^\gamma = 2.2\text{MeV}$) from de-excitation after neutron capture
⁴⁰³ on hydrogen. Searching for both signals improves the detector’s ability to distinguish
⁴⁰⁴ between background and signal events [68]. Recently, SK included gadolinium dopants
⁴⁰⁵ into the ultra-pure water to increase the energy released from the photon cascade to
⁴⁰⁶ $\sim 8\text{MeV}$ and reduce the time of the delayed signal to $\sim 28\mu\text{s}$.

⁴⁰⁷ There are many short baseline experiments ($L \sim O(1)\text{km}$) that have measured the
⁴⁰⁸ $\sin^2(\theta_{13})$ and Δm_{23}^2 oscillation parameters. Daya Bay [69], RENO [70] and Double
⁴⁰⁹ Chooz [71] have all provided precise measurements, with the first discovery of a
⁴¹⁰ non-zero θ_{13} made by Daya Bay and RENO (and complimented by T2K [71]). The
⁴¹¹ constraints on $\sin^2(\theta_{13})$ by the reactor experiments lead the field and are often used as

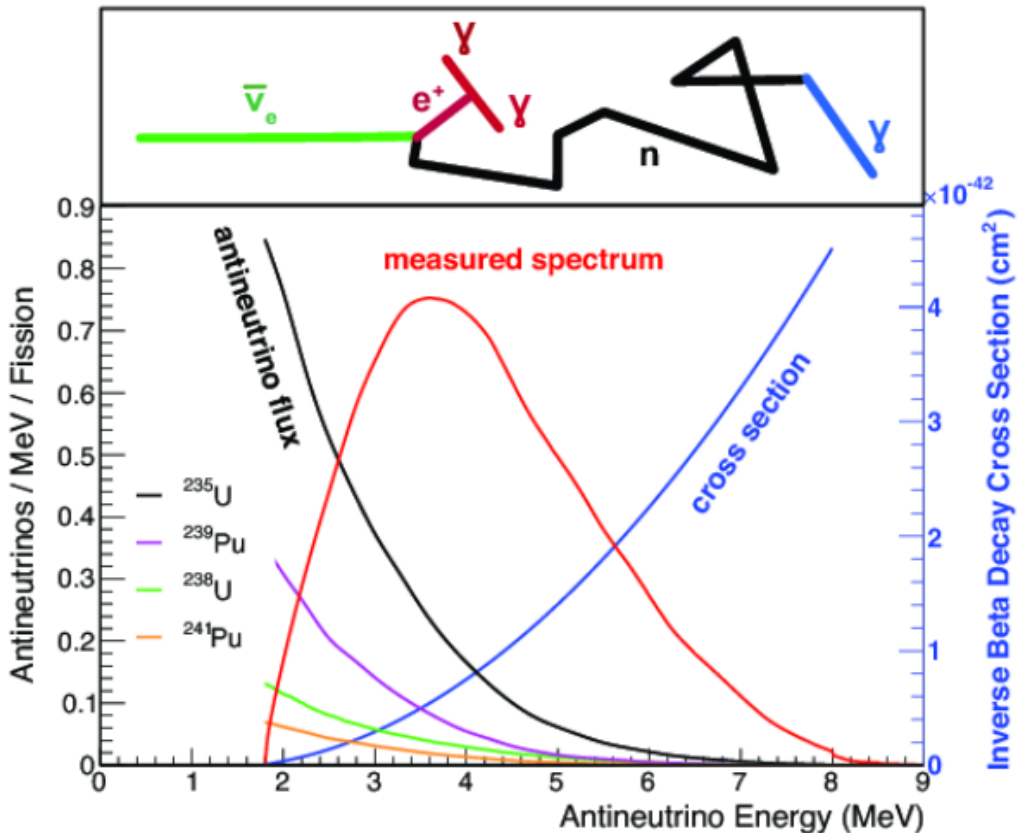


Figure 1.7: Reactor electron antineutrino fluxes for ^{235}U (Black), ^{238}U (Green), ^{239}Pu (Purple), and ^{241}Pu (Orange) isotopes. The inverse β -decay cross-section (Blue) and corresponding measurable neutrino spectrum (Red) are also given. Top panel: Schematic of Inverse β -decay interaction including the eventual capture of the emitted neutron. This capture emits a γ -ray which provides a second signal of the event. Taken from [67].

412 external inputs to accelerator neutrino experiments to improve their sensitivity to δ_{CP}
 413 and mass hierarchy determination. JUNO-TAO [72], a small collaboration within the
 414 larger JUNO experiment, is a next-generation reactor experiment that aims to precisely
 415 measure the isotopic antineutrino yields from the different fission chains. Alongside
 416 this, it aims to explain the ‘5MeV excess’ [73–75] by conducting a search for sterile
 417 neutrinos with a mass scale of around 1eV.

418 Kamlan [76] is the only experiment to have observed reactor neutrinos using a
 419 long baseline (flux weighted averaged baseline of $L \sim 180\text{km}$) which allows it to have
 420 sensitivity to Δm_{12}^2 . Combined with the SK solar neutrino experiment, the combined

- ⁴²¹ analysis puts the most stringent constraint on Δm_{12}^2 [77] which is used as a prior
⁴²² uncertainty within accelerator neutrino experiments.

⁴²³ **Chapter 2**

⁴²⁴ **T2K and SK Experiment Overview**

⁴²⁵ As the successor of the Kamiokande experiment, the Super-Kamiokande (SK) collabora-
⁴²⁶ ration has been leading atmospheric neutrino oscillation analyses for over two decades.
⁴²⁷ The detector has provided some of the strongest constraints on proton decay limits
⁴²⁸ and as well as the first precise measurements of the Δm_{23}^2 and $\sin^2(\theta_{23})$ neutrino
⁴²⁹ oscillation parameters. Despite this, the ability of the detector to low-energy neutrino
⁴³⁰ events has been significantly improved with the recent gadolinium doping of the
⁴³¹ ultra-pure water target. section 2.1 describes the history, detection technique, and
⁴³² operation of the SK detector.

⁴³³ The Tokai-to-Kamioka (T2K) experiment was one of the first long-baseline ex-
⁴³⁴ periments to use both neutrino and antineutrino beams to precisely measure the
⁴³⁵ charge parity violation within the neutrino sector. With the SK detector observing
⁴³⁶ the oscillated neutrino flux, the T2K experiment observed the first hints of a non-zero
⁴³⁷ $\sin^2(\theta_{13})$ measurement and continues to lead the field with the constraints it pro-
⁴³⁸ vides on $\sin^2(\theta_{13})$, $\sin^2(\theta_{23})$, Δm_{23}^2 and δ_{CP} . section 2.2 documents the techniques
⁴³⁹ which T2K uses in generating its neutrino beam as well as the ‘near-detector’ used to
⁴⁴⁰ constrain the flux and cross-section parameters invoked within the systematic models.

⁴⁴¹ **2.1 The Super-Kamiokande Experiment**

⁴⁴² The SK experiment began taking data in 1996 [78] and has had many modifications
⁴⁴³ throughout its lifespan. There have been seven defined periods of data taking as

noted in Table 2.1. Data taking began in SK-I which ran for five years. Between the SK-I and SK-II periods, a significant proportion of the PMTs were damaged during maintenance. Those that survived were equally distributed throughout the detector in the SK-II era, which resulted in a reduced photo-coverage. From SK-III onwards, repairs to the detector meant the full suite of PMTs was operational. Before the start of SK-IV, the data acquisition and electronic systems were upgraded. Between SK-IV and SK-V, a significant effort was placed into tank open maintenance and repair/replacement of defective PMTs, a task for which the author of this thesis was required. Consequently, the detector conditions were significantly different between the two operational periods. SK-VI saw the start of the 0.01% gadolinium doped water. SK-VII, which started during the writing of this thesis, has increased the gadolinium concentration to 0.03% for continued operation. [DB: Link to Linyan's talk from Nu2022.](#)

Period	Start Date	End Date	Live-time (days)
I	April 1996	July 2001	1489.19
II	October 2002	October 2005	798.59
III	July 2006	September 2008	518.08
IV	September 2008	May 2018	3244.4
V	January 2019	July 2020	461.02
VI	July 2020	May 2022	583.3
VII	May 2022	Ongoing	N/A

Table 2.1: The various SK periods and respective live-time. The SK-VI live-time is calculated until 1st April 2022. SK-VII started during the writing of this thesis.

2.1.1 The SK Detector

The basic structure of the Super-Kamiokande (SK) detector is a cylindrical tank with a diameter 39.3m and height 41.1m filled with ultrapure water [79]. A diagram of the significant components of the SK detector is illustrated in Figure 2.1. The SK detector

is situated in the Kamioka mine in Gifu, Japan. The mine is underground with roughly 1km rock overburden (2.7km water equivalent overburden) [80]. At this depth, the rate of cosmic ray muons is significantly decreased to a value of $\sim 2\text{Hz}$. The top of the tank is covered with stainless steel which is designed as a working platform for maintenance, calibration, and location for high voltage and data acquisition electronics.

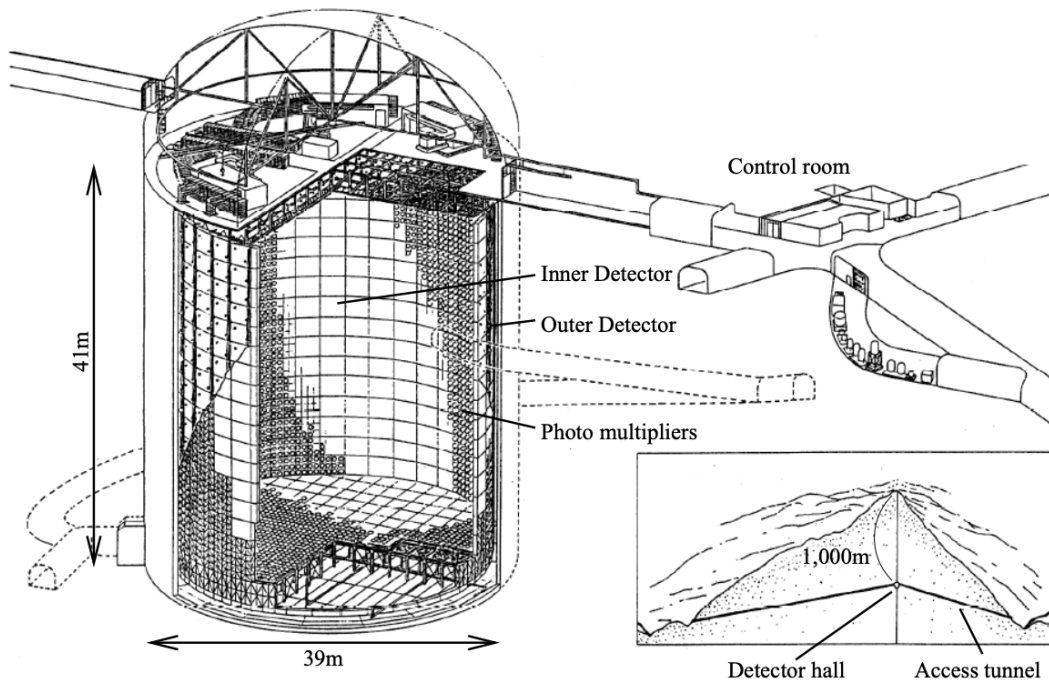


Figure 2.1: A schematic diagram of the Super-Kamiokande Detector. Taken from [81].

A smaller cylindrical structure (36.2m diameter, 33.8m height) is situated inside the tank, with an approximate 2m gap between this structure and the outer tank wall. The purpose of this structure is to support the photomultiplier tubes (PMTs). The volume inside and outside the support structure is referred to as the inner detector (ID) and outer detector (OD), respectively. In the SK-IV era, the ID and OD are instrumented by 11,129 50cm and 1,885 20cm PMTs respectively [79]. The ID contains a 32kton mass of water. Many analyses performed at SK use a “fiducial volume” defined by the volume of water inside the ID excluding some distance to the ID wall. This reduces the volume of the detector which is sensitive to neutrino events but reduces radioactive

⁴⁷⁵ backgrounds and allows for better reconstruction performance. The nominal fiducial
⁴⁷⁶ volume is defined as the area contained inside 2m from the ID wall for a total of
⁴⁷⁷ 22.5kton water [82].

⁴⁷⁸ The two regions of the detector (ID and OD) are optically separated with opaque
⁴⁷⁹ black plastic. The purpose of this is to determine whether a track entered or exited
⁴⁸⁰ the ID. This allows cosmic ray muons and partially contained events to be tagged and
⁴⁸¹ separated from neutrino events entirely contained within the ID. This black plastic is
⁴⁸² also used to cover the area between the ID PMTs to reduce photon reflection from the
⁴⁸³ ID walls. Opposite to this, the OD is lined with a reflective material to allow photons to
⁴⁸⁴ reflect around inside the OD until collected by one of the PMTs. Furthermore, each OD
⁴⁸⁵ PMT is backed with $50 \times 50\text{cm}$ plates of wavelength shifting acrylic which increases
⁴⁸⁶ the efficiency of light collection [80].

⁴⁸⁷ In the SK-IV data-taking period, the photocathode coverage of the detector, or the
⁴⁸⁸ fraction of the ID wall instrumented with PMTs, is $\sim 40\%$ [80]. The PMTs have a
⁴⁸⁹ quantum efficiency (the ratio of detected electrons to incident photons) of $\sim 21\%$ for
⁴⁹⁰ photons with wavelengths of $360\text{nm} < \lambda < 390\text{nm}$. The proportion of photoelectrons
⁴⁹¹ that produce a signal in the dynode of a PMT, termed the collection efficiency, is
⁴⁹² $> 70\%$ [80]. The PMTs used within SK are most sensitive to photons with wavelength
⁴⁹³ $300\text{nm} \leq \lambda \leq 600\text{nm}$ [80]. One disadvantage of using PMTs as the detection media
⁴⁹⁴ is that the Earth's geomagnetic field can modify its response. Therefore, a set of
⁴⁹⁵ compensation coils is built around the inner surface of the detector to mitigate this
⁴⁹⁶ effect [83].

⁴⁹⁷ As mentioned, the SK detector is filled with ultrapure water, which in a perfect
⁴⁹⁸ world would contain no impurities. However, bacteria and organic compounds can
⁴⁹⁹ significantly degrade the water quality. This decreases the attenuation length which
⁵⁰⁰ reduces the total number of photons that hit a PMT. To combat this, a sophisticated

501 water treatment system has been developed [80,84]. UV lights, mechanical filters, and
502 membrane degasifiers are used to reduce the bacteria, suspended particulates, and
503 radioactive materials from the water. The flow of water within the tank is also critical
504 as it can remove stagnant bacterial growth or build-up of dust on the surfaces within
505 the tank. Gravity drifts impurities in the water towards the bottom of the tank which,
506 if left uncontrolled, can create asymmetric water conditions between the top and
507 bottom of the tank. Typically, the water entering the tank is cooled below the ambient
508 temperature of the tank to control convection and inhibit bacteria growth. Furthermore,
509 the dark noise hits within PMTs is sensitive to the PMT temperature [85] so controlling
510 the temperature gradients within the tank is beneficial for stable measurements.

511 SK-VI is the first phase of the SK experiment to use gadolinium dopants within
512 the ultrapure water [DB: Link to Linyan's talk at Nu2022](#). As such, the SK water
513 system had to be replaced to avoid removing the gadolinium concentrate from the
514 ultrapure water [86]. For an inverse β -decay (IBD) interaction in a water target, the
515 emitted neutron is thermally captured on hydrogen. This process releases 2.2MeV γ
516 rays which are difficult to detect due to Compton scattered electrons from a γ ray of
517 this energy is very close to the Cherenkov threshold, limiting the number of photons
518 produced. Thermal capture of neutrons on gadolinium generates γ rays with higher
519 energy meaning they are more easily detected. SK-VI has 0.01% Gd loading (0.02%
520 gadolinium sulphate by mass) which causes \approx 50% of neutrons emitted by IBD to
521 be captured on gadolinium [87,88]. Whilst predominantly useful for low energy
522 analyses, Gd loading allows better $\nu/\bar{\nu}$ separation for atmospheric neutrino event
523 selections [89]. Efforts are currently in place to increase the gadolinium concentrate to
524 0.03% for \approx 75% neutron capture efficiency on gadolinium [DB: Link to Mark's talk at](#)
525 [Nu2022](#). The final stage of loading targets 0.1% concentrate.

526 2.1.2 Calibration

527 The calibration of the SK detector is documented in [79] and summarised below. The
528 analysis presented within this thesis is dependent upon ‘high energy events’ (Charged
529 particles with $O(> 100)\text{MeV}$ momenta). These are events that are expected to generate
530 a larger number of photons such that each PMT will be hit with multiple photons.
531 The reconstruction of these events depends upon the charge deposited within each
532 PMT and the timing response of each individual PMT. Therefore, the most relevant
533 calibration techniques to this thesis are outlined.

534 Before installation, 420 PMTs were calibrated to have identical charge responses
535 and then distributed throughout the tank in a cross-shape pattern (As illustrated by
536 Figure 2.2). These are used as a standardised measure for the rest of the PMTs installed
537 at similar geometric positions within SK to be calibrated against. To perform this
538 calibration, a xenon lamp is located at the center of the SK tank which flashes uniform
539 light at 1Hz. This allows for geometrical effects, water quality variation, and timing
540 effects to be measured in-situ throughout normal data-taking periods.

541 When specifically performing calibration of the detector (in out-of-data taking
542 mode), the water in the tank was circulated to avoid top/bottom asymmetric water
543 quality. Any non-uniformity within the tank significantly affects the PMT hit proba-
544 bility through scattering or absorption. This becomes a dominant effect for the very
545 low-intensity light sources discussed later which are designed such that only one
546 photon is incident upon a given PMT.

547 The “gain” of a PMT is defined as the ratio of the total charge of the signal produced
548 compared to the charge of photoelectrons emitted by the photocathodes within the
549 PMT. To calibrate the signal of each PMT, the “relative” and “absolute” gain values are

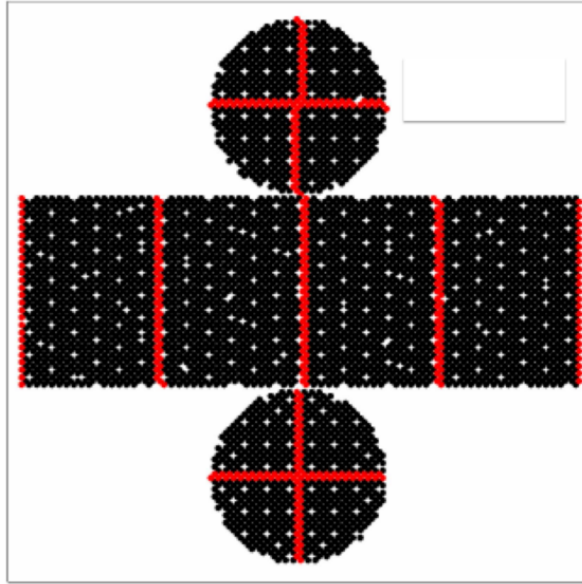


Figure 2.2: The location of “standard PMTs” (red) inside the SK detector. Taken from [79].

measured. The relative gain is the variation of gain among each of the PMTs whereas the absolute gain is the average gain of all PMTs.

The relative gain is calibrated as follows. A laser is used to generate two measurements; a high-intensity flash that illuminates every PMT with a sufficient number of photons, and a low-intensity flash in which only a small number of PMTs collect light. The first measurement creates an average charge, $Q_{obs}(i)$ on PMT i , whereas the second measurement ensures that each hit PMT only generates a single photoelectron. For the low-intensity measurement, the number of times each PMT records a charge larger than $1/4$ photoelectrons, $N_{obs}(i)$, is counted. The values measured can be expressed as

$$\begin{aligned} Q_{obs}(i) &\propto I_H \times f(i) \times \epsilon(i) \times G(i), \\ N_{obs}(i) &\propto I_L \times f(i) \times \epsilon(i), \end{aligned} \tag{2.1}$$

Where I_H and I_L is the intensity of the high and low flashes, $f(i)$ is the acceptance efficiency of the i^{th} PMT, $\epsilon(i)$ is the product of the quantum and collection efficiency

561 of the i^{th} PMT and $G(i)$ is the gain of the i^{th} PMT. The relative gain for each PMT can
 562 determined by taking the ratio of these quantities.

563 The absolute gain calibration is performed by observing fixed energy γ -rays of
 564 $E_{\gamma} \sim 9\text{MeV}$ emitted isotropically from neutron capture on a NiCf source situated at
 565 the center of the detector. This generates a photon yield of about 0.004 photoelec-
 566 trons/PMT/event, meaning that $> 99\%$ of PMT signals are generated from single
 567 photoelectrons. A charge distribution is generated by performing this calibration over
 568 all PMTs, and the average value of this distribution is taken to be the absolute gain
 569 value.

570 As mentioned in subsection 2.1.1, the average quantum and collection efficiency
 571 for the SK detector is $\sim 21\%$ and $> 70\%$ respectively. However, these values do differ
 572 between each PMT and need to be calibrated accordingly. Consequently, the NiCf
 573 source is also used to calibrate the “quantum \times collection” efficiency (denoted “QE”)
 574 value of each PMT. The NiCf low-intensity source is used as the PMT hit probability
 575 is proportional to the QE ($N_{\text{obs}}(i) \propto \epsilon(i)$ in Equation 2.1). A Monte Carlo prediction
 576 which includes photon absorption, scattering, and reflection is made to estimate the
 577 number of photons incident on each PMT and the ratio of the number of predicted
 578 to observed hits is calculated. The difference is attributed to the QE efficiency of that
 579 PMT. This technique is extended to calculate the relative QE efficiency by normalizing
 580 the average of all PMTs which removes the dependence on the light intensity.

581 Due to differing cable lengths and readout electronics, the timing response between
 582 a photon hitting the PMT and the signal being captured by the data acquisition can be
 583 different between each PMT. Due to threshold triggers (Described in subsection 2.1.3),
 584 the time at which a pulse reaches a threshold is dependent upon the size of the pulse.
 585 This is known as the ‘time-walk’ effect and also needs to be accounted for in each PMT.
 586 To calibrate the timing response, a pulse of light with width 0.2ns is emitted into the

587 detector through a diffuser Two-dimensional distributions of time and pulse height
588 (or charge) are made for each PMT and are used to calibrate the timing response. This
589 is performed in-situ whilst data taking with the light source pulsing at 0.03Hz.

590 The top/bottom water quality asymmetry is measured using the NiCf calibration
591 data and cross-referencing these results to the “standard PMTs”. The water attenuation
592 length is continuously measured by the rate of vertically-downgoing cosmic-ray
593 muons which enter via the top of the tank.

594 2.1.3 Data Acquisition and Triggering

595 Dark noise is the phenomenon where a PMT registers a pulse that is consistent with a
596 single photoelectron emitted from photon detection despite the PMT being in complete
597 darkness. This is predominately caused by two processes. Firstly there is intrinsic
598 dark noise which is where photoelectrons gain enough thermal energy to be emitted
599 from the photocathode, and secondly, the radioactive decay of contaminants inside the
600 structure of the PMT. Typical dark noise rate for PMTs used within SK are $O(3)$ kHz [80]
601 which equates to about 12 dark noise hits per 220ns [90]. This is lower than the
602 expected number of photons generated for a ‘high energy event’ (As described in
603 subsection 2.1.4) but instability in this value can cause biases in reconstruction.

604 The analysis presented in this thesis only uses the SK-IV period of the SK exper-
605 iment so this subsection focuses on the relevant points of the data acquisition and
606 triggering systems to that SK period. The earlier data acquisition and triggering
607 systems are documented in [91, 92].

608 Before the SK-IV period started, the existing front-end electronics were replaced
609 with “QTC-Based Electrons with Ethernet, QBEE” systems [93]. When the QBEE
610 observes a signal above a 1/4 photoelectron threshold, the charge-to-time (QTC)

converter generates a rectangular pulse. The start of the rectangular pulse indicates the time at which the analog photoelectron signal was received and the width of the pulse indicates the total charge integrated throughout the signal. This is then digitized by time-to-digital converters and sent to the “front-end” PCs. The digitized signal from every QBEE is then chronologically ordered and sent to the “merger” PCs. It is the merger PCs that apply the software trigger. Any triggered events are passed to the “organizer” PC. This sorts the data stream of multiple merger PCs into chronologically ordered events which are then saved to disk. The schematic of data flow from PMTs to disk is illustrated in Figure 2.3.

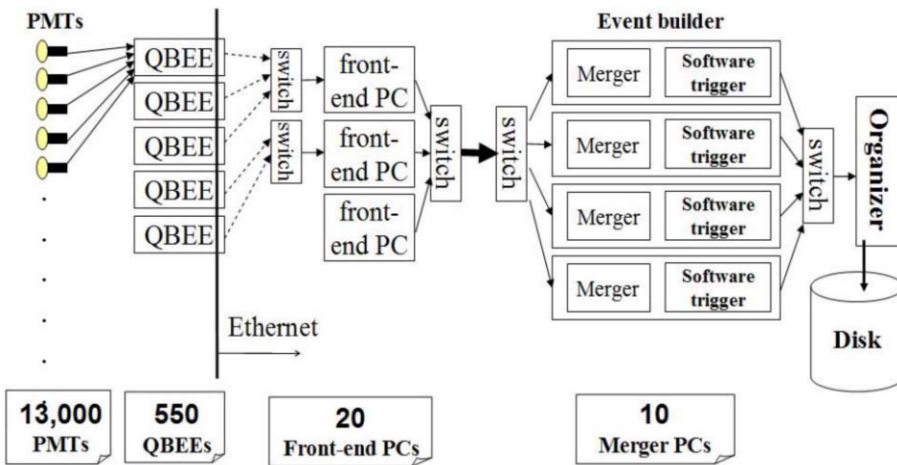


Figure 2.3: Schematic view of the data flow through the data acquisition and online system. Taken from [94].

The software trigger (described in [95]) operates by determining the number of PMT hits within a 200ns sliding window, N_{200} , coincides with the maximum time that a Cherenkov photon would take to traverse the length of the SK tank [92]. For lower energy events that generate fewer photons, this technique is useful for eliminating background processes like dark noise and radioactive decay which would be expected to separate in time. When the value of N_{200} exceeds some threshold, a software trigger is issued. There are several trigger thresholds used within the SK-IV period which are detailed in Table 2.2. If one of these thresholds is met, the PMT hits within an extended

time window are also read out and saved to disk. In the special case of an event that exceeds the SHE trigger but does not exceed the OD trigger, the AFT trigger looks for delayed coincidences of 2.2MeV gamma rays emitted from neutron capture in a $535\mu\text{s}$ window after the SHE trigger. A similar but more complex “Wideband Intelligent Trigger (WIT)” has been deployed and is described in [90].

Trigger	Acronym	Condition	Extended time window (μs)
Super Low Energy	SLE	>34/31 hits	1.3
Low Energy	LE	>47 hits	40
High Energy	HE	>50 hits	40
Super High Energy	SHE	>70/58 hits	40
Outer Detector	OD	>22 hits in OD	N/A

Table 2.2: The trigger thresholds and extended time windows saved around an event which were utilised throughout the SK-IV period. The exact thresholds can change and the values listed here represent the thresholds at the start and end of the SK-IV period.

2.1.4 Cherenkov Radiation

Cherenkov light is emitted from any highly energetic charged particle traveling with relativistic velocity, β , greater than the local speed of light in a medium [96]. Cherenkov light is formed at the surface of a cone with characteristic pitch angle,

$$\cos(\theta) = \frac{1}{\beta n}. \quad (2.2)$$

where n is the refractive index of the medium. Consequently, the Cherenkov momentum threshold, P_{thres} , is dependent upon the mass, m , of the charged particle moving through the media,

$$P_{thres} = \frac{m}{\sqrt{n^2 - 1}} \quad (2.3)$$

For water, where $n = 1.33$, the Cherenkov threshold momentum and energy for various particles are given in Table 2.3. In contrast, γ -rays are detected indirectly via the combination of photons generated by Compton scattering and pair production. The threshold for detection in the SK detector is typically higher than the threshold for photon production. This is due to the fact that the attenuation of photons in the water means that typically $\sim 75\%$ of Cherenkov photons reach the ID PMTs. Then the collection and quantum efficiencies described in subsection 2.1.1 result in the number of detected photons being lower than the number of photons which reach the PMTs.

Particle	Threshold Momentum (MeV)	Threshold Energy (MeV)
Electron	0.5828	0.7751
Muon	120.5	160.3
Pion	159.2	211.7
Proton	1070.0	1423.1

Table 2.3: The threshold momentum and energy for a particle to generate Cherenkov light in ultrapure water, as calculated in Equation 2.2 in ultrapure water which has refractive index $n = 1.33$.

The Frank-Tamm equation [97] describes the relationship between the number of Cherenkov photons generated per unit length, dN/dx , the wavelength of the photons generated, λ , and the relativistic velocity of the charged particle,

$$\frac{d^2N}{dxd\lambda} = 2\pi\alpha \left(1 - \frac{1}{n^2\beta^2}\right) \frac{1}{\lambda^2}. \quad (2.4)$$

where α is the fine structure constant. For a 100MeV momentum electron, approximately 330 photons will be produced per centimeter in the $300\text{nm} \leq \lambda \leq 700\text{nm}$ region which the ID PMTs are most sensitive to [80].

2.2 The Tokai to Kamioka Experiment

The Tokai to Kamioka (T2K) experiment is a long-baseline neutrino oscillation experiment located in Japan. Proposed in the early 2000s [98,99] to replace K2K [100], T2K was designed to observe electron neutrino appearance whilst precisely measuring the oscillation parameters associated with muon neutrino disappearance [101]. The experiment consists of a neutrino beam generated at the Japan Proton Accelerator Research Complex (J-PARC), a suite of near detectors situated 280m from the beam target, and the Super Kamiokande far detector positioned at a 295km baseline. The cross-section view of the T2K experiment is drawn in Figure 2.4.

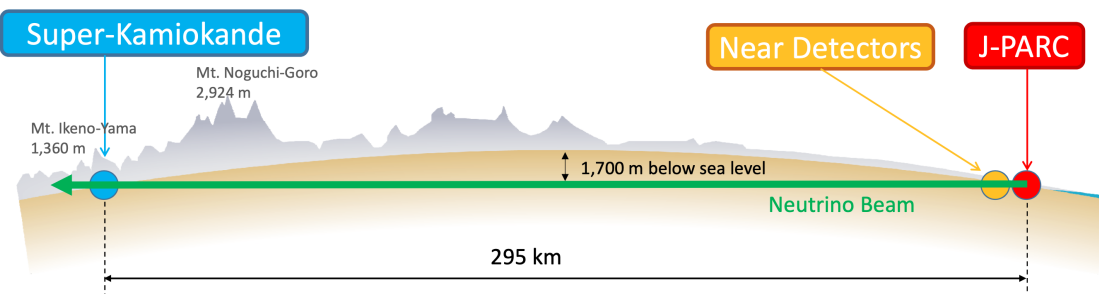


Figure 2.4: The cross-section view of the Tokai to Kamioka experiment illustrating the beam generation facility at J-PARC, the near detector situated at a baseline of 280m and the Super Kamiokande far detector situated 295km from the beam target.

The T2K collaboration makes world-leading measurements of the $\sin^2(\theta_{23})$, Δm_{23}^2 , and δ_{CP} oscillation parameters. Improvements in the precision and accuracy of parameter estimates are still being made by including new data samples and developing the models which describe the neutrino interactions and detector responses [DB: Link](#) to Christophe's slides from Nu2022. Electron neutrino appearance was first observed

668 at T2K in 2014 [102] which accompanied a 7.3σ significance of a non-zero $\sin^2(\theta_{13})$
 669 measurement.

670 The near detectors provide constraints on the beam flux and cross-section model
 671 parameters used within the fit by observing the unoscillated neutrino beam. There
 672 are a host of detectors situated in the near detector hall (As illustrated in Figure 2.5);
 673 ND280 (subsection 2.2.2), INGRID (subsection 2.2.3), NINJA [103], WAGASCI [104],
 674 and Baby-MIND [105]. The latter three are not currently used within the oscillation
 675 analysis presented within this thesis.

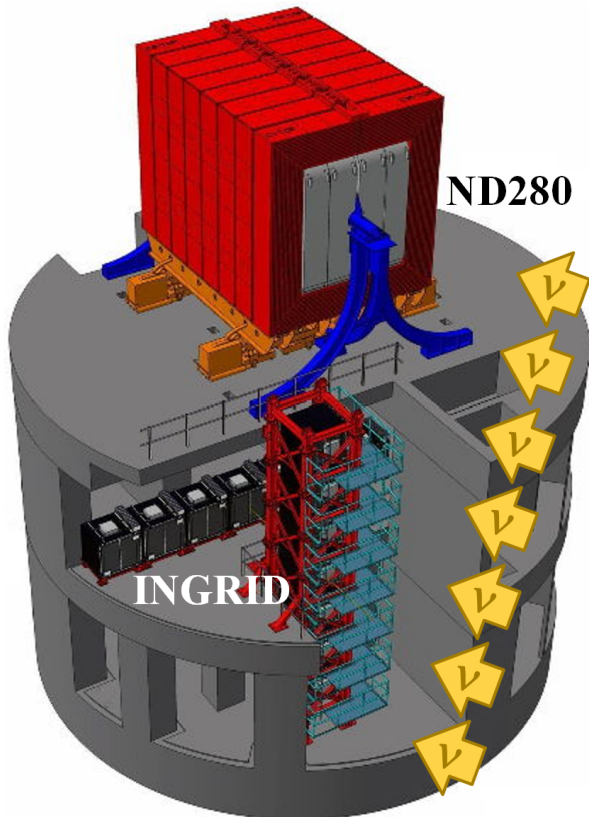


Figure 2.5: The near detector suite for the T2K experiment showing the ND280 and INGRID detectors. The distance between the detectors and the beam target is 280m.

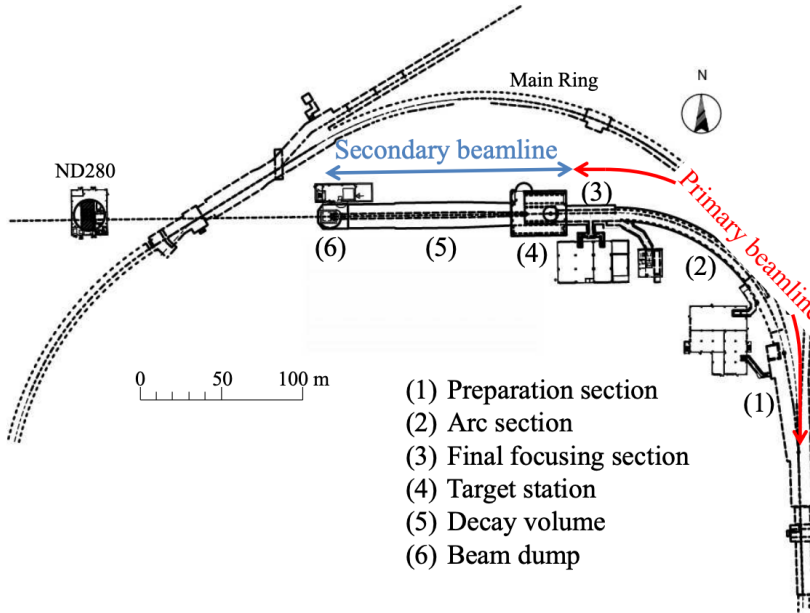
676 Whilst this thesis presents the ND280 in terms of its purpose for the oscillation
 677 analysis, the detector can also make many cross-section measurements at neutrino
 678 energies of $O(1)\text{GeV}$ for the different targets within the detector [106, 107]. These

679 measurements are of equal importance as they can lead the way in determining the
680 model parameters used in the interaction models for the future high-precision era of
681 neutrino physics.

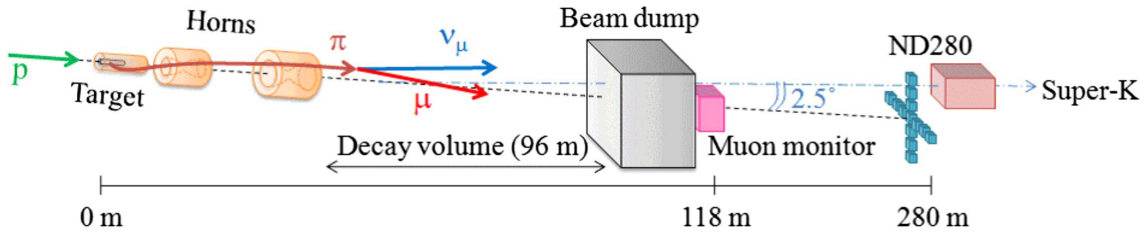
682 2.2.1 The Neutrino Beam

683 The neutrino beam used within the T2K experiment is described in [57, 108] and
684 summarised below. The accelerating facility at J-PARC is composed of two sections; the
685 primary and secondary beamlines. Figure 2.6 illustrates a schematic of the beamline,
686 focusing mostly on the components of the secondary beamline. The primary beamline
687 has three accelerators that progressively accelerate protons; a linear accelerator, a rapid-
688 cycling synchrotron, and the main-ring (MR) synchrotron. Once fully accelerated by
689 the MR, the protons have a kinetic energy of 30GeV. Eight bunches of these protons,
690 separated by 500ns, are extracted per “spill” from the MR and directed towards a
691 graphite target (A rod of length 91.4cm and diameter 2.6cm). Spills are extracted at
692 0.5Hz with $\sim 3 \times 10^{14}$ protons contained per spill.

693 The secondary beamline consists of three main components; the target station, the
694 decay volume, and the beam dump. The target station is comprised of the target, beam
695 monitors, and three magnetic focusing horns. The proton beam interacts with the
696 graphite target to form a secondary beam of mostly pions and kaons. The secondary
697 beam travels through a 96m long decay volume, generating neutrinos through the
698 following decays [57],



(a) Primary and secondary beamline



(b) Secondary beamline

Figure 2.6: Top panel: Bird's eye view of the most relevant part of primary and secondary beamline used within the T2K experiment. The primary beamline is the main-ring proton synchrotron, kicker magnet, and graphite target. The secondary beamline consists of the three focusing horns, decay volume, and beam dump. Figure taken from [108]. Bottom panel: The side-view of the secondary beamline including the focusing horns, beam dump and neutrino detectors. Figure taken from [109].

$$\pi^+ \rightarrow \mu^+ + \nu_\mu$$

$$\pi^- \rightarrow \mu^- + \bar{\nu}_\mu$$

$$K^+ \rightarrow \mu^+ + \nu_\mu$$

$$K^- \rightarrow \mu^- + \bar{\nu}_\mu$$

$$\rightarrow \pi^0 + e^+ + \nu_e$$

$$\rightarrow \pi^0 + e^- + \bar{\nu}_e$$

$$\rightarrow \pi^0 + \mu^+ + \nu_\mu$$

$$\rightarrow \pi^0 + \mu^- + \bar{\nu}_\mu$$

$$K_L^0 \rightarrow \pi^- + e^+ + \nu_e$$

$$K_L^0 \rightarrow \pi^+ + e^- + \bar{\nu}_e$$

$$\rightarrow \pi^- + \mu^+ + \nu_\mu$$

$$\rightarrow \pi^+ + \mu^- + \bar{\nu}_\mu$$

$$\mu^+ \rightarrow e^+ + \bar{\nu}_\mu + \nu_e$$

$$\mu^- \rightarrow e^- + \nu_\mu + \bar{\nu}_e$$

The electrically charged component of the secondary beam is focused towards the far detector by the three magnetic horns. These horns direct charged particles of a particular polarity towards SK whilst defocusing the oppositely charged particles. This allows a mostly neutrino or mostly antineutrino beam to be used within the experiment, denoted as “forward horn current (FHC)” or “reverse horn current (RHC)” respectively.

Figure 2.7 illustrates the different contributions to the FHC and RHC neutrino flux. The low energy flux is dominated by the decay of pions whereas kaon decay becomes the dominant source of neutrinos for $E_\nu > 3\text{GeV}$. The “wrong-sign” component, which is the $\bar{\nu}_\mu$ background in a ν_μ beam, and the intrinsic irreducible ν_e background are predominantly due to muon decay for $E_\nu < 2\text{GeV}$. As the antineutrino cross-section is smaller than the neutrino cross-section, the wrong-sign component is more dominant in the RHC beam as compared to that in the FHC beam.

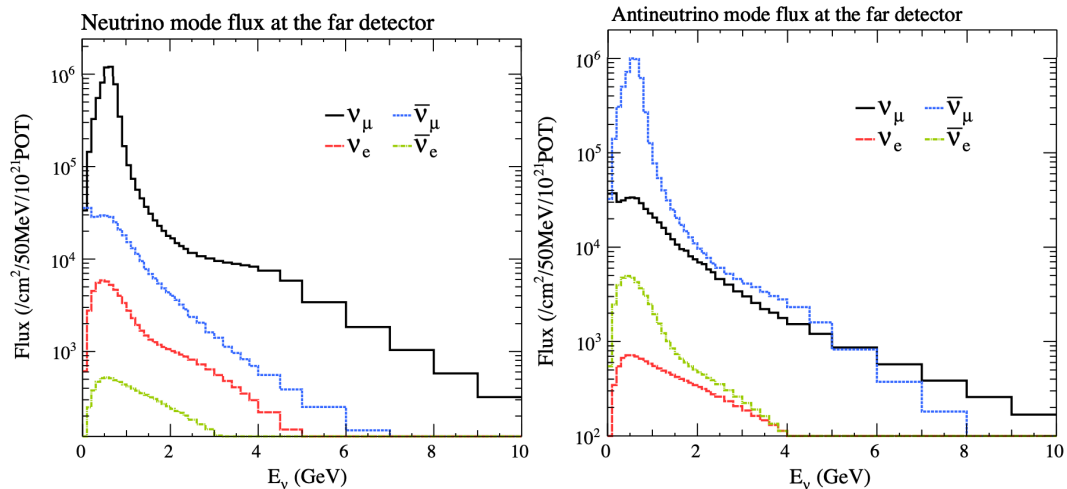


Figure 2.7: The Monte Carlo prediction of the energy spectrum for each flavour of neutrino (ν_e , $\bar{\nu}_e$, ν_μ and $\bar{\nu}_\mu$) in the neutrino dominated beam FHC mode (Left) and antineutrino dominated beam RHC mode (Right) expected at SK. Taken from [110].

The beam dump, situated at the end of the decay volume, stops all charged particles other than highly energetic muons ($p_\mu > 5\text{GeV}$). The MuMon detector monitors the

⁷¹⁵ penetrating muons to determine the beam direction and intensity which is used to
⁷¹⁶ constrain some of the beam flux systematics within the analysis [109, 111].

⁷¹⁷ The T2K experiment uses an off-axis beam to narrow the neutrino energy distribution.
⁷¹⁸ This was the first implementation of this technique in a long-baseline neutrino
⁷¹⁹ oscillation experiment after its original proposal [112]. Pion decay, $\pi \rightarrow \mu + \nu_\mu$, is a
⁷²⁰ two-body decay. Consequently, the neutrino energy, E_ν , can be determined based on
⁷²¹ the pion energy, E_π , and the angle at which the neutrino is emitted, θ ,

$$E_\nu = \frac{m_\pi^2 - m_\mu^2}{2(E_\pi - p_\pi \cos(\theta))}, \quad (2.5)$$

⁷²² where m_π and m_μ are the mass of the pion and muon respectively. For a fixed
⁷²³ energy pion, the neutrino energy distribution is dependent upon the angle at which
⁷²⁴ the neutrinos are observed from the initial pion beam direction. For the 295km
⁷²⁵ baseline at T2K, $E_\nu = 0.6\text{GeV}$ maximises the electron neutrino appearance probability,
⁷²⁶ $P(\nu_\mu \rightarrow \nu_e)$, whilst minimising the muon disappearance probability, $P(\nu_\mu \rightarrow \nu_\mu)$.
⁷²⁷ Figure 2.8 illustrates the neutrino energy distribution for a range of off-axis angles, as
⁷²⁸ well as the oscillation probabilities most relevant to T2K.

⁷²⁹ 2.2.2 The Near Detector at 280m

⁷³⁰ Whilst all the near detectors are situated in the same “pit” located at 280m from the
⁷³¹ beamline, the “ND280” detector is the off-axis detector which is situated at the same
⁷³² off-axis angle as the Super-Kamiokande far detector. It has two primary functions;
⁷³³ firstly it measures the neutrino flux and secondly it counts the event rates of different
⁷³⁴ types of neutrino interactions. Both of these constrain the flux and cross-section

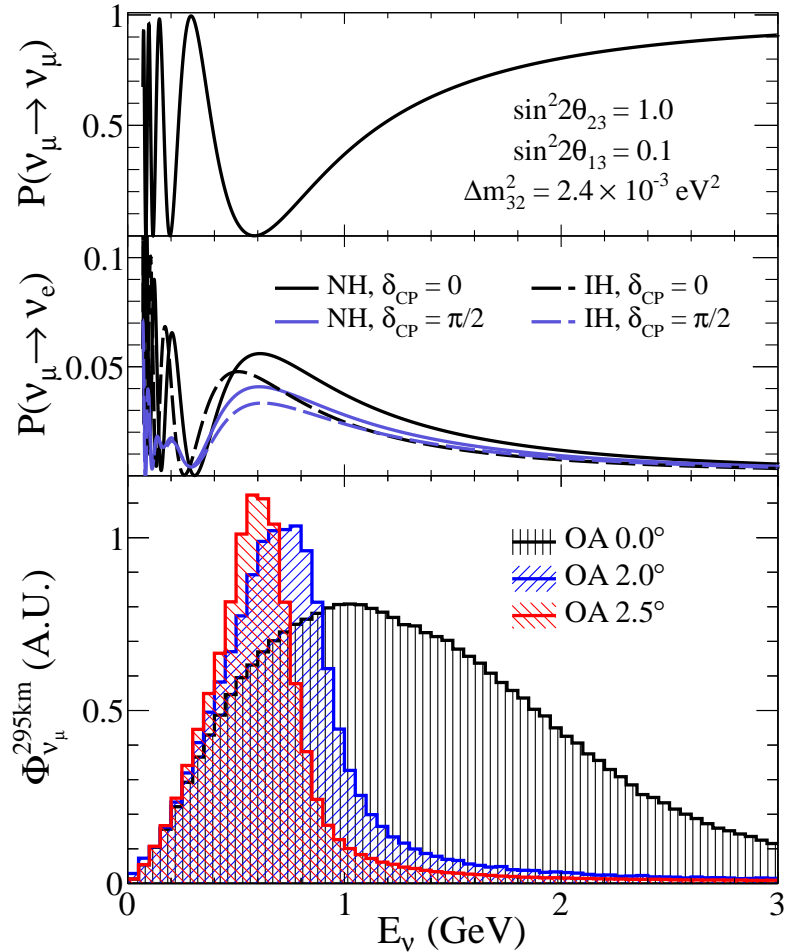


Figure 2.8: Top panel: T2K muon neutrino disappearance probability as a function of neutrino energy. Middle panel: T2K electron neutrino appearance probability as a function of neutrino energy. Bottom panel: The neutrino flux distribution for three different off-axis angles (Arbitrary units) as a function of neutrino energy.

735 systematics invoked within the model for a more accurate prediction of the expected
 736 event rate at the far detector.

737 As illustrated in Figure 2.9, the ND280 detector consists of several sub-detectors.
 738 The most important part of the detector for this analysis is the tracker region. This is
 739 comprised of two time projection chambers (TPCs) sandwiched between three fine
 740 grain detectors (FGDs). The FGDs contain both hydrocarbon plastics and water tar-
 741 gets for neutrino interactions and provide track reconstruction near the interaction
 742 vertex. The emitted charged particles can then propagate into the TPCs which pro-
 743 vide particle identification and momentum reconstruction. The FGDs and TPCs are

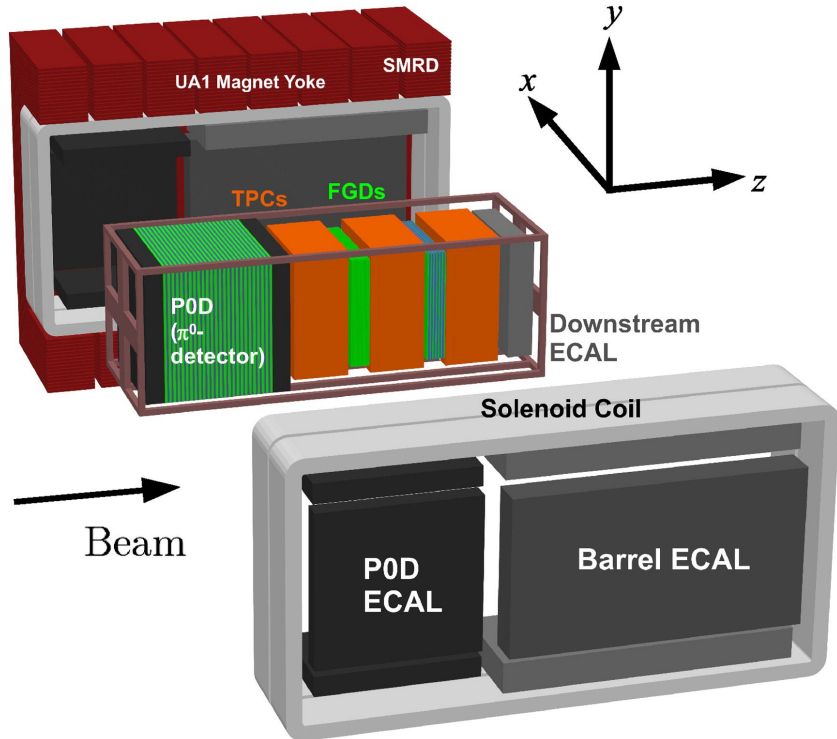


Figure 2.9: The components of the ND280 detector. The neutrino beam travels from left to right. Taken from [108].

⁷⁴⁴ further described in subsubsection 2.2.2.1 and subsubsection 2.2.2.2 respectively. The
⁷⁴⁵ electromagnetic calorimeter (ECAL) encapsulates the tracker region alongside the π^0
⁷⁴⁶ detector (P0D). The ECAL measures the deposited energy from photons emitted from
⁷⁴⁷ interactions within the FGD. The P0D constrains the cross-section of neutral current
⁷⁴⁸ interactions which generate neutral pions, which is one of the largest backgrounds in
⁷⁴⁹ the electron neutrino appearance oscillation channel. The P0D and ECAL detectors
⁷⁵⁰ are detailed in subsubsection 2.2.2.3 and subsubsection 2.2.2.4 respectively. The entire
⁷⁵¹ detector is located within a large yolk magnet which produces a 0.2T magnetic field.
⁷⁵² This design of the magnet also includes a scintillating detector called the side muon
⁷⁵³ range detector (SMRD) which is used to track high-angle muons as well as acting as a
⁷⁵⁴ cosmic veto. The SMRD is described in subsubsection 2.2.2.5.

755 2.2.2.1 Fine Grained Detectors

756 The T2K tracker region is comprised of two fine grained detectors (FGD) and three
757 Time Projection Chambers (TPC). A detailed description of the FGD design, construc-
758 tion, and assembly is found in [113] and summarised below. The FGDs are the primary
759 target for neutrino interactions with a mass of 1.1 tonnes per FGD. Alongside this,
760 the FGDs are designed to be able to track short-range particles which do not exit the
761 FGD. Typically, short-range particles are low momentum and are observed as tracks
762 that deposit a large amount of energy per unit length. This means the FGD needs
763 good granularity to resolve these particles. The FGDs have the best timing resolution
764 ($\sim 3\text{ns}$) of any of the sub-detectors of the ND280 detector. As such, the FGDs are
765 used for time of flight measurements to determine forward going positively charged
766 particles from backward going negatively charged particles. Finally, any tracks which
767 pass through multiple sub-detectors are required to be track matched to the FGD.

768 Both FDGs are made from square scintillator planes of side length 186cm and width
769 2.02cm. Each plane consists of two layers of 192 scintillator bars in an XY orientation.
770 A wave-length shift fiber is threaded through the center of each bar and is read out by
771 a multi-photon pixel counter (MPPC). FGD1 is the most upstream of the two FGDs
772 and contains 15 planes of carbon plastic scintillator which is a common target in
773 external neutrino scattering data. As the far detector is a pure water target, 7 of the 15
774 scintillator planes in FGD2 have been replaced with a hybrid water-scintillator target.
775 Due to the complexity of the nucleus, nuclear effects can not be extrapolated between
776 different nuclei. Therefore having the ability to take data on one target which is the
777 same as external data and another target which is the same as the far detector target is
778 beneficial for reliable model parameter estimates.

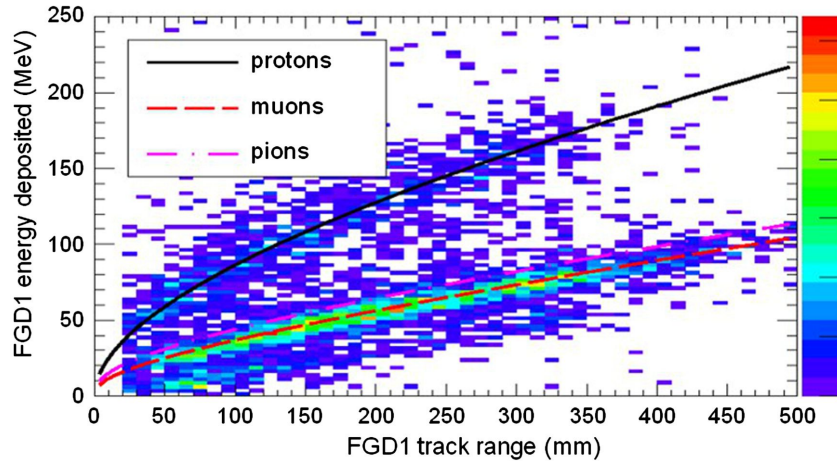


Figure 2.10: Comparison of data to Monte Carlo prediction of integrated deposited energy as a function of track length for particles that stopped in FGD1. Taken from [113].

779 The integrated deposited energy is used for particle identification. The FGD
780 can distinguish protons from other charged particles by comparing the integrated
781 deposited energy from data to Monte Carlo prediction as seen in Figure 2.10.

782 2.2.2.2 Time Projection Chambers

783 The majority of particle identification and momentum measurements within ND280
784 are provided by three Time Projection Chambers (TPCs) [114]. The TPCs are located
785 on either side of the FGDs. They are located inside of the magnetic field meaning the
786 momentum of a charged particle can be determined from the bending of the track.

787 Each TPC module consists of two gas-tight boxes, as shown in Figure 2.11, which
788 are made of non-magnetic material. The outer box is filled with CO₂ which acts as
789 an electrical insulator between the inner box and the ground. The inner box forms
790 the field cage which produces a uniform electric drift field of $\sim 275\text{V/cm}$ and an
791 argon gas mixture. Charged particles moving through this gas mixture ionize the gas
792 mixture. The ionised charge is drifted towards micromega detectors which measure
793 the ionization charge. The time and position information in the readout allows a
794 three-dimensional image of the neutrino interaction.

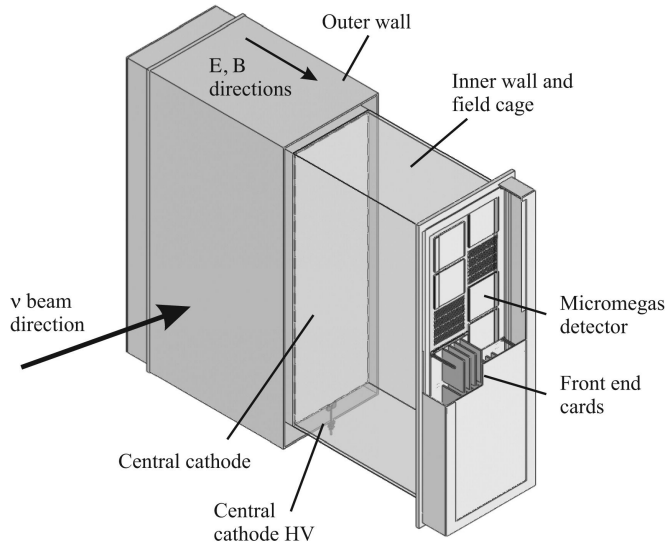


Figure 2.11: Schematic design of a Time Projection Chamber detector. Taken from [114].

The particle identification of tracks that pass through the TPCs is performed using

dE/dx measurements. Figure 2.12 illustrates the data to Monte Carlo distributions

of the energy lost by a charged particle passing through the TPC as a function of the

reconstructed particle momentum. The resolution is $7.8 \pm 0.2\%$ meaning that electrons

and muons can be distinguished. This allows reliable measurements of the intrinsic ν_e

component of the beam.

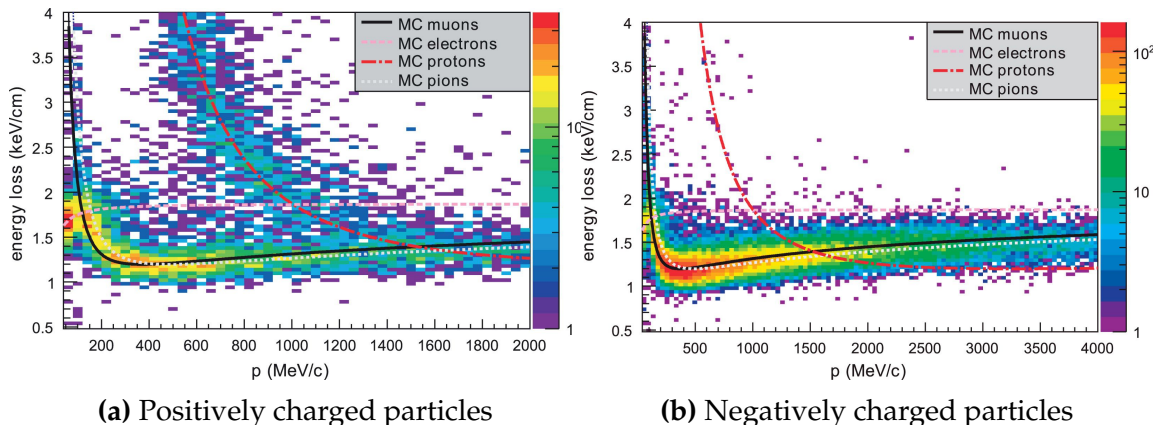


Figure 2.12: The distribution of energy loss as a function of reconstructed momentum for charged particles passing through the TPC, comparing data to Monte Carlo prediction. Taken from [114].

⁸⁰¹ 2.2.2.3 π^0 Detector

⁸⁰² If one of the γ -rays from a $\pi^0 \rightarrow 2\gamma$ decay is missed at the far detector, the reconstruction will determine that event to be electron-like. This is one of the main backgrounds hindering the electron neutrino appearance searches. Therefore, the π^0 detector (P0D) measures the cross-section of the neutral current induced neutral pion production on a water target.

⁸⁰⁷ The P0D is a cube of approximately 2.5m length. The P0D consists of layers of scintillating bars, brass and lead sheets, and water bags as illustrated in Figure 2.13. ⁸⁰⁸ Two electromagnetic calorimeters are positioned at the most upstream and most downstream position in the sub-detector and the water target is situated in between them. The scintillator layers are built from two triangular bars orientated in opposite directions to form a rectangular layer. Each triangular scintillator bar is threaded with optical fiber which is read out by MPPCs. The high-Z brass and lead regions produce electron showers from the photons emitted in π^0 decay.

⁸¹⁵ The sub-detector can generate measurements of NC1 π^0 cross-sections on a water target by measuring the event rate both with and without the water target, with the cross-section on a water target being determined as the difference. The total active mass is 16.1 tonnes when filled with water and 13.3 tonnes when empty.

⁸¹⁹ 2.2.2.4 Electromagnetic Calorimeter

⁸²⁰ The electromagnetic calorimeter [116] (ECal) encapsulates the P0D and tracking sub-detectors. Its primary purpose is to aid π^0 reconstruction from any interaction in the tracker. To do this, it measures the energy and direction of photon showers from $\pi^0 \rightarrow 2\gamma$ decay. It can also distinguish pion and muon tracks depending on the shape of the photon shower deposited.

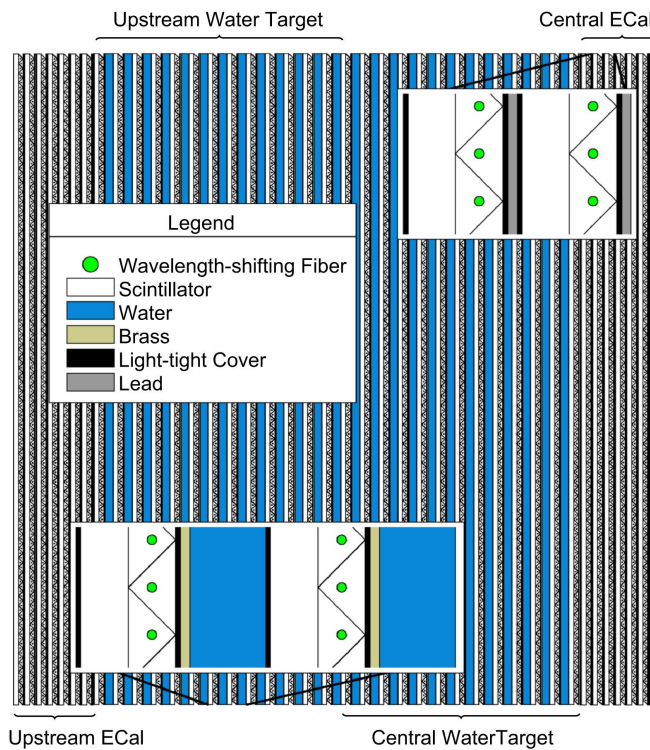


Figure 2.13: A schematic of the P0D side-view. Taken from [115].

825 The ECal is comprised of three sections; the P0D ECal which surrounds the P0D,
 826 the barrel ECal which encompasses the tracking region, and the downstream ECal
 827 which is situated downstream of the tracker region. The barrel and downstream
 828 ECals are tracking calorimeters that focus on electromagnetic showers from high-angle
 829 particles emitted from the tracking sub-detectors. Particularly in the TPC, high-angle
 830 tracks (those which travel perpendicularly to the beam-axis) can travel along a single
 831 scintillator bar resulting in very few hits. The width of the barrel and downstream
 832 ECal corresponds to ~ 11 electron radiation lengths to ensure $\sim 50\%$ of the energy of
 833 the π^0 is contained. As the P0D has its own calorimetry which reconstructs showers,
 834 the P0D ECal determines the energy which escapes the P0D.

835 Each ECal is constructed of multiple layers of scintillating bars sandwiched between
 836 lead sheets. The scintillating bars are threaded with optical fiber and read out by
 837 MPPCs. Each sequential layer of the scintillator is orientated perpendicular to the
 838 previous which allows a two-dimensional readout, which when temporal, information

⁸³⁹ is included results in three-dimension event displays. The target mass of the P0D ECal,
⁸⁴⁰ barrel ECal, and downstream ECal are 1.50, 4.80 and 6.62 tonnes respectively.

⁸⁴¹ **2.2.2.5 Side Muon Range Detector**

⁸⁴² As illustrated in Figure 2.9, the ECal, FGDs, P0D, and TPCs are enclosed within the
⁸⁴³ UA1 magnet. Originally designed for the NOMAD [117] experiment and reconditioned
⁸⁴⁴ for use in the T2K experiment [118], the UA1 magnet provides a uniform horizontal
⁸⁴⁵ magnetic field of $0.2 \pm 2 \times 10^{-4}$ T.

⁸⁴⁶ Built into the UA1 magnet, the side muon range detector (SMRD) [119] monitors
⁸⁴⁷ high-energy muons which leave the tracking region and permeate through the ECal.
⁸⁴⁸ It additionally acts as a cosmic muon veto and trigger.

⁸⁴⁹ **2.2.3 The Interactive Neutrino GRID**

⁸⁵⁰ The Interactive Neutrino GRID (INGRID) detector is situated within the same “pit” as
⁸⁵¹ the other near detectors. It is aligned with the beam in the “on-axis” position and mea-
⁸⁵² sures the beam direction, spread, and intensity. The detector was originally designed
⁸⁵³ with 16 identical modules [108] (two modules have since been decommissioned) and a
⁸⁵⁴ “proton” module. The design of the detector is cross-shaped with length and height
⁸⁵⁵ 10m × 10m as illustrated in Figure 2.14.

⁸⁵⁶ Each module is composed of iron sheets interlaced with eleven tracking scintillator
⁸⁵⁷ planes for a total target mass of 7.1 tonnes per module. The scintillator design is an X-Y
⁸⁵⁸ pattern of 24 bars in both orientations, where each bar contains wave-length shifting
⁸⁵⁹ fibers which are connected to multi-pixel photon counters (MPPCs). The MPPCs
⁸⁶⁰ convert detected photons into electrical signals via photodiodes. This is then read
⁸⁶¹ out by Trip-T front-end electronics [120] and passed to the readout merging modules

⁸⁶² along with timing information from the clock module. Each module is encapsulated
⁸⁶³ inside veto planes to aid the rejection of charged particles entering the module.

⁸⁶⁴ The proton module is different from the other modules in that it consists of entirely
⁸⁶⁵ scintillator planes with no iron target. The scintillator bars are also smaller than those
⁸⁶⁶ used in the other modules to increase the granularity of the detector and improve
⁸⁶⁷ tracking capabilities. The module sits in the center of the beamline and is designed to
⁸⁶⁸ give precise measurements of quasi-elastic charged current interactions to evaluate
⁸⁶⁹ the performance of the Monte Carlo simulation of the beamline.

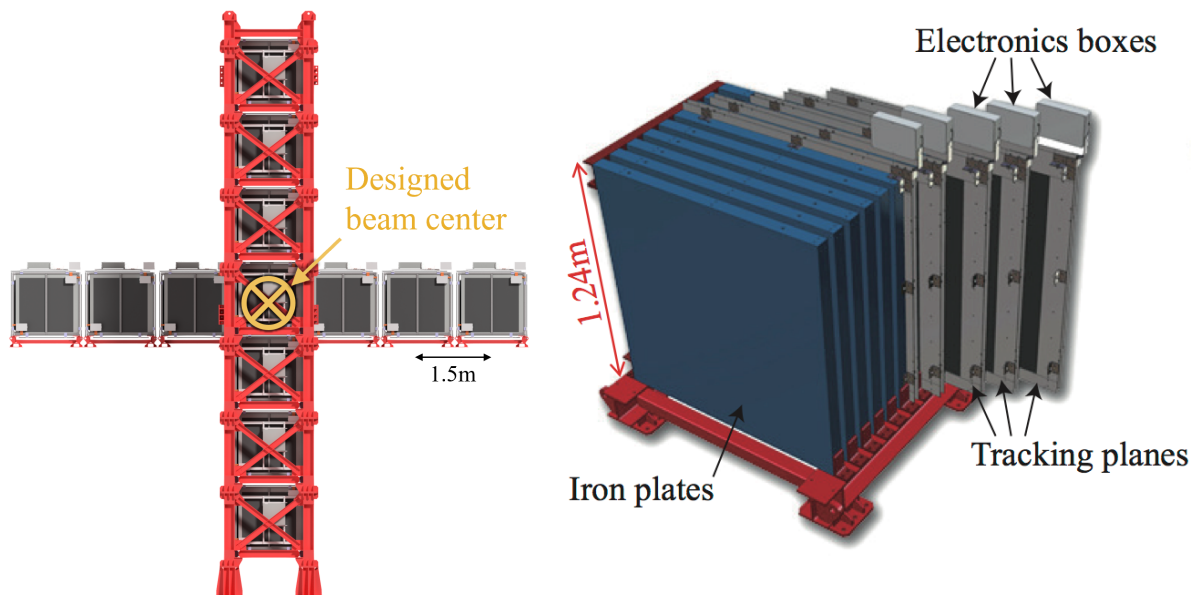


Figure 2.14: Left panel: The Interactive Neutrino GRID on-axis Detector. 14 modules are arranged in a cross-shape configuration, with the center modules being directly aligned with the on-axis beam. Right panel: The layout of a single module of the INGRID detector. Both figures are recreated from [108].

⁸⁷⁰ The INGRID detector can measure the beam direction to an uncertainty of 0.4mrad
⁸⁷¹ and the beam center within a resolution of 10cm [108]. The beam direction in both the
⁸⁷² vertical and horizontal directions is discussed in [121] and it is found to be in good
⁸⁷³ agreement with the MUMON monitor described in subsection 2.2.1.

874 **Chapter 3**

875 **Bayesian Statistics and Markov Chain
Monte Carlo Techniques**

877 The analysis throughout this thesis is based upon a Bayesian oscillation analysis. To
878 extract the oscillation parameters, a Markov Chain Monte Carlo (MCMC) method is
879 used. This chapter explains the theory of how parameter estimates can be determined
880 using this technique and condenses the material found in the literature [122–125].

881 The oscillation parameter determination presented within this thesis is built upon a
882 simultaneous fit to the near detector, far detector beam, and atmospheric neutrino data.
883 In total, there are four oscillation parameters of interest ($\sin^2(\theta_{23})$, $\sin^2(\theta_{13})$, Δm_{23}^2 ,
884 and δ_{CP}), two oscillation parameters to which this study will not be sensitive ($\sin^2(\theta_{12})$
885 , Δm_{12}^2) and many nuisance parameters that control the systematic uncertainty models
886 invoked within this study. The systematic uncertainties can be grouped into categories
887 depending on how they are defined; 574 bin-normalisations due to the near detector
888 response, 45 bin-normalisations to describe the far detector response to neutrino beam
889 events, 27 parameters to describe the detector response to atmospheric neutrino events,
890 100 to model the bin-normalisation due to beam flux uncertainties, 18 which model the
891 atmospheric flux uncertainties, and 87 to describe the correlated cross-section model.
892 An alternative parameterisation, where the far detector response is correlated between
893 the beam and atmospheric samples, replaces the bin-normalisation parameters with
894 224 shift and smear systematics. Section [DB: Link to Systematics Chapter](#) describes
895 the systematic model in more depth.

896 The MCMC technique generates a multi-dimensional probability distribution across
897 all of the model parameters used in the fit. To determine the parameter estimate of a
898 single parameter, this multi-dimensional object is integrated over all other parameters.
899 This process is called Marginalisation and is further described in subsection 3.3.1.
900 Monte Carlo techniques approximate the probability distribution of each parameter
901 within the limit of generating infinite samples. As ever, generating a large number of
902 samples is time and resource-dependent. Therefore, an MCMC technique is utilised
903 within this analysis to reduce the required number of steps to sufficiently sample the
904 parameter space. This technique is described in further detail in subsection 3.2.1.

905 **3.1 Bayesian Statistics**

906 According to Bayesian Inference, observables and parameters of a statistical model are
907 treated on an equal footing. To estimate model parameters $\vec{\theta}$ from some data D , one
908 needs to define the joint probability distribution $P(D|\vec{\theta})$ which can be described as the
909 prior distribution for model parameters $P(\vec{\theta})$ and the likelihood of the data given the
910 model parameters $P(D|\vec{\theta})$,

$$P(D, \vec{\theta}) = P(D|\vec{\theta})P(\vec{\theta}). \quad (3.1)$$

911 The prior distribution, $P(\vec{\theta})$, describes all previous knowledge about the parameters
912 within the model. For example, if the risk of developing health problems is known
913 to increase with age, the prior distribution would describe the increase. For the
914 purpose of this analysis, the prior distribution is typically the best-fit values taken
915 from external data measurements with a Gaussian uncertainty. The prior distribution

can also contain correlations between model parameters. In an analysis using Monte Carlo techniques, the likelihood of measuring some data assuming some set of model parameters is calculated by comparing the Monte Carlo prediction generated at that particular set of model parameters to the data.

It is parameter estimation that is important for this analysis and as such, we apply Bayes' theorem [126]. To calculate the probability for each parameter to have a certain value given the observed data $P(\vec{\theta}|D)$, known as the posterior distribution (often termed the posterior). This can be expressed as

$$P(\vec{\theta}|D) = \frac{P(D|\vec{\theta})P(\vec{\theta})}{\int P(D|\vec{\theta})P(\vec{\theta})d\vec{\theta}}. \quad (3.2)$$

The denominator in Equation 3.2 is the integral of the joint probability distribution over all values of all parameters used within the fit. For brevity, we say that the posterior distribution is

$$P(\vec{\theta}|D)\alpha P(D|\vec{\theta})P(\vec{\theta}). \quad (3.3)$$

In subsection 3.3.1, we see that for the cases used within this analysis, it is reasonable to know the posterior to some normalisation constant.

3.2 Monte Carlo Simulation

Monte Carlo techniques are used to numerically solve a complex problem that does not necessarily have an analytical solution. These techniques rely on building a large

932 ensemble of samples from an unknown distribution and then using the ensemble to
933 approximate the properties of the distribution.

934 An example that uses Monte Carlo techniques is to calculate the area underneath
935 a curve. For example, take the problem of calculating the area under a straight line
936 with gradient $M = 0.4$ and intercept $C = 1.0$. Analytically, one can calculate the area
937 under the line is equal to 30 units for $0 \leq x \leq 10$. Using Monte Carlo techniques,
938 one can calculate the area under this line by throwing many random values for the x
939 and y components of each sample and then calculating whether that point falls below
940 the line. The area can then be calculated by the ratio of points below the line to the
941 total number of samples thrown multiplied by the total area in which samples were
942 scattered. The study is shown in Figure 3.1 highlights this technique and finds the area
943 under the curve to be 29.9 compared to an analytical solution of 30.0. The deviation
944 of the numerical to analytical solution can be attributed to the number of samples
945 used in the study. The accuracy of the approximation in which the properties of the
946 Monte Carlo samples replicate those of the desired distribution is dependent on the
947 number of samples used. Replicating this study with a differing number of Monte
948 Carlo samples used in each study (As shown in Figure 3.2) highlights how the Monte
949 Carlo techniques are only accurate within the limit of a high number of samples.

950 Whilst the above example has an analytical solution, these techniques are just as
951 applicable to complex solutions. Clearly, any numerical solution is only as useful as its
952 efficiency. As discussed, the accuracy of the Monte Carlo technique is dependent upon
953 the number of samples generated to approximate the properties of the distribution.
954 Furthermore, if the positions at which the samples are evaluated are not 'cleverly'
955 picked, the efficiency of the Monte Carlo technique significantly drops. Given the
956 example in Figure 3.1, if the region in which the samples are scattered significantly
957 extends passed the region of interest, many calculations will be calculated but do

not add to the ability of the Monte Carlo technique to achieve the correct result. For instance, any sample evaluated at a $y \geq 5$ could be removed without affecting the final result. This does bring in an aspect of the ‘chicken and egg’ problem in that to achieve efficient sampling, one needs to know the distribution beforehand.

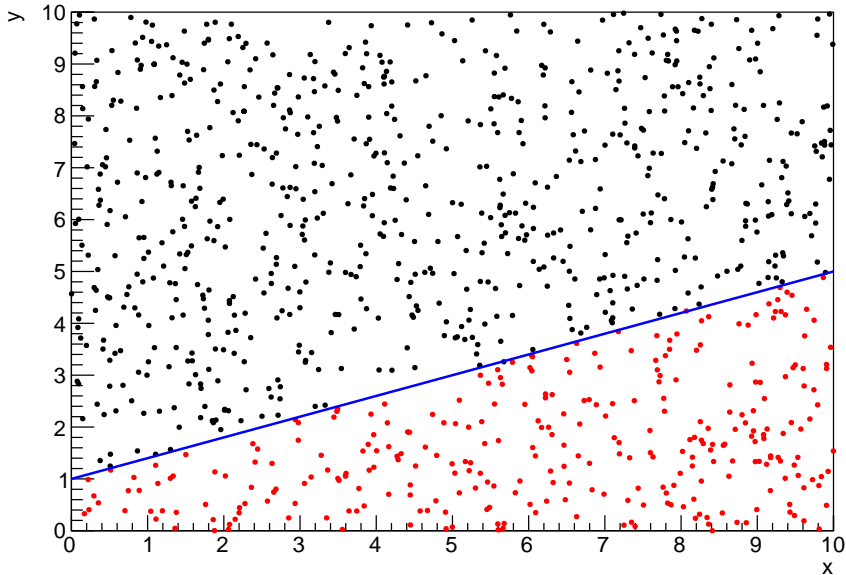


Figure 3.1: Example of using Monte Carlo techniques to find the area under the blue line. The gradient and intercept of the line are 0.4 and 1.0 respectively. The area found to be under the curve using one thousand samples is 29.9 units.

3.2.1 Markov Chain Monte Carlo

This analysis utilises a multi-dimensional probability distribution, with some dimensions being significantly more constrained than others. This could be from prior knowledge of parameter distributions from external data or un-physical regions in which parameters can not exist. Consequently, the Monte Carlo techniques used need to be as efficient as possible. For this analysis, the Markov Chain Monte Carlo (MCMC) technique is chosen. An MCMC technique is a Monte Carlo technique that uses a Markov chain to select which points at which to sample the parameter distribution.

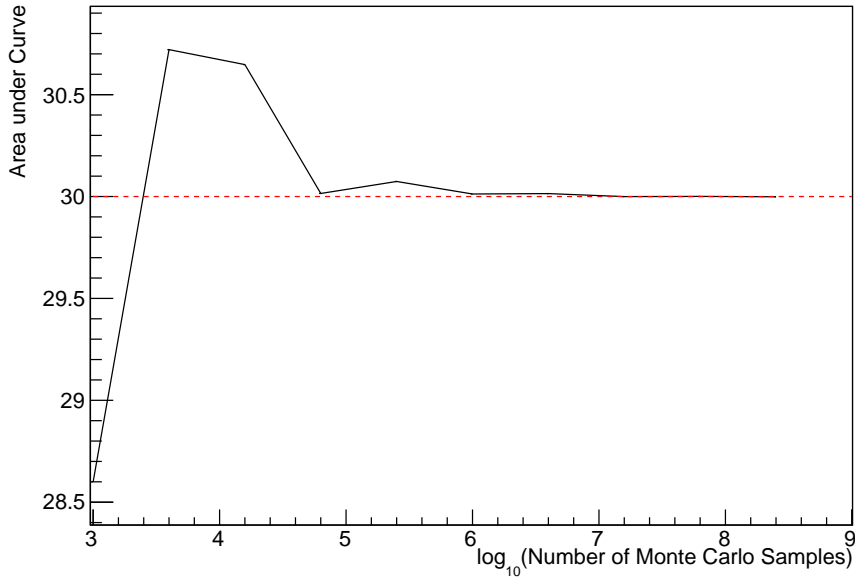


Figure 3.2: The area under a line of gradient 0.4 and intercept 1.0 for the range $0 \leq x \leq 10$ as calculated using Monte Carlo techniques as a function of the number of samples used in each repetition. The analytical solution to the area is 30 units as given by the red line.

970 This technique performs a semi-random stochastic walk through the allowable pa-
 971 rameter space. This builds a posterior distribution which has the property that the
 972 density of sampled points is proportional to the probability density of that parame-
 973 ter. This does mean that the samples produced by this technique are not statistically
 974 independent but they will cover the space of the distribution.

975 A Markov chain functions by selecting the position of step \vec{x}_{i+1} based on the
 976 position of \vec{x}_i . The space in which the Markov chain selects samples is dependent
 977 upon the total number of parameters utilised within the fit, where a discrete point in
 978 this space is described by the N-dimensional space \vec{x} . In a perfectly operating Markov
 979 chain, the position of the next step depends solely on the previous step and not on the
 980 further history of the chain (\vec{x}_0, \vec{x}_1 , etc.). However, in solving the multi-dimensionality
 981 of the fit used within this analysis, each step becomes correlated with several of
 982 the steps preceding itself. This behaviour is further explained in subsection 3.2.3.
 983 Providing the MCMC chain is well optimised, it will begin to converge towards a

unique stationary distribution. The period between the chain's initial starting point and the convergence to the unique stationary distribution is colloquially known as the burn-in period. This is discussed further in subsection 3.2.3. Once the chain reaches the stationary distribution, all points sampled after that point will look like samples from that distribution.

Further details of the theories underpinning MCMC techniques are discussed in [123] but can be summarised by the requirement that the chain satisfies the three 'regularity conditions':

- Irreducibility: From every position in the parameter space \vec{x} , there must exist a non-zero probability for every other position in the parameter space to be reached.
- Recurrence: Once the chain arrives at the stationary distribution, every step following from that position must be samples from the same stationary distribution.
- Aperiodicity: The chain must not repeat the same sequence of steps at any point throughout the sampling period.

The output of the chain after burn-in (ie. the sampled points after the chain has reached the stationary distribution) can be used to approximate the posterior distribution and model parameters $\vec{\theta}$. To achieve the requirement that the unique stationary distribution found by the chain be the posterior distribution, one can use the Metropolis-Hastings algorithm. This guides the stochastic process depending on the likelihood of the current proposed step compared to that of the previous step. Implementation and other details of this technique are discussed in subsection 3.2.2.

1005 3.2.2 Metropolis-Hastings Algorithm

1006 As a requirement for MCMCs, the Markov chain implemented in this technique must
 1007 have a unique stationary distribution that is equivalent to the posterior distribution.
 1008 To ensure this requirement and that the regularity conditions are met, this analysis
 1009 utilises the Metropolis-Hastings (MH) algorithm [127, 128]. For the i^{th} step in the chain,
 1010 the MH algorithm determines the position in the parameter space to which the chain
 1011 moves to based on the current step, \vec{x}_i , and the proposed step, \vec{y}_{i+1} . The proposed step
 1012 is randomly selected from some proposal function $f(\vec{x}_{i+1}|\vec{x}_i)$, which depends solely
 1013 on the current step (ie. not the further history of the chain). The next step in the chain
 1014 \vec{x}_{i+1} can be either the current step or the proposed step determined by whether the
 1015 proposed step is accepted or rejected. To decide if the proposed step is selected, the
 1016 acceptance probability, $\alpha(\vec{x}_i, \vec{y}_i)$, is calculated as

$$\alpha(\vec{x}_i, \vec{y}_{i+1}) = \min\left(1, \frac{P(\vec{y}_{i+1}|D)f(\vec{x}_i|\vec{y}_{i+1})}{P(\vec{x}_i|D)f(\vec{y}_{i+1}|\vec{x}_i)}\right). \quad (3.4)$$

1017 Where $P(\vec{y}_{i+1}|D)$ is the posterior distribution as introduced in section 3.1. To
 1018 simplify this calculation, the proposal function is required to be symmetric such that
 1019 $f(\vec{x}_i|\vec{y}_{i+1}) = f(\vec{y}_{i+1}|\vec{x}_i)$. In practice, a multi-variate Gaussian distribution is used to
 1020 throw parameter proposals from. This reduces Equation 3.4 to

$$\alpha(\vec{x}_i, \vec{y}_{i+1}) = \min\left(1, \frac{P(\vec{y}_{i+1}|D)}{P(\vec{x}_i|D)}\right). \quad (3.5)$$

After calculating this quantity, a random number, β , is generated uniformly between 0 and 1. If $\beta \leq \alpha(\vec{x}_i, \vec{y}_{i+1})$, the proposed step is accepted. Otherwise, the chain sets the next step equal to the current step and this procedure is repeated. This can be interpreted as if the posterior probability of the proposed step is greater than that of the current step, ($P(\vec{y}_{i+1}|D) \geq P(\vec{x}_i|D)$), the proposed step will always be accepted. If the opposite is true, ($P(\vec{y}_{i+1}|D) \leq P(\vec{x}_i|D)$), the proposed step will be accepted with probability $P(\vec{x}_i|D)/P(\vec{y}_{i+1}|D)$. This ensures that the Markov chain does not get trapped in any local minima in the potentially non-Gaussian posterior distribution. The outcome of this technique is that the density of steps taken in a discrete region is directly proportional to the probability density in that region.

3.2.3 MCMC Optimisation

As discussed in subsection 3.2.2, the proposal function invoked within the MH algorithm can take any form and the chain will still converge to the stationary distribution. As discussed in [DB: Link to Analysis Strategy Section](#), this analysis performs the Monte Carlo reweighting on an event-by-event basis. This requires significant computational resources to perform a parameter fit. Therefore, the number of steps taken before the unique stationary distribution is found should be minimised as only steps after convergence add information to the fit. Furthermore, the chain should entirely cover the allowable parameter space to ensure that all values have been considered. Tuning the distance that the proposal function jumps between steps on a parameter-by-parameter basis can both minimise the length of the burn-in period and ensure that the correlation between step \vec{x}_i and \vec{x}_j is sufficiently small.

The effect of changing the width of the proposal function is highlighted in Figure 3.3. Three scenarios, each with the same underlying stationary distribution (A Gaussian of width 1.0 and mean 0.), are presented. The only difference between the three scenarios

1046 is the width of the proposal function, colloquially known as the ‘step size σ ’. Each
1047 scenario starts at an initial parameter value of 10.0 which would be considered an
1048 extreme variation. For the case where $\sigma = 0.1$, it is clear to see that the chain takes
1049 a long time to reach the expected region of the parameter. This indicates that this
1050 chain would have a large burn-in period and does not converge to the stationary
1051 distribution until step ~ 500 . Furthermore, whilst the chain does move towards the
1052 expected region, each step is significantly correlated with the previous. Considering
1053 the case where $\sigma = 5.0$, the chain approaches the expected parameter region almost
1054 instantly meaning that the burn-in period is not significant. However, there are clearly
1055 large regions of steps where the chain does not move. This is likely due to the chain
1056 proposing steps in the tails of the distribution which have a low probability of being
1057 accepted. Consequently, this chain would take a significant number of steps to fully
1058 span the allowable parameter region. For the final scenario, where $\sigma = 0.5$, you can see
1059 a relatively small burn-in period of approximately 100 steps. Once the chain reaches
1060 the stationary distribution, it moves throughout the expected region of parameter
1061 values many times, sufficiently sampling the full parameter region. This example is a
1062 single parameter varying across a continuous distribution and does not fully reflect
1063 the difficulties in the many-hundred multi-variate parameter distribution used within
1064 this analysis. However, it does give a conceptual idea of the importance of selecting
1065 the proposal function and associated step size.

1066 As discussed, step size tuning directly correlates to the average step acceptance
1067 rate. If the step size is too small, many steps will be accepted but the chain moves
1068 slowly. If the opposite is true, many steps will be rejected as the chain proposes steps
1069 in the tails of the distribution. Discussion in [129] suggests that the ‘ideal’ acceptance
1070 rate of a high dimension MCMC chain should be approximately $\sim 25\%$. An “ideal”
1071 step size [129] of

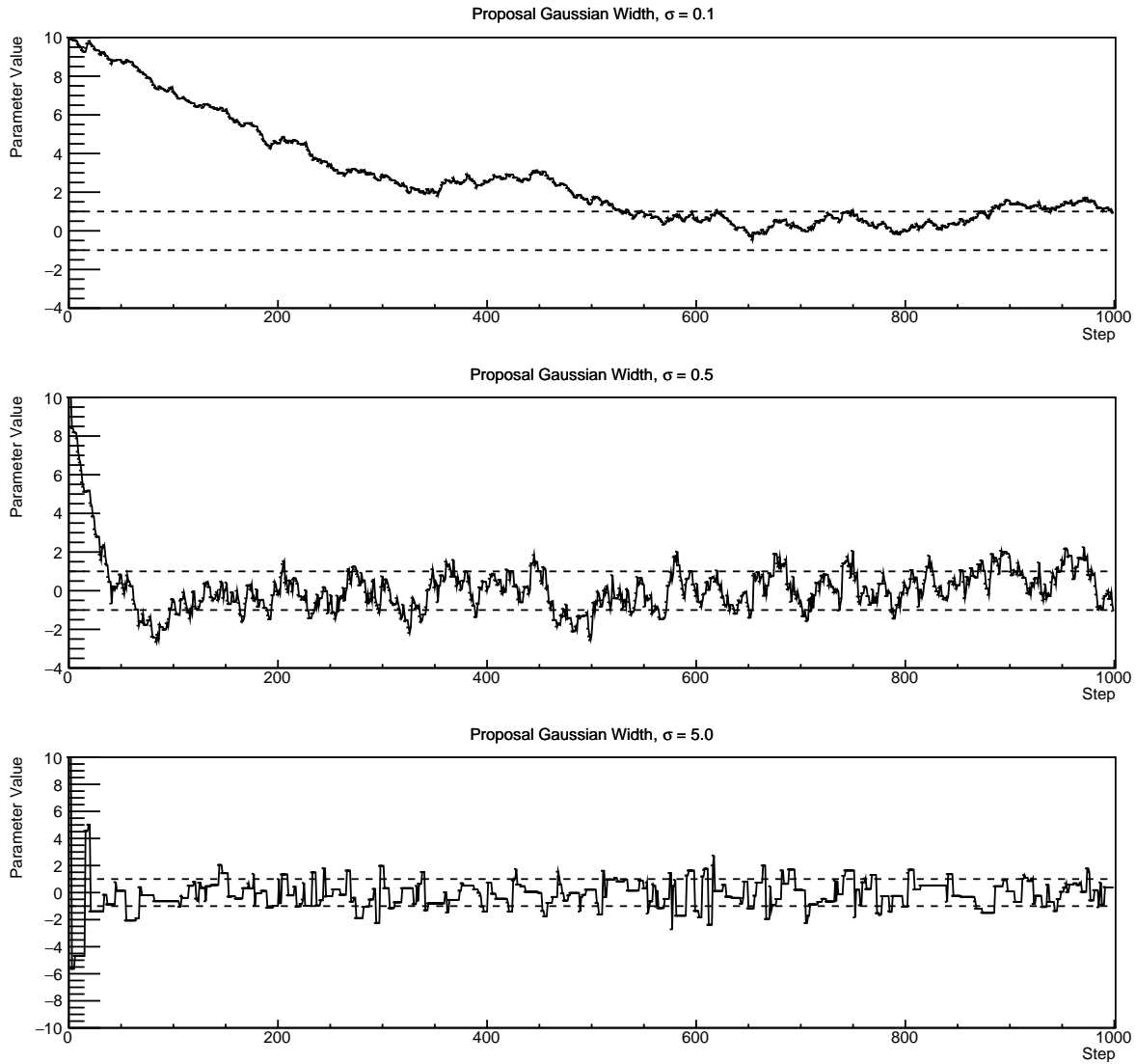


Figure 3.3: Three MCMC chains, each with a stationary distribution equal to a Gaussian centered at 0 and width 1 (As indicated by the black dotted lines). All of the chains use a Gaussian proposal function but have different widths (or ‘step size σ ’). The top panel has $\sigma = 0.1$, middle panel has $\sigma = 0.5$ and the bottom panel has $\sigma = 5.0$.

$$\sigma = \frac{2.4}{N_p}, \quad (3.6)$$

1072 where N_p is the number of parameters included in the MCMC fit. However, the
 1073 complex correlations between systematics mean that some parameters have to be hand

¹⁰⁷⁴ tuned and many efforts have been taken to select a set of parameter-by-parameter step
¹⁰⁷⁵ sizes to approximately reach the ideal acceptance rate.

¹⁰⁷⁶ Figure 3.3 highlights the likelihood as calculated by the fit in [DB: Link to AsimovA](#)
¹⁰⁷⁷ [Sensitivity Section](#) as a function of the number of steps in each chain. In practice,
¹⁰⁷⁸ many independent MCMC chains are run simultaneously to parallelise the task of
¹⁰⁷⁹ performing the fit. This figure overlays the distribution found in each chain. As seen,
¹⁰⁸⁰ the likelihood decreases from its initial value and converges towards a stationary
¹⁰⁸¹ distribution after $\sim 1 \times 10^5$ steps. Each fit (whether it be different asimov fits or data
¹⁰⁸² fit) will have a different set of preferred parameter values which results in a different
¹⁰⁸³ stationary distribution. For each fit presented in this thesis, a burn-in period of 1×10^5
¹⁰⁸⁴ steps was found to be sufficient.

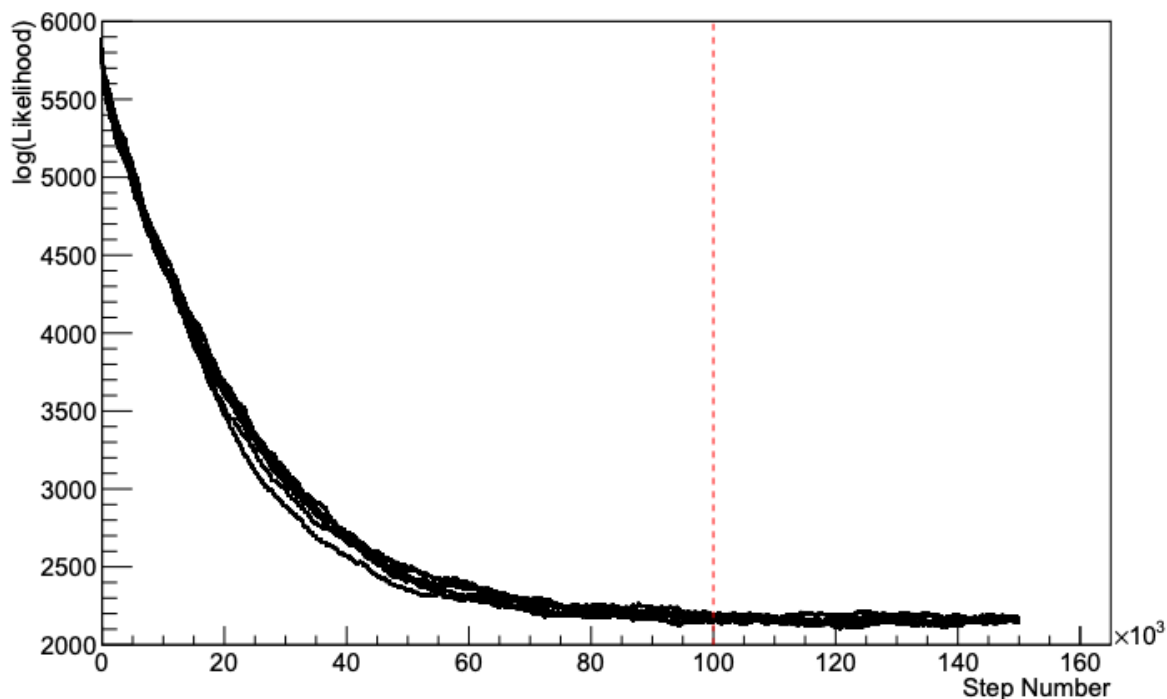


Figure 3.4: The log-likelihood from the fit detailed in [DB: Link to AsimovA](#) [Sensitivity Section](#) as a function of the number of steps accumulated in each fit. Many independent MCMC chains were run in parallel and overlaid on this plot. The red line indicates the 1×10^5 step burn-in period after which the log-likelihood becomes stable.

1085 3.3 Understanding the MCMC Results

1086 Whilst section 3.1 and section 3.2 describe how to interpret Bayesian statistics and
1087 explains the MCMC techniques used within this analysis, there is no mention of
1088 how to interpret the output of the chain. The posterior distribution output from the
1089 chain is a high dimension object, with as many dimensions as there are parameters
1090 included in the fit. However, this multi-dimensional object is difficult to conceptualize
1091 so parameter estimations are often presented in one or two-dimensional projections
1092 of this probability distribution. To do this, we invoke the marginalisation technique
1093 highlighted in subsection 3.3.1.

1094 3.3.1 Maginalisation

1095 The output of the MCMC chain is a highly dimensional probability distribution
1096 which is very difficult to interpret. From the standpoint of an oscillation analysis
1097 experiment, the one or two-dimensional ‘projections’ of the oscillation parameters of
1098 interest are most relevant. Despite this, the best fit values and uncertainties on the
1099 oscillation parameters of interest should correctly encapsulate the correlations to the
1100 other systematic uncertainties (colloquially called ‘nuisance’ parameters). For this joint
1101 beam and atmospheric analysis, the oscillation parameters of interest are $\sin^2(\theta_{23})$,
1102 $\sin^2(\theta_{13})$, Δm_{23}^2 , and δ_{CP} . All other parameters (Including the oscillation parameter
1103 this fit is insensitive to) are deemed nuisance parameters. To generate these projections,
1104 we rely upon integrating the posterior distribution over all nuisance parameters. This
1105 is called marginalisation. A simple example of this technique is to imagine the scenario
1106 where two coins are flipped. To determine the probability that the first coin returned
1107 a ‘head’, the exact result of the second coin flip is disregarded and simply integrated

1108 over. For the parameters of interest, $\vec{\theta}_i$, we can calculate the marginalised posterior by
1109 integrating over the nuisance parameters, $\vec{\theta}_n$. In this case, Equation 3.2 becomes

$$P(\vec{\theta}_i|D) = \frac{\int P(D|\vec{\theta}_i, \vec{\theta}_n)P(\vec{\theta}_i, \vec{\theta}_n)d\vec{\theta}_n}{\int P(D|\vec{\theta})P(\vec{\theta})d\vec{\theta}} \quad (3.7)$$

1110 Where $P(\vec{\theta}_i, \vec{\theta}_n)$ encodes the prior knowledge about the uncertainty and correlations
1111 between the parameters of interest and the nuisance parameters. In practice, this
1112 is simply taking the one or two-dimensional projection of the multi-dimensional
1113 probability distribution.

1114 Whilst in principle an easy solution to a complex problem, correlations between the
1115 interesting and nuisance parameters can bias the marginalised results. A similar effect
1116 is found when the parameters being marginalised over have non-Gaussian probability
1117 distributions. For example, Figure 3.5 highlights the marginalisation bias in the
1118 probability distribution found for a parameter when requiring a correlated parameter
1119 to have a positive parameter value. Due to the complex nature of this oscillation
1120 parameter fit presented in this thesis, there are certainly correlations occurring between
1121 the oscillation parameters of interest and the other nuisance parameters included in
1122 the fit.

1123 3.3.2 Parameter Estimation and Credible Intervals

1124 The purpose of this analysis is to determine the best fit values for the oscillation param-
1125 eters that the beam and atmospheric samples are sensitive to; $\sin^2(\theta_{23})$, $\sin^2(\theta_{13})$,
1126 Δm_{23}^2 , and δ_{CP} . Typically, the results presented take the form of one or two-dimension
1127 marginalised probability distributions for the appearance ($\sin^2(\theta_{13})$ and δ_{CP}) and

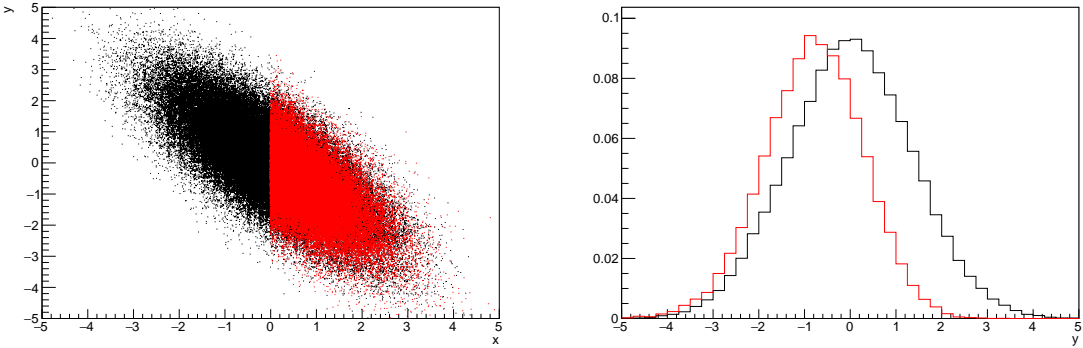


Figure 3.5: Left: The two dimensional probability distribution for two correlated parameters x and y . The red distribution shows the two dimensional probability distribution when $0 \leq x \leq 5$. Right: The marginalised probability distribution for the y parameter found when requiring the x to be bound between $-5 \leq x \leq 5$ and $0 \leq x \leq 5$ for the black and red distribution, respectively.

1128 disappearance ($\sin^2(\theta_{23})$ and Δm_{23}^2) parameters. The posterior probability density
 1129 taken from the output MCMC chain is binned in these parameters. The parameter
 1130 best-fit point is then taken to be the value that has the highest posterior probability.
 1131 This is performed in both one and two-dimensional projections.

1132 However, the single best-fit point in a given parameter is not of much use on its
 1133 own. We would also like to determine the uncertainty, or credible interval, on that
 1134 best-fit point. The definition of the 1σ credible interval is that we have 68% belief that
 1135 the parameter is within those bounds. For a more generalised definition, the credible
 1136 interval is the region of the posterior distribution that contains a specific fraction of
 1137 the total probability, such that

$$\int P(\theta|D)d\theta = \alpha \quad (3.8)$$

1138 Where θ is the parameter on which we calculate the credible interval. This technique
 1139 then calculates the $\alpha \times 100\%$ credible interval.

₁₁₄₀ In practice, this analysis uses the highest posterior density (HPD) credible intervals
₁₁₄₁ which are calculated through the following method. First, the probability distribution
₁₁₄₂ is area-normalised such that it has an integrated area equal to 1.0. The bins of proba-
₁₁₄₃ bility are then summed from the highest to lowest until the sum exceeds the 1σ level
₁₁₄₄ (0.68 in this example). This process is repeated for a range of credible intervals, notably
₁₁₄₅ the 1σ , 2σ and 3σ along with other levels where the critical values for each level can
₁₁₄₆ be found in [130]. This process can be repeated for the two-dimensional probability
₁₁₄₇ distributions by creating two-dimensional contours of credible intervals rather than a
₁₁₄₈ one-dimensional result.

₁₁₄₉ 3.3.3 Application of Bayes' Theorem

₁₁₅₀ Due to the matter resonance, this analysis has some sensitivity to the mass hierarchy
₁₁₅₁ of neutrino states (whether Δm_{23}^2 is positive or negative) and the octant of $\sin^2(\theta_{23})$
₁₁₅₂. The Bayesian approach utilised within this analysis gives an intuitive method of
₁₁₅₃ model comparison by determining which hypothesis is most favourable. Taking the
₁₁₅₄ ratio of Equation 3.3 for the two hypotheses of normal hierarchy, NH , and inverted
₁₁₅₅ hierarchy, IH , gives

$$\frac{P(\vec{\theta}_{NH}|D)}{P(\vec{\theta}_{IH}|D)} = \frac{P(D|\vec{\theta}_{NH})}{P(D|\vec{\theta}_{IH})} \times \frac{P(\vec{\theta}_{NH})}{P(\vec{\theta}_{IH})}. \quad (3.9)$$

₁₁₅₆ The middle term defines the Bayes factor which is a data-driven interpretation of
₁₁₅₇ how strong the data prefers one hierarchy to the other. For this analysis, equal priors
₁₁₅₈ on both mass hierarchy hypotheses are chosen ($P(\vec{\theta}_{NH}) = P(\vec{\theta}_{IH}) = 0.5$). In practice,
₁₁₅₉ the MCMC chain proposes a value of $|\Delta m_{23}^2|$ and then applies a 50% probability
₁₁₆₀ that the value is sign flipped. Consequently, the Bayes factor can be calculated from

1161 the ratio of the probability density in either hypothesis. This equates to counting the
1162 number of steps taken in the normal and inverted hierarchies and taking the ratio. The
1163 same approach can be taken to compare the upper octant (UO) compared to the lower
1164 octant (LO) hypothesis of $\sin^2(\theta_{23})$.

1165 Whilst the value of the Bayes factor should always be shown, the Jeffreys scale [131]
1166 (highlighted in Table 3.1) gives an indication of the strength of preference for one model
1167 compared to the other. Other interpretations of the strength of preference of a model
1168 exist, e.g. the Kass and Raferty Scale [132].

$\log_{10}(B_{AB})$	B_{AB}	Strength of Preference
< 0.0	< 1	No preference for hypothesis A (Supports hypothesis B)
0.0 – 0.5	1.0 – 3.16	Preference for hypothesis A is weak
0.5 – 1.0	3.16 – 10.0	Preference for hypothesis A is substantial
1.0 – 1.5	10.0 – 31.6	Preference for hypothesis A is strong
1.5 – 2.0	31.6 – 100.0	Preference for hypothesis A is very strong
> 2.0	> 100.0	Decisive preference for hypothesis A

Table 3.1: Jeffreys scale for strength of preference for two models A and B as a function of the calculated Bayes factor ($B_{AB} = B(A/B)$) between the two models [131]. The original scale is given in terms of $\log_{10}(B(A/B))$ but converted to linear scale for easy comparison throughout this thesis.

1169 3.3.4 Comparison of MCMC Output to Expectation

1170 Whilst not important for the extraction of oscillation parameters, understanding how
1171 the data constrains the model parameters is important to the understanding of this
1172 analysis. A simple method of doing this is to perform a comparison in the fitting
1173 parameters (For instance, the reconstructed neutrino energy and lepton direction for
1174 T2K far detector beam samples) of the spectra generated by the MCMC chain to ‘data’.
1175 This ‘data’ could be true data or some variation of Monte Carlo prediction. This allows
1176 easy comparison of the MCMC probability distribution to the data. To perform this, N

1177 steps from the post burn-in MCMC chain are randomly selected (Where for all plots
1178 of this style in this thesis, $N = 3000$). From these, the Monte Carlo prediction at each
1179 step is generated by reweighting the model parameters to the values specified at that
1180 step. Due to the probability density being directly correlated with the density of steps
1181 in a certain region, parameter values close to the best fit value are most likely to be
1182 selected.

1183 In practice, for each bin of the fitting parameters has a probability distribution
1184 of event rates, with one entry per sampled MCMC step. This distribution is binned
1185 where the bin with the highest probability is selected as the mean and an error on
1186 the width of this probability distribution is calculated using the approach highlighted
1187 in subsection 3.3.2. Consequently, the best fit distribution in the fit parameter is not
1188 necessarily that which would be attained by reweighting the Monte Carlo prediction
1189 to the most probable parameter values.

1190 A similar study can be performed to illustrate the freedom of the model parameter
1191 space prior to the fit. This can be done by throwing parameter values from the prior
1192 uncertainty of each parameter. This becomes troublesome for parameters with no
1193 prior uncertainty as the range is technically infinite. Where applicable solutions to
1194 remove these have been addressed.

₁₁₉₅ **Chapter 4**

₁₁₉₆ **Oscillation Probability Calculation**

₁₁₉₇ **4.1 Overview**

₁₁₉₈ The analysis presented within this thesis focuses on the determination of oscillation
₁₁₉₉ parameters from atmospheric and beam neutrinos. Whilst subject to the same oscil-
₁₂₀₀ lation probability, the way in which the two sets of samples have sensitivity to the
₁₂₀₁ different oscillation parameters differs quite significantly.

₁₂₀₂ Atmospheric neutrinos have a varying baseline, or “path length”, such that the
₁₂₀₃ distance each neutrino travels before interacting is dependent upon the zenith angle.
₁₂₀₄ Therefore the oscillation probability can be represented as a two-dimensional “oscillo-
₁₂₀₅ gram” as shown in Figure 4.1. For this calculation, four layers of fixed density were
₁₂₀₆ used to model the Earth with values taken from an approximation of the PREM model.
₁₂₀₇ These can be seen in the distinct discontinuities in the oscillogram as a function of the
₁₂₀₈ zenith angle.

₁₂₀₉ Another complexity of atmospheric neutrino oscillation probability calculation is
₁₂₁₀ the uncertainty in the height at which a neutrino was produced, termed the “produc-
₁₂₁₁ tion height”. Primary cosmic rays, whch contribute most of the neutrino flux, can
₁₂₁₂ interact anywhere between the Earth’s surface and $\sim 50\text{km}$ above that. The baseline,
₁₂₁₃ L , for a neutrino generated with zenith angle, θ , and production height, h , can be
₁₂₁₄ calculated as

$$L = \sqrt{(R_E + h)^2 - R_E^2 (1 - \cos^2(\theta))} - R_E \cos(\theta), \quad (4.1)$$

1215 where $R_E = 6,371\text{km}$ is the Earth's radius.

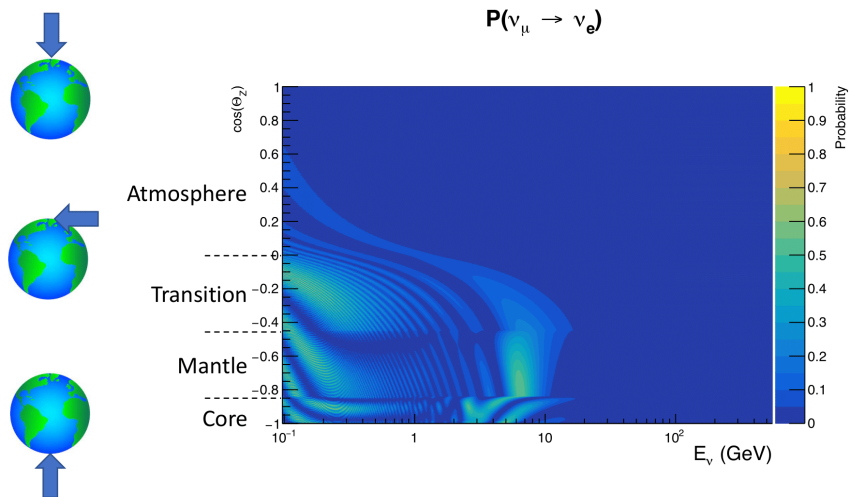


Figure 4.1: An “Oscillogram” that depicts the $P(\nu_\mu \rightarrow \nu_e)$ oscillation probability as a function of neutrino energy and cosine of the zenith angle. The zenith angle is defined such that $\cos(\theta_Z) = 1.0$ represents neutrinos that travel from directly above the detector. The four-layer constant density PREM model approximation is used and Asimov A oscillation parameters are assumed.

1216 Atmospheric neutrinos do have some sensitivity to δ_{CP} through a normalisa-
1217 tion term. Figure 4.2 illustrates the difference in oscillation probability between
1218 CP-conserving and CP-violating δ_{CP} values. The result is a complicated oscillation
1219 pattern in the appearance probability for sub-GeV upgoing neutrinos. The detector
1220 does not have sufficient resolution to resolve these individual patterns so the sensi-
1221 tivity to δ_{CP} for atmospheric neutrinos comes via the overall normalisation of the
1222 sub-GeV upgoing events. The presence of matter means that the effect δ_{CP} has on
1223 the oscillation probability is not equal between neutrinos and antineutrinos which
1224 would be expected when propagating through a vacuum. This is further extenuated

by the fact that SK can not distinguish neutrinos and antineutrinos well and that the cross-section neutrino interaction is larger than that for antineutrinos. Finally, sample selections (discussed in [DB: Link to selection chapter](#)) targeting different neutrino interaction modes (charge current quasi-elastic and single pion production) result in an imbalance in the percentage of neutrinos to anti-neutrinos in these samples due to pion capture. Negatively charged pions from antineutrino interactions are more likely to be captured by a nucleus compared to a positively charged pion emitted from a neutrino interaction. This all culminates in atmospheric neutrinos having a very complex sensitivity to δ_{CP} .

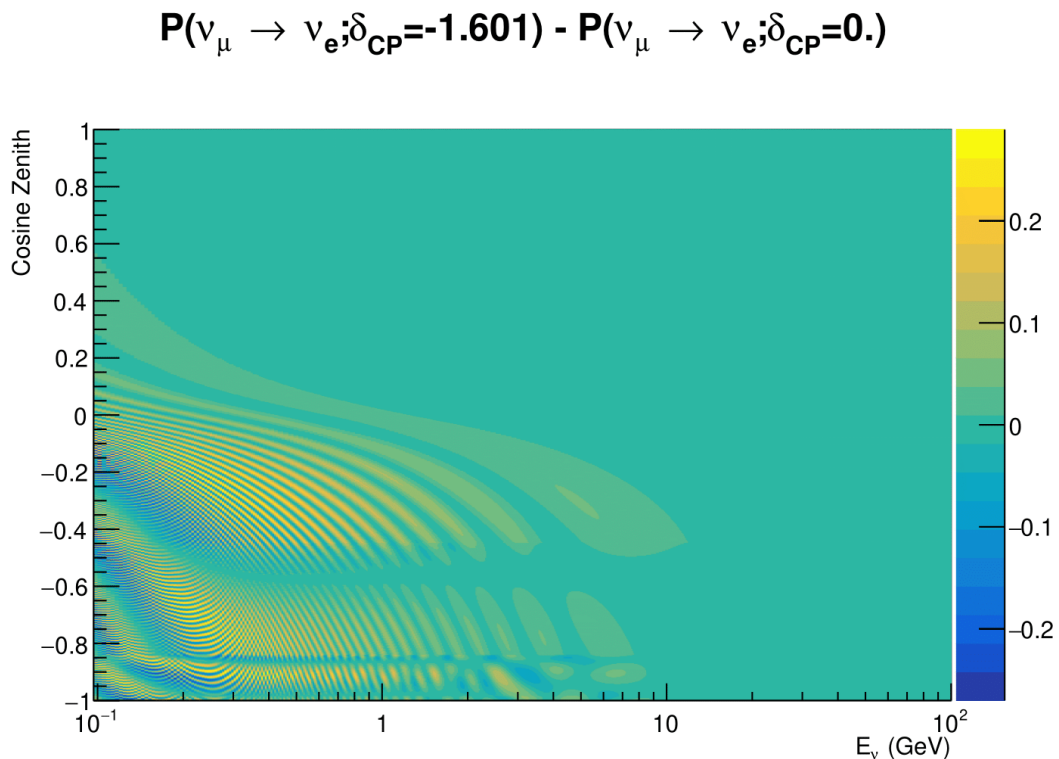


Figure 4.2: The effect of δ_{CP} for atmospheric neutrinos given in terms of the neutrino energy and zenith angle. The oscillogram compares the $P(\nu_\mu \rightarrow \nu_e)$ oscillation probability for a CP conserving ($\delta_{CP} = 0.0$) and CP violating ($\delta_{CP} = -1.601$) value of δ_{CP} . The other oscillation parameters assume the “Asimov A” oscillation parameter set given in Table 4.1.

Atmospheric neutrinos are subject to matter effects as they travel through the dense matter in the Earth. The vacuum and matter oscillation probabilities for $P(\nu_e \rightarrow \nu_e)$ and $P(\bar{\nu}_e \rightarrow \bar{\nu}_e)$ are presented in Figure 4.3. The oscillation probability for both neutrinos and antineutrinos are affected in the presence of matter but the resonance (Effects around $E_\nu \sim 5\text{GeV}$) only occurs for neutrinos in normal mass hierarchy and antineutrinos for inverse mass ordering. The exact position and amplitude of the resonance depend on $\sin^2(\theta_{23})$ meaning that the atmospheric neutrinos have sensitivity to the octant of θ_{23} .

As the T2K beam flux is centered at the first oscillation maximum, the sensitivity to δ_{CP} is predominantly observed as a change in the event-rate of e-like samples in $\nu/\bar{\nu}$ modes. Figure 4.4 illustrates the $P(\nu_\mu \rightarrow \nu_e)$ oscillation probability for a range of δ_{CP} values. A circular modulation of the oscillation peak (in both magnitude and position) is observed when varying throughout the allowable values of δ_{CP} . The CP-conserving values of $\delta_{CP} = 0, \pi$ have a lower(higher) oscillation maximum than the CP-violating values of $\delta_{CP} = -\pi/2 (\delta_{CP} = \pi/2)$ leading to a $\sin(\delta_{CP})$ type sensitivity. A sub-dominant shift in the energy of the oscillation peak is also present to aid in separating the two CP-conserving values of δ_{CP} .

T2K's sensitivity to the atmospheric oscillation parameters is more of a shape-based variation of the muon-like samples, as illustrated in Figure 4.4. The value of Δm_{32}^2 laterally shifts the position of the oscillation dip (around $E_\nu \sim 0.6\text{GeV}$) in the $P(\nu_\mu \rightarrow \nu_\mu)$ oscillation probability. A variation of $\sin^2(\theta_{23})$ is predominantly observed as a vertical shift of the oscillation dip with second-order horizontal shifts being due to matter effects. The beam neutrinos have limited sensitivity to matter effects due to the shorter baseline as well as the Earth's mantle is relatively low-density material (as compared to the Earth's core). For some values of δ_{CP} , the degeneracy in the

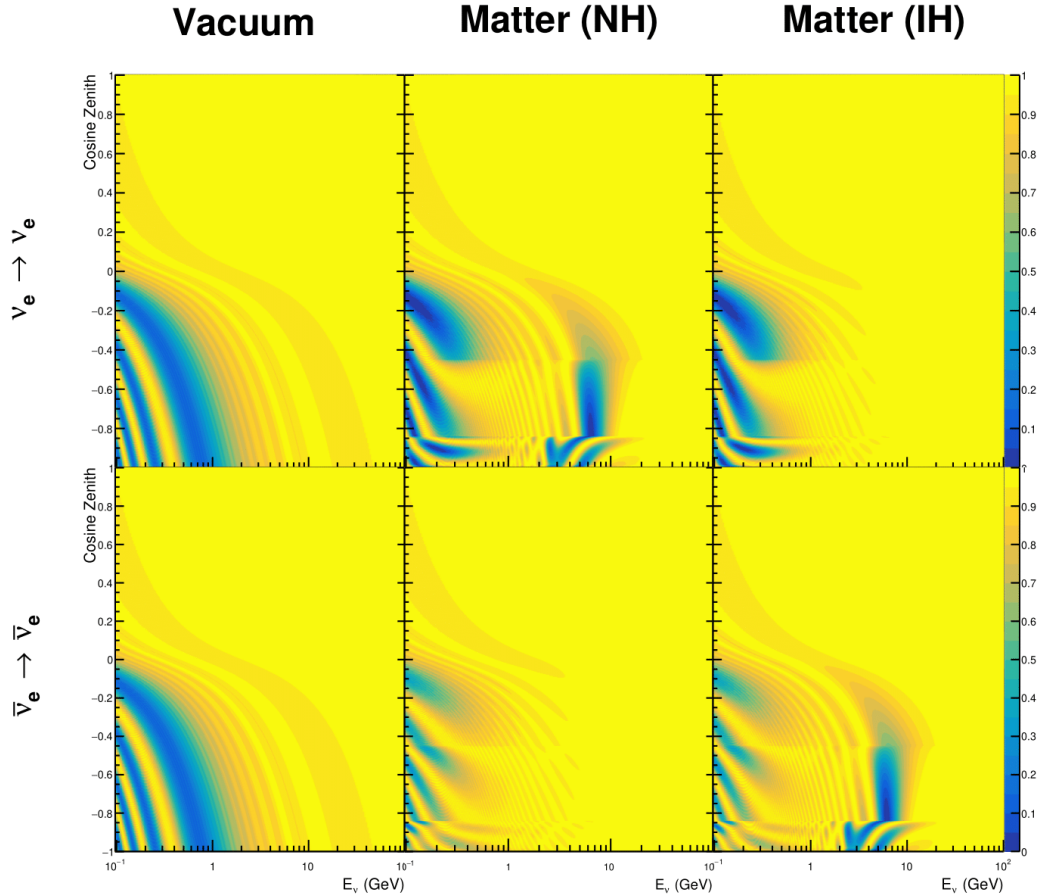


Figure 4.3: An illustration of the matter-induced effects on the oscillation probability, given as a function of neutrino energy and zenith angle. The top row of panels gives the $P(\nu_e \rightarrow \nu_e)$ oscillation probability and the bottom row illustrates the $P(\bar{\nu}_e \rightarrow \bar{\nu}_e)$ oscillation probability. The left column highlights the oscillation probability in a vacuum, whereas the middle and right column represents the oscillation probabilities when the four layer fixed density PREM model is assumed. All oscillation probabilities assume the “Asimov A” set given in Table 4.1, but importantly, the right column sets an inverted mass hierarchy. The “matter resonance” effects at $E_\nu \sim 5\text{GeV}$ can be seen in the $P(\nu_e \rightarrow \nu_e)$ for normal mass hierarchy and $P(\bar{\nu}_e \rightarrow \bar{\nu}_e)$ for inverted hierarchy.

number of e-like events allows the mass hierarchy to be resolved. This leads to a δ_{CP} -dependent mass hierarchy sensitivity. **DB: Bi-probability plot?**

Whilst all oscillation channels should be included for completeness, the computational resources required to run a fit are limited and any reasonable approximations which reduce the number of oscillation probability calculations which need to be made

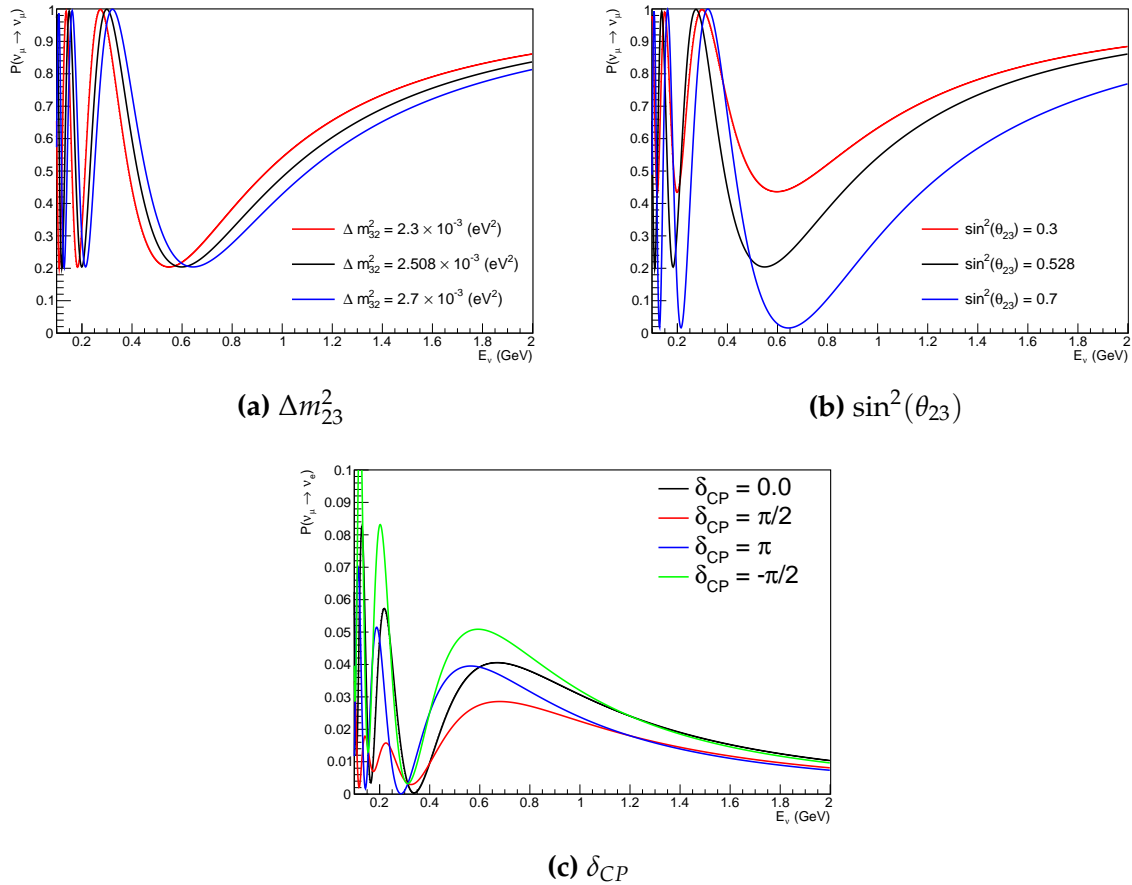


Figure 4.4: The oscillation probability for beam neutrino events, given as a function of neutrino energy. All oscillation parameters assume the “Asimov A” set given in Table 4.1 unless otherwise stated. Each panel represents a change in one of the oscillation parameters whilst keeping the remaining parameters fixed.

should be applied. The $\nu_e \rightarrow \nu_{e,\mu,\tau}$ (and antineutrino equivalent) oscillations can be ignored for beam neutrinos as the $\nu_e/\bar{\nu}_e$ fluxes being approximately two orders of magnitude smaller than the corresponding $\nu_\mu/\bar{\nu}_\mu$ flux. Furthermore, as the peak neutrino energy of the beam is well below the threshold for τ production ($E_\nu \sim 3$ GeV [133]) only a small proportion of the neutrinos produced in the beam have the required energy. For the few neutrinos that have sufficient energy, the oscillation probability is very small due to the short baseline. Whilst these approximations can be made for the beam neutrinos, the atmospheric flux of ν_e is of the same order of magnitude as the ν_μ flux and the energy distribution of atmospheric neutrinos extends well above the tau production threshold.

Throughout this thesis, several spectra predictions, Asimov fits, and contour comparisons are presented which require oscillation parameters to be assumed. Table 4.1 defines two sets of oscillation parameters, with “Asimov A” set being close to the preferred values from a previous T2K-only fit DB: Need Citation and “Asimov B” being CP-conserving and further from maximal θ_{23} mixing.

Parameter	Asimov A	Asimov B
Δm_{12}^2	$7.53 \times 10^{-5} \text{ eV}^2$	
Δm_{32}^2	$2.509 \times 10^{-3} \text{ eV}^2$	
$\sin^2(\theta_{12})$	0.304	
$\sin^2(\theta_{13})$	0.0219	
$\sin^2(\theta_{23})$	0.528	0.45
δ_{CP}	-1.601	0.0

Table 4.1: Reference values of the neutrino oscillation parameters for two different oscillation parameter sets.

4.2 Treatment of Fast Oscillations

As shown in Figure 4.5, atmospheric neutrino oscillations have a significantly more complex structure for upgoing neutrinos with energy below 1GeV. This is because the L/E dependence of the oscillation probability in this region induces rapid variations for small changes in L or E . As discussed in section 4.1, this is also the region in which atmospheric neutrinos have sensitivity to δ_{CP} . In practice, the direction between the detector and a neutrino’s production vertex is inferred from the direction of any secondary particles created in the detector target. For low energy neutrinos, this inference can be rather poor and introduces a distinct difference to beam neutrinos where the direction to production vertex is very well known.

As a consequence of the poor detector resolution, an average oscillation probability is observed in this region. This creates a computational problem as a significantly

1291 large amount of MC statistics would be required to accurately predicted the number
1292 of events in each bin if MC averaging was the only technique used. This section
1293 describes the ‘sub-sampling’ approach developed for this analysis and compares it to
1294 the methodology used within the SK-only analysis.

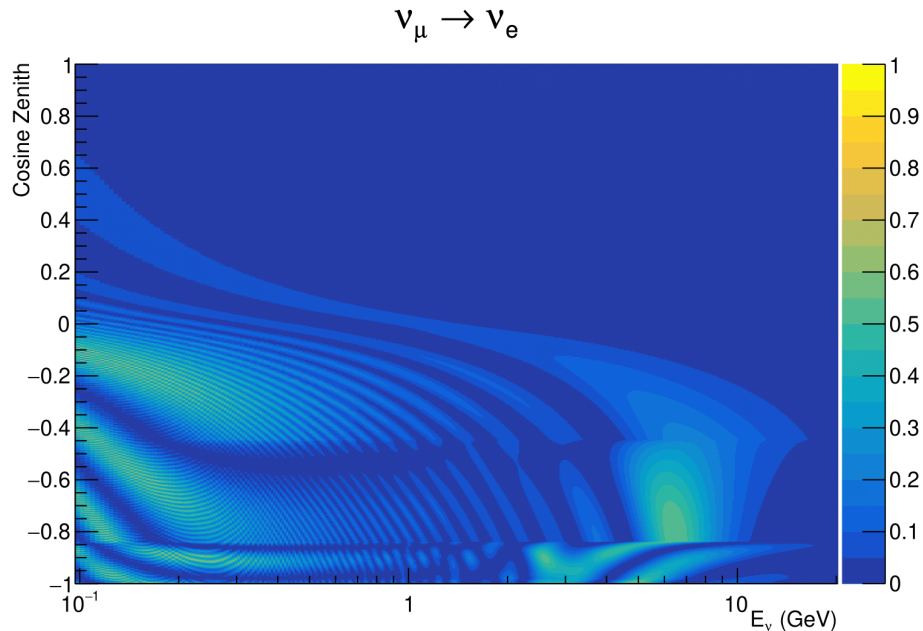


Figure 4.5: The oscillation probability $P(\nu_\mu \rightarrow \nu_e)$, given as a function of neutrino energy and zenith angle, which highlights an example of the “fast” oscillations in the sub-GeV upgoing region.

1295 The official SK-only analysis uses the osc3++ oscillation parameter fitter [20]. To
1296 perform the fast oscillation averaging, it uses a ‘nearest-neighbour’ technique. For a
1297 given neutrino MC event, the nearest neighbours in reconstructed lepton momentum
1298 and zenith angle are found and a distribution of neutrino energies is built. This
1299 distribution is then used to compute an average oscillation probability for the given
1300 neutrino MC event.

1301 For the i^{th} event, the oscillation weight is calculated as

$$W_i = \frac{1}{5}P(E_i, \bar{L}_i) + \frac{1}{5} \sum_{\beta=-1, -0.5, 0.5, 1} P(E_i + \beta\sigma_i, L_\beta), \quad (4.2)$$

where $P(E, L)$ is the oscillation probability calculation for neutrino energy E and path length L , σ_i is the RMS of the energy distribution for the given event, and the two path lengths, \bar{L}_i and L_β are discussed below. In practice, twenty of the nearest neighbours are used to generate the neutrino energy distribution. All of the oscillation probability calculations are performed with a fixed zenith angle (and therefore have same matter density profile).

The uncertainty in the production height is controlled by using an “average” production height. \bar{L}_i represents the average path length computed using twenty production heights taken from the Honda flux model’s prediction DB: Need citation for a fixed zenith angle, where the production heights are sampled in steps of 5% of their cumulative distribution function. L_β values are similarly calculated but instead use different combinations of four production heights (sampled in the same way),

$$\begin{aligned} L_{-1.0} &= \frac{1}{4}L(45, 50, 55, 60), \\ L_{-0.5} &= \frac{1}{4}L(35, 40, 65, 70), \\ L_{+0.5} &= \frac{1}{4}L(25, 30, 75, 68), \\ L_{+1.0} &= \frac{1}{4}L(15, 20, 85, 89). \end{aligned} \quad (4.3)$$

This averaging works well because of the correlation between true neutrino zenith angle and the inferred direction from secondary particles in the detector. For low energy neutrinos, where the resolution of the true neutrino direction is poor, σ_i will be

₁₃₁₇ large resulting in significant averaging effects. Contrary to this, the inferred direction
₁₃₁₈ of high energy neutrinos will be much closer to the true value, meaning that σ_i will be
₁₃₁₉ smaller.

₁₃₂₀ In practice, this technique is performed before the fit in order to deal with the
₁₃₂₁ computational cost. Oscillation probabilities are pre-calculated on a 4D grid. This
₁₃₂₂ is possible as the Osc3++ framework uses binned oscillation parameters rather than
₁₃₂₃ continuous so the oscillation parameters used in the fit are known prior to run-time. The
₁₃₂₄ framework used in the analysis presented within this thesis uses continuous oscillation
₁₃₂₅ parameters. Due to the MCMC technique invoked within the fitter ([DB: Link to MCMC](#)
₁₃₂₆ chapter), there is no way to know which parameter values will be selected at run-time.
₁₃₂₇ Therefore, the oscillation parameter calculation would have to be performed at run-
₁₃₂₈ time which is very expensive for event-by-event reweighting. Having to compute five
₁₃₂₉ oscillation probabilities per event would require far too much computational resources
₁₃₃₀ to be viable so the SK technique can not be used within this analysis. However, the
₁₃₃₁ concept of the averaging technique can be taken from it.

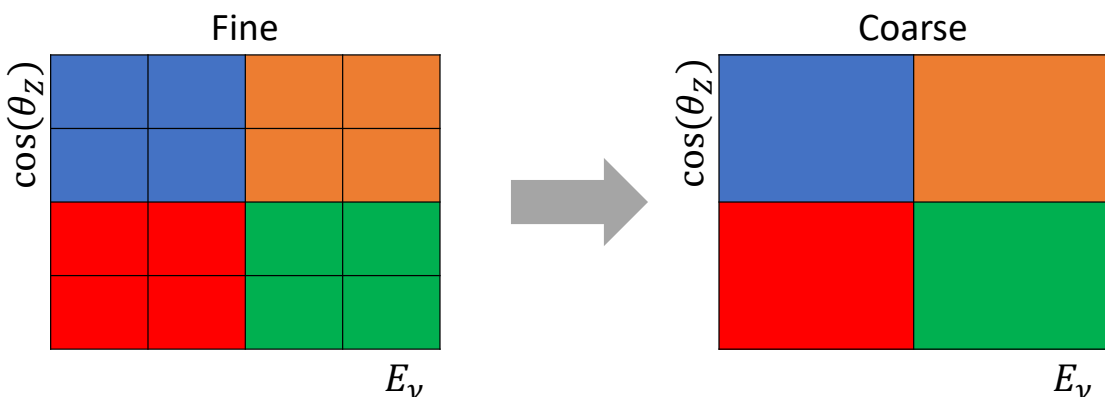


Figure 4.6: Illustration of the averaging procedure for $N = 2$. The oscillation probabilities calculated on the finer left binning are averaged to obtain the oscillation probabilities in the coarser right binning. These averaged oscillation probabilities with the coarser binning are then applied to each event during the fit.

1332 This analysis uses a binned oscillogram in which oscillation probabilities for a given
1333 event are selected based on that event's attributes. To perform a similar averaging as
1334 the SK analysis, a sub-sampling approach has been devised. The technique can be
1335 explained by considering a "fine" and "coarse" oscillogram. The fine oscillograms
1336 are used to define the array of cosine zeniths and energies for the neutrino oscillation
1337 engine. The coarse oscillograms cover the same phasespace as the fine oscillograms
1338 but have fewer bins in that range. Then, for a given coarse oscillogram bin, the value
1339 of that bin will be taken as the average of all the oscillation probabilities of all the fine
1340 oscillogram bins which fall into that coarse oscillogram bin.

1341 The binning which is used to calculate the oscillation probabilities, known as the
1342 'fine' binning, has $N \times N$ subdivisions per coarse bin. The value assigned to a coarse
1343 bin is the linear average (flat prior in E_ν and $\cos(\theta_Z)$) of all the oscillation probabilities
1344 calculated at the center of each fine bin contained within that coarse bin. Figure 4.6
1345 illustrates the $N = 2$ example where the assigned value to a coarse bin is the linear
1346 average of the four fine bins which fall in that coarse bin. Whilst the coarse bin edges
1347 are not linear in either axis, the sub-division of the fine bins is linear over the range
1348 of a coarse bin. The alignment of the fine and coarse binning edges are checked at
1349 run-time.

1350

₁₃₅₁ **Bibliography**

- ₁₃₅₂ [1] J. Chadwick, Verhandl. Dtsc. Phys. Ges. **16**, 383 (1914).
- ₁₃₅₃ [2] C. D. Ellis and W. A. Wooster, Proc. R. Soc. Lond. A Math. Phys. Sci. **117**, 109
₁₃₅₄ (1927).
- ₁₃₅₅ [3] W. Pauli, Phys. Today **31N9**, 27 (1978).
- ₁₃₅₆ [4] E. Fermi, Z. Phys. **88**, 161 (1934).
- ₁₃₅₇ [5] F. Reines and C. L. Cowan, Phys. Rev. **92**, 830 (1953).
- ₁₃₅₈ [6] C. L. Cowan, F. Reines, F. B. Harrison, H. W. Kruse, and A. D. McGuire, Science
₁₃₅₉ **124**, 103 (1956), <http://science.sciencemag.org/content/124/3212/103.full.pdf>.
- ₁₃₆₀ [7] G. Danby *et al.*, Phys. Rev. Lett. **9**, 36 (1962).
- ₁₃₆₁ [8] K. Kodama *et al.*, Physics Letters B **504**, 218 (2001).
- ₁₃₆₂ [9] LSND, A. Aguilar-Arevalo *et al.*, Phys. Rev. **D64**, 112007 (2001), hep-ex/0104049.
- ₁₃₆₃ [10] MiniBooNE Collaboration, A. A. Aguilar-Arevalo *et al.*, Phys. Rev. Lett. **110**,
₁₃₆₄ 161801 (2013).
- ₁₃₆₅ [11] and P. A. R. Ade *et al.*, Astronomy and Astrophysics **594**, A13 (2016).
- ₁₃₆₆ [12] B. Pontecorvo, Sov. Phys. JETP **26**, 984 (1968), [Zh. Eksp. Teor. Fiz. 53, 1717 (1967)].
- ₁₃₆₇ [13] B. Pontecorvo, Sov. Phys. JETP **7**, 172 (1958), [Zh. Eksp. Teor. Fiz. 34, 247 (1957)].
- ₁₃₆₈ [14] M. Kobayashi and T. Maskawa, Progress of Theoretical Physics **49**, 652 (1973).
- ₁₃₆₉ [15] N. Cabibbo, Phys. Rev. Lett. **10**, 531 (1963).
- ₁₃₇₀ [16] A. Y. Smirnov, (2003).
- ₁₃₇₁ [17] S. Mikheyev and A. Smirnov, Soviet Journal of Nuclear Physics **42**, 913 (1985).
- ₁₃₇₂ [18] L. Wolfenstein, Phys. Rev. D **17**, 2369 (1978).
- ₁₃₇₃ [19] A. M. Dziewonski and D. L. Anderson, Phys. Earth Planet. Inter. **25**, 297 (1981).
- ₁₃₇₄ [20] R. Wendell, *Three Flavor Oscillation Analysis of Atmospheric Neutrinos in Super-Kamiokande*, PhD thesis, University of North Carolina, 2008.
₁₃₇₅

- 1376 [21] The Super-Kamiokande Collaboration, Y. Ashie *et al.*, Phys. Rev. Lett. **93**, 101801
1377 (2004).
- 1378 [22] SNO Collaboration, Q. R. Ahmad *et al.*, Phys. Rev. Lett. **89**, 011301 (2002).
- 1379 [23] 2015 Nobel prize in Physics as listed by Nobelprize.org, [https://www.](https://www.nobelprize.org/nobel_prizes/physics/laureates/2015/)
1380 [nobelprize.org/nobel_prizes/physics/laureates/2015/](https://www.nobelprize.org/nobel_prizes/physics/laureates/2015/), Accessed: 18-04-
1381 2018.
- 1382 [24] J. A. Formaggio and G. P. Zeller, Rev. Mod. Phys. **84**, 1307 (2012), 1305.7513.
- 1383 [25] A. Bellerive, Int. J. Mod. Phys. A **19**, 1167 (2004).
- 1384 [26] R. Davis, D. S. Harmer, and K. C. Hoffman, Phys. Rev. Lett. **20**, 1205 (1968).
- 1385 [27] N. Vinyoles *et al.*, Astrophys. J. **835**, 202 (2017).
- 1386 [28] V. Gribov and B. Pontecorvo, Phys. Lett. B **28**, 493 (1969).
- 1387 [29] K. S. Hirata *et al.*, Phys. Rev. Lett. **63**, 16 (1989).
- 1388 [30] W. Hampel *et al.*, Phys. Lett. B **447**, 127 (1999).
- 1389 [31] SAGE Collaboration, J. N. Abdurashitov *et al.*, Phys. Rev. C **60**, 055801 (1999).
- 1390 [32] Q. R. Ahmad *et al.*, Phys. Rev. Lett. **89** (2002).
- 1391 [33] Borexino Collaboration, Nature **562**, 505 (2018).
- 1392 [34] B. Aharmim *et al.*, Astrophys. J. **653**, 1545 (2006).
- 1393 [35] M. Agostini *et al.*, (2020).
- 1394 [36] S. Andringa *et al.*, Adv. High Energy Phys. **2016**, 1 (2016).
- 1395 [37] J. F. Beacom *et al.*, Chin. phys. C **41**, 023002 (2017).
- 1396 [38] F. An *et al.*, J. Phys. G Nucl. Part. Phys. **43**, 030401 (2016).
- 1397 [39] J. Aalbers *et al.*, (2020), 2006.03114.
- 1398 [40] T. K. Gaisser and M. Honda, (2002).
- 1399 [41] G. D. Barr, T. K. Gaisser, P. Lipari, S. Robbins, and T. Stanev, Physical Review D
1400 **70** (2004).
- 1401 [42] M. Honda, T. Kajita, K. Kasahara, S. Midorikawa, and T. Sanuki, Physical Review

- 1402 D **75** (2007).
- 1403 [43] M. Honda, T. Kajita, K. Kasahara, and S. Midorikawa, Phys. Rev. D **70**, 043008
1404 (2004).
- 1405 [44] A. Fasso, A. Ferrari, P. R. Sala, and J. Ranft, (2001).
- 1406 [45] Y. Ashie *et al.*, Physical Review D **71** (2005).
- 1407 [46] F. Reines *et al.*, Phys. Rev. Lett. **15**, 429 (1965).
- 1408 [47] D. Casper *et al.*, Phys. Rev. Lett. **66**, 2561 (1991).
- 1409 [48] K. S. Hirata *et al.*, Phys. Lett. B **280**, 146 (1992).
- 1410 [49] Z. Li *et al.*, Physical Review D **98** (2018).
- 1411 [50] Kamiokande Collaboration *et al.*, (2017).
- 1412 [51] T2K Collaboration, Nature **580**, 339 (2020).
- 1413 [52] M. A. Acero *et al.*, Phys. Rev. Lett. **123**, 151803 (2019).
- 1414 [53] M. G. Aartsen *et al.*, Phys. Rev. Lett. **120** (2018).
- 1415 [54] P. Adamson *et al.*, Phys. Rev. Lett. **112** (2014).
- 1416 [55] M. S. Athar *et al.*, Progress in Particle and Nuclear Physics **124**, 103947 (2022).
- 1417 [56] G. Danby *et al.*, Phys. Rev. Lett. **9**, 36 (1962).
- 1418 [57] K. Abe *et al.*, Physical Review D **87** (2013).
- 1419 [58] MINOS Collaboration, D. G. Michael *et al.*, Phys. Rev. Lett. **97**, 191801 (2006).
- 1420 [59] G. Danby *et al.*, Phys. Rev. Lett. **9**, 36 (1962).
- 1421 [60] NOvA Collaboration, M. A. Acero *et al.*, Phys. Rev. Lett. **123**, 151803 (2019).
- 1422 [61] B. Abi, R. Acciarri, M. A. Acero, and G. e. a. Adamov, Eur. Phys. J. C Part. Fields
1423 **80** (2020).
- 1424 [62] Hyper-Kamiokande Proto-Collaboration *et al.*, Prog. Theor. Exp. Phys. **2015**,
1425 53C02 (2015).
- 1426 [63] C. Blanco, D. Hooper, and P. Machado, Physical Review D **101** (2020).
- 1427 [64] MicroBooNE Collaboration *et al.*, Search for an Excess of Electron Neutrino

- 1428 Interactions in MicroBooNE Using Multiple Final State Topologies, 2021.
- 1429 [65] KARMEN Collaboration, B. Armbruster *et al.*, Phys. Rev. D **65**, 112001 (2002).
- 1430 [66] S.-B. Kim, T. Lasserre, and Y. Wang, Adv. High Energy Phys. **2013**, 1 (2013).
- 1431 [67] M. Sajjad Athar *et al.*, Prog. Part. Nucl. Phys. **124**, 103947 (2022), 2111.07586.
- 1432 [68] K. Abe *et al.*, Nucl. Instrum. Methods Phys. Res. A **1027**, 166248 (2022).
- 1433 [69] F. P. An *et al.*, Phys. Rev. Lett. **108**, 171803 (2012).
- 1434 [70] RENO Collaboration, J. K. Ahn *et al.*, Phys. Rev. Lett. **108**, 191802 (2012).
- 1435 [71] Double Chooz Collaboration, Y. Abe *et al.*, Phys. Rev. Lett. **108**, 131801 (2012).
- 1436 [72] J. Collaboration *et al.*, TAO Conceptual Design Report: A Precision Measurement
1437 of the Reactor Antineutrino Spectrum with Sub-percent Energy Resolution, 2020,
1438 2005.08745.
- 1439 [73] for the RENO Collaboration, New results from RENO and the 5 MeV excess,
1440 AIP Publishing LLC, 2015.
- 1441 [74] Y. Abe *et al.*, Journal of High Energy Physics **2014** (2014).
- 1442 [75] Daya Bay Collaboration, D. Adey *et al.*, Phys. Rev. Lett. **123**, 111801 (2019).
- 1443 [76] M. P. Decowski, Nucl. Phys. B. **908**, 52 (2016).
- 1444 [77] The KamLAND Collaboration, A. Gando *et al.*, Phys. Rev. D **83**, 052002 (2011).
- 1445 [78] Y. Fukuda *et al.*, Phys. Rev. Lett. **81**, 1562 (1998).
- 1446 [79] K. Abe *et al.*, Nuclear Instruments and Methods in Physics Research Section
1447 A: Accelerators, Spectrometers, Detectors and Associated Equipment **737**, 253
1448 (2014).
- 1449 [80] S. Fukuda *et al.*, Nucl. Instrum. Methods Phys. Res. A **501**, 418 (2003).
- 1450 [81] Y. Itow *et al.*, (2001).
- 1451 [82] M. Jiang *et al.*, Prog. Theor. Exp. Phys. **2019** (2019).
- 1452 [83] S. Fukuda *et al.*, Nuclear Instruments and Methods in Physics Research Section
1453 A: Accelerators, Spectrometers, Detectors and Associated Equipment **501**, 418
1454 (2003), <http://www.sciencedirect.com/science/article/pii/S016890020300425X>.

- [84] Y. Nakano *et al.*, Nucl. Instrum. Methods Phys. Res. A **977**, 164297 (2020).
- [85] Hamamatsu, Hamamatsu Photonics Photomultiplier Tubes Handbook.
- [86] K. Abe *et al.*, Nucl. Instrum. Methods Phys. Res. A **1027**, 166248 (2022).
- [87] J. F. Beacom and M. R. Vagins, Phys. Rev. Lett. **93**, 171101 (2004).
- [88] L. Marti *et al.*, Nucl. Instrum. Methods Phys. Res. A **959**, 163549 (2020).
- [89] L. Marti *et al.*, (2019).
- [90] G. Carminati, Phys. Procedia **61**, 666 (2015).
- [91] T. Tanimori *et al.*, IEEE Transactions on Nuclear Science **36**, 497 (1989).
- [92] Super-Kamiokande Collaboration, J. Hosaka *et al.*, Phys. Rev. D **73**, 112001 (2006).
- [93] H. Nishino *et al.*, Nucl. Instrum. Methods Phys. Res. A **610**, 710 (2009).
- [94] S. Yamada *et al.*, IEEE Transactions on Nuclear Science **57**, 428 (2010).
- [95] S. Yamada, Y. Hayato, Y. Obayashi, and M. Shiozawa, New online system without hardware trigger for the Super-Kamiokande experiment, in *2007 IEEE Nuclear Science Symposium Conference Record*, IEEE, 2007.
- [96] P. A. Čerenkov, Phys. Rev. **52**, 378 (1937).
- [97] I. Frank and I. Tamm, Coherent visible radiation of fast electrons passing through matter, in *Selected Papers*, pp. 29–35, Springer Berlin Heidelberg, Berlin, Heidelberg, 1991.
- [98] The T2K Collaboration, KEK Proposal (2001),
<http://neutrino.kek.jp/jhfnu/loi/loi.v2.030528.pdf>.
- [99] Y. Itow *et al.*, (2001), hep-ex/0106019.
- [100] The K2K Collaboration and S. H. Ahn, (2001), hep-ex/0103001.
- [101] The T2K Collaboration, KEK Proposal (2006), http://j-parc.jp/researcher/Hadron/en/pac_0606/pdf/p11-Nishikawa.pdf.
- [102] T2K Collaboration, K. Abe *et al.*, Phys. Rev. Lett. **112**, 061802 (2014),
<https://link.aps.org/doi/10.1103/PhysRevLett.112.061802>.

- [103] NINJA Collaboration, T. Fukuda *et al.*, Proposal for precise measurement of neutrino-water cross-section in NINJA physics run, Proposal for J-PARC and KEK, 2017.
- [104] T. Ovsianikova *et al.*, Physics of Particles and Nuclei **48**, 1014 (2017), <https://doi.org/10.1134/S1063779617060478>.
- [105] M. Antonova *et al.*, Journal of Instrumentation **12**, C07028 (2017), <http://stacks.iop.org/1748-0221/12/i=07/a=C07028>.
- [106] The T2K Collaboration, K. Abe *et al.*, Phys. Rev. D **102**, 012007 (2020).
- [107] K. Abe *et al.*, Progress of Theoretical and Experimental Physics **2021** (2021).
- [108] The T2K Collaboration, K. Abe *et al.*, Nuclear Instruments and Methods in Physics Research Section A: Accelerators, Spectrometers, Detectors and Associated Equipment **659**, 106 (2011), <http://www.sciencedirect.com/science/article/pii/S0168900211011910>.
- [109] K. Matsuoka *et al.*, Nuclear Instruments and Methods in Physics Research Section A: Accelerators, Spectrometers, Detectors and Associated Equipment **624**, 591 (2010), <http://www.sciencedirect.com/science/article/pii/S016890021002098X>.
- [110] K. Abe *et al.*, Phys. Rev. D. **103** (2021).
- [111] T. Vladislavljevic, *Predicting the T2K neutrino flux and measuring oscillation parameters* Springer theses, 1 ed. (Springer Nature, Cham, Switzerland, 2020).
- [112] D. Beavis, A. Carroll, and I. Chiang, (1995).
- [113] P.-A. Amaudruz *et al.*, Nuclear Instruments and Methods in Physics Research Section A: Accelerators, Spectrometers, Detectors and Associated Equipment **696**, 1 (2012).
- [114] N. Abgrall *et al.*, Nuclear Instruments and Methods in Physics Research Section A: Accelerators, Spectrometers, Detectors and Associated Equipment **637**, 25 (2011).
- [115] S. Assylbekov *et al.*, Nuclear Instruments and Methods in Physics Research Section A: Accelerators, Spectrometers, Detectors and Associated Equipment **686**, 48 (2012).
- [116] D. Allan *et al.*, Journal of Instrumentation **8**, P10019 (2013).

- 1512 [117] F. Vannucci, Advances in High Energy Physics **2014**, 1 (2014).
- 1513 [118] UA1 magnet sets off for a second new life, 2022.
- 1514 [119] S. Aoki *et al.*, Nuclear Instruments and Methods in Physics Research Section
1515 A: Accelerators, Spectrometers, Detectors and Associated Equipment **698**, 135
1516 (2013).
- 1517 [120] M. Yokoyama *et al.*, Nuclear Instruments and Methods in Physics Research
1518 Section A: Accelerators, Spectrometers, Detectors and Associated Equipment
1519 **622**, 567 (2010).
- 1520 [121] K. Suzuki *et al.*, Progress of Theoretical and Experimental Physics **2015**, 53C01
1521 (2015).
- 1522 [122] S. Brooks, A. Gelman, G. L. Jones, and X.-L. Meng, *Handbook of Markov Chain
Monte Carlo* (CRC Press, 2011).
- 1524 [123] W. R. Gilks, S. Richardson, and D. J. Spiegelhalter, *Markov Chain Monte Carlo in
Practice* (Chapman & Hall/CRC Interdisciplinary Statistics, 1995).
- 1526 [124] C. Wret, *Minimising systematic uncertainties in the T2K experiment using near-
detector and external data*, PhD thesis, Imperial College London, 2018.
- 1528 [125] K. E. Duffy, *Measurement of the Neutrino Oscillation Parameters $\sin^2 \theta_{23}$, Δm_{32}^2 ,
1529 $\sin^2 \theta_{13}$, and δ_{CP} in Neutrino and Antineutrino Oscillation at T2K*, PhD thesis, Oriel
1530 College, University of Oxford, 2016.
- 1531 [126] T. Bayes, Rev. Phil. Trans. Roy. Soc. Lond. **53**, 370 (1764).
- 1532 [127] N. Metropolis, A. W. Rosenbluth, M. N. Rosenbluth, A. H. Teller, and E. Teller,
1533 Journal of Chemical Physics **21** (1970).
- 1534 [128] W. K. Hastings, Biometrika **57** (1970).
- 1535 [129] J. Dunkley, M. Bucher, P. G. Ferreira, K. Moodley, and C. Skordis, Mon. Not. R.
1536 Astron. Soc. **356**, 925 (2005).
- 1537 [130] Particle Data Group *et al.*, Prog. Theor. Exp. Phys. **2020** (2020).
- 1538 [131] H. Jeffreys, *The Theory of Probability* Oxford Classic Texts in the Physical Sciences
1539 (, 1939).
- 1540 [132] R. E. Kass and A. E. Raftery, J. Am. Stat. Assoc. **90**, 773 (1995).

- ₁₅₄₁ [133] P. Machado, H. Schulz, and J. Turner, Physical Review D **102** (2020).

1542 List of Figures

<small>1543</small>	1.1	The cross-section of neutrinos from various natural and man-made sources as a function of neutrino energy. Taken from [24]	<small>1544</small>	10				
<small>1545</small>	1.2	The solar neutrino flux as a function of neutrino energy for various fusion reactions and decay chains as predicted by the Standard Solar Model. Taken from [25].	<small>1546</small>	<small>1547</small>	11			
<small>1548</small>	1.3	Left panel: The atmospheric neutrino flux for different neutrino flavours as a function of neutrino energy as predicted by the 2007 Honda model (“This work”) [42], the 2004 Honda model (“HKKM04”) [43], the Bartol model [41] and the FLUKA model [44]. Right panel: The ratio of the muon to electron neutrino flux as predicted by all the quoted models. Both figures taken from [42].	<small>1549</small>	<small>1550</small>	<small>1551</small>	<small>1552</small>	<small>1553</small>	13
<small>1554</small>	1.4	A diagram illustrating the definition of zenith angle as used in the Super Kamiokande experiment [45].	<small>1555</small>	14				
<small>1556</small>	1.5	Predictions of the summed neutrino and antineutrino flux for electron and muon neutrinos from the Bartol [41], Honda [42] and FLUKA [44] models as a function of zenith angle with respect to the detector. Left panel: $0.3 < E_\nu < 0.5$. Middle panel: $0.9 < E_\nu < 1.5$. Right panel: $3.0 < E_\nu < 5.0$. Figures taken from [45].	<small>1557</small>	<small>1558</small>	<small>1559</small>	<small>1560</small>	15	
<small>1561</small>	1.6	Constraints on the atmospheric oscillation parameters, $\sin^2(\theta_{23})$ and Δm_{23}^2 , from atmospheric and long baseline experiments: SK [50], T2K [51], NO ν A [52], IceCube [53] and MINOS [54]. Figure taken from [55].	<small>1562</small>	<small>1563</small>	16			
<small>1564</small>	1.7	Reactor electron antineutrino fluxes for ^{235}U (Black), ^{238}U (Green), ^{239}Pu (Purple), and ^{241}Pu (Orange) isotopes. The inverse β -decay cross-section (Blue) and corresponding measurable neutrino spectrum (Red) are also given. Top panel: Schematic of Inverse β -decay interaction including the eventual capture of the emitted neutron. This capture emits a γ -ray which provides a second signal of the event. Taken from [67].	<small>1565</small>	<small>1566</small>	<small>1567</small>	<small>1568</small>	<small>1569</small>	19
<small>1570</small>	2.1	A schematic diagram of the Super-Kamiokande Detector. Taken from [81].	23					

1571	2.2	The location of “standard PMTs” (red) inside the SK detector. Taken from [79].	27
1572			
1573	2.3	Schematic view of the data flow through the data acquisition and online system. Taken from [94].	30
1574			
1575	2.4	The cross-section view of the Tokai to Kamioka experiment illustrating the beam generation facility at J-PARC, the near detector situated at a baseline of 280m and the Super Kamiokande far detector situated 295km from the beam target.	33
1576			
1577			
1578			
1579	2.5	The near detector suite for the T2K experiment showing the ND280 and INGRID detectors. The distance between the detectors and the beam target is 280m.	34
1580			
1581			
1582	2.6	Top panel: Bird’s eye view of the most relevant part of primary and secondary beamline used within the T2K experiment. The primary beamline is the main-ring proton synchrotron, kicker magnet, and graphite target. The secondary beamline consists of the three focusing horns, decay volume, and beam dump. Figure taken from [108]. Bottom panel: The side-view of the secondary beamline including the focusing horns, beam dump and neutrino detectors. Figure taken from [109].	36
1583			
1584			
1585			
1586			
1587			
1588			
1589	2.7	The Monte Carlo prediction of the energy spectrum for each flavour of neutrino (ν_e , $\bar{\nu}_e$, ν_μ and $\bar{\nu}_\mu$) in the neutrino dominated beam FHC mode (Left) and antineutrino dominated beam RHC mode (Right) expected at SK. Taken from [110].	37
1590			
1591			
1592			
1593	2.8	Top panel: T2K muon neutrino disappearance probability as a function of neutrino energy. Middle panel: T2K electron neutrino appearance probability as a function of neutrino energy. Bottom panel: The neutrino flux distribution for three different off-axis angles (Arbitrary units) as a function of neutrino energy.	39
1594			
1595			
1596			
1597			
1598	2.9	The components of the ND280 detector. The neutrino beam travels from left to right. Taken from [108].	40
1599			
1600	2.10	Comparison of data to Monte Carlo prediction of integrated deposited energy as a function of track length for particles that stopped in FGD1. Taken from [113].	42
1601			
1602			

1603	2.11 Schematic design of a Time Projection Chamber detector. Taken from [114].	43
1604	2.12 The distribution of energy loss as a function of reconstructed momentum for charged particles passing through the TPC, comparing data to Monte Carlo prediction. Taken from [114].	43
1605		
1606		
1607	2.13 A schematic of the P0D side-view. Taken from [115].	45
1608	2.14 Left panel: The Interactive Neutrino GRID on-axis Detector. 14 modules are arranged in a cross-shape configuration, with the center modules being directly aligned with the on-axis beam. Right panel: The layout of a single module of the INGRID detector. Both figures are recreated from [108].	47
1609		
1610		
1611		
1612		
1613	3.1 Example of using Monte Carlo techniques to find the area under the blue line. The gradient and intercept of the line are 0.4 and 1.0 respectively. The area found to be under the curve using one thousand samples is 29.9 units.	52
1614		
1615		
1616		
1617	3.2 The area under a line of gradient 0.4 and intercept 1.0 for the range $0 \leq x \leq 10$ as calculated using Monte Carlo techniques as a function of the number of samples used in each repetition. The analytical solution to the area is 30 units as given by the red line.	53
1618		
1619		
1620		
1621	3.3 Three MCMC chains, each with a stationary distribution equal to a Gaussian centered at 0 and width 1 (As indicated by the black dotted lines). All of the chains use a Gaussian proposal function but have different widths (or 'step size σ '). The top panel has $\sigma = 0.1$, middle panel has $\sigma = 0.5$ and the bottom panel has $\sigma = 5.0$.	58
1622		
1623		
1624		
1625		
1626	3.4 The log-likelihood from the fit detailed in DB: Link to AsimovA Sensitivity Section as a function of the number of steps accumulated in each fit. Many independent MCMC chains were run in parallel and overlaid on this plot. The red line indicates the 1×10^5 step burn-in period after which the log-likelihood becomes stable.	59
1627		
1628		
1629		
1630		

1631 3.5	Left: The two dimensional probability distribution for two correlated parameters x and y . The red distribution shows the two dimensional probability distribution when $0 \leq x \leq 5$. Right: The marginalised probability distribution for the y parameter found when requiring the x to be bound between $-5 \leq x \leq 5$ and $0 \leq x \leq 5$ for the black and red distribution, respectively.	62
1637 4.1	An “Oscillogram” that depicts the $P(\nu_\mu \rightarrow \nu_e)$ oscillation probability as a function of neutrino energy and cosine of the zenith angle. The zenith angle is defined such that $\cos(\theta_Z) = 1.0$ represents neutrinos that travel from directly above the detector. The four-layer constant density PREM model approximation is used and Asimov A oscillation parameters are assumed.	67
1643 4.2	The effect of δ_{CP} for atmospheric neutrinos given in terms of the neutrino energy and zenith angle. The oscillogram compares the $P(\nu_\mu \rightarrow \nu_e)$ oscillation probability for a CP conserving ($\delta_{CP} = 0.0$) and CP violating ($\delta_{CP} = -1.601$) value of δ_{CP} . The other oscillation parameters assume the “Asimov A” oscillation parameter set given in Table 4.1.	68
1648 4.3	An illustration of the matter-induced effects on the oscillation probability, given as a function of neutrino energy and zenith angle. The top row of panels gives the $P(\nu_e \rightarrow \nu_e)$ oscillation probability and the bottom row illustrates the $P(\bar{\nu}_e \rightarrow \bar{\nu}_e)$ oscillation probability. The left column highlights the oscillation probability in a vacuum, whereas the middle and right column represents the oscillation probabilities when the four layer fixed density PREM model is assumed. All oscillation probabilities assume the “Asimov A” set given in Table 4.1, but importantly, the right column sets an inverted mass hierarchy. The “matter resonance” effects at $E_\nu \sim 5\text{GeV}$ can be seen in the $P(\nu_e \rightarrow \nu_e)$ for normal mass hierarchy and $P(\bar{\nu}_e \rightarrow \bar{\nu}_e)$ for inverted hierarchy.	70
1659 4.4	The oscillation probability for beam neutrino events, given as a function of neutrino energy. All oscillation parameters assume the “Asimov A” set given in Table 4.1 unless otherwise stated. Each panel represents a change in one of the oscillation parameters whilst keeping the remaining parameters fixed.	71

1664	4.5	The oscillation probability $P(\nu_\mu \rightarrow \nu_e)$, given as a function of neutrino energy and zenith angle, which highlights an example of the “fast” oscillations in the sub-GeV upgoing region.	73
1665			
1666			
1667	4.6	Illustration of the averaging procedure for $N = 2$. The oscillation probabilities calculated on the finer left binning are averaged to obtain the oscillation probabilities in the coarser right binning. These averaged oscillation probabilities with the coarser binning are then applied to each event during the fit.	75
1668			
1669			
1670			
1671			

¹⁶⁷² List of Tables

¹⁶⁷³ 1.1	Description of the four layers of the Earth invoked within the PREM model [19].	¹⁶⁷⁴ 9
¹⁶⁷⁵ 2.1	The various SK periods and respective live-time. The SK-VI live-time is calculated until 1 st April 2022. SK-VII started during the writing of this thesis.	¹⁶⁷⁶ 22
¹⁶⁷⁷ 2.2	The trigger thresholds and extended time windows saved around an event which were utilised throughout the SK-IV period. The exact thresholds can change and the values listed here represent the thresholds at the start and end of the SK-IV period.	¹⁶⁷⁸ 31
¹⁶⁷⁹ 2.3	The threshold momentum and energy for a particle to generate Cherenkov light in ultrapure water, as calculated in Equation 2.2 in ultrapure water which has refractive index $n = 1.33$	¹⁶⁸⁰ 32
¹⁶⁸¹ 3.1	Jeffreys scale for strength of preference for two models A and B as a function of the calculated Bayes factor ($B_{AB} = B(A/B)$) between the two models [131]. The original scale is given in terms of $\log_{10}(B(A/B))$ but converted to linear scale for easy comparison throughout this thesis.	¹⁶⁸² 64
¹⁶⁸³ 4.1	Reference values of the neutrino oscillation parameters for two different oscillation parameter sets.	¹⁶⁸⁴ 72